Spin Diffusion in Dynamic Nuclear Polarization Nuclear Magnetic Resonance

PAR

Arthur César PINON

ÉCOLE POLYTECHNIQUE
FÉDÉRALE DE LAUSANNE

Suisse
2018

lol

Abstract

Dynamic Nuclear Polarization (DNP) is currently one of the most efficient ways of enhancing sensitivity in solid-state Nuclear Magnetic Resonance (NMR) experiments. The DNP protocol consists in doping a sample with a small amount of paramagnetic species, typically nitroxide biradicals, and carrying out either a magic-angle spinning (MAS) solid-state NMR experiment under microwave irradiation at 100 K or a dissolution DNP (dDNP) experiment under microwave irradiation at around 1.2 K.

Maximum theoretical enhancements that can be achieved in MAS DNP reach 658, while polarizations close to unity can be achieved in dDNP, translating into the possibility of studying atomic-level composition of dilute surface species at picomolar concentrations that would be otherwise out of reach.

Recent years witnessed very fast development of DNP instrumentation (high-power and high-frequency microwave sources, higher magnetic fields, faster sample spinning), polarizing agents (rigid dinitroxide biradicals) and new sample preparation techniques (sample formulation, optimisation of proton and radical concentration) which brought sensitivity enhancements (in MAS DNP) and nuclear polarizations (in dDNP) close to their theoretical maximum.

The first chapter of this thesis is focusing on the microscopic description of a DNP system. We show how nuclear polarization is intrinsically limited in NMR, how it can be increased, and how the introduction of paramagnetic species modifies the behaviours of various parameters in the system. In particular, we look at the spatial dependence of relaxation times, spin diffusion coefficient, and paramagnetic quenching close to the paramagnet location.

The second chapter is showing how using finite element numerical simulations can simulate the propagation of magnetization in homogeneous and heterogeneous DNP systems. We show that polarizing and relaxing powers are important parameters that greatly influence polarization dynamics. We observe how the diffusion equation behaves at steady state and how it can be linked to domain sizes in heterogeneous systems.

In the third chapter, experimental measurements are performed and compared with numerical simulations in order to confirm the structure of homogeneous DNP systems. The importance of radical and proton concentration are highlighted, as well as several ways of increasing the efficiency of cross polarization in homogeneous frozen solutions.

Finally, heterogeneous systems are studied in chapter four, where we combined NMR experiments and numerical simulations to determine spin diffusion coefficients, domain sizes, structures of core-shell particles, structure of perovskite materials, and predict that the bulk of inorganic materials can be significantly enhanced by DNP using spin diffusion.

Keywords

Spin Diffusion, Dynamic Nuclear Polarization, Nuclear Magnetic Resonance

Résumé

La technique de Polarisation Dynamique Nucléaire (PDN) est aujourd'hui l'une des méthodes les plus efficaces pour exalter la sensibilité des expériences de Résonnance Magnétique Nucléaire (RMN).

Une expérience de PDN consiste à doper l'échantillon avec des substances paramagnétiques, puis d'effectuer la mesure à faible température, afin d'augmenter la polarisation des noyaux concernés, et mesurer des signaux plus intenses.

L'exaltation maximale atteignable à une température de 100 K est de 658, et à une température de 1.2 K les polarisations atteintes sont proche de 100%. Ces dernières années, les rapides avancées technologiques en terme d'instrumentation pour la PDN (sources micro-ondes à haute fréquence et haute puissance, hauts champs magnétiques, rotations à l'angle magique de plus en plus rapides), en terme d'agents polarisant (bi-radicaux nitroxyde rigides), et en terme de préparation d'échantillon (technique d'imprégnation, variation de la quantité de protons et d'électrons) a permis d'obtenir des exaltations de polarisation proches du maximum théorique.

Le premier chapitre de cette thèse est consacré à la description microscopique des systèmes utilisés en PDN. Nous montrons comment la polarisation nucléaire est intrinsèquement limitée en RMN, comment elle peut être augmentée, et comment l'ajout de substances paramagnétiques modifie le comportement de plusieurs paramètres du système. En particulier, nous regardons la variation spatiale des temps de relaxation, du coefficient de diffusion de spin, et du quenching paramagnétique autour de la substance paramagnétique.

Le second chapitre montre comment des simulations numérique d'éléments finis peuvent être utilisées afin de modéliser la propagation de la magnétisation dans les systèmes homogènes et hétérogènes en PDN. Nous montrons que les pouvoirs polarisants et pouvoirs relaxants sont des paramètres importants qui influencent grandement la dynamique de tels systèmes. Nous montrons enfin comment l'équation de diffusion en régime permanent est directement liée à la taille des domaines dans les systèmes hétérogènes.

Dans le troisième chapitre, nous comparons les mesures expérimentales aux simulations numériques afin de confirmer la structure des systèmes homogènes. Nous mettons en évidence l'importance de la concentration en protons et électrons, ainsi que plusieurs manières d'augmenter l'efficacité de la polarisation croisée dans les systèmes homogènes.

Enfin, les systèmes hétérogènes sont étudiés dans le chapitre quatre, ou nous combinons à nouveau les expériences et les simulations afin de déterminer des coefficients de diffusion de spin, des tailles de domaines, des structures en oignons, des structures de pérovskites, et comment hyperpolariser l'intérieur de matériaux inorganiques.

Mots-clés

Diffusion de spin, Polarisation Dynamique Nucléaire, Résonance Magnétique Nucléaire

Contents

Chapter 1:
Introduction & Theory

1.1 Nuclear Magnetic Resonance

1.1.1 Basic principles

"Consider a beam of molecules, such as LiCl, traversing a magnetic field which is sufficiently strong to decouple completely the nuclear spins from one another and from the molecular rotation. If a small oscillating magnetic field is applied at right angles to a much larger constant field, a re-orientation of the nuclear spin and magnetic moment with respect to the constant field will occur when the frequency of the oscillating field is close to the Larmor frequency of precession of the particular angular momentum vector in question."[1]

This is how Rabi, in 1938, discovered that nuclei could resonate. And this is how Nuclear Magnetic Resonance, abridged today NMR, was discovered. Few years later in 1946, this discovery was extended to liquids and solids by Bloch[2] and Purcell.[3]

Protons and neutrons that compose a nucleus all possess an intrinsic property: their **spin**. Depending on the number of protons and neutrons that constitute a nucleus, the overall nuclear **spin quantum number** (I) of a nucleus varies. For example, an even number of protons and neutrons leads to I = 0. The nuclear spin number is associated with a **magnetic moment** (μ) by the relation:[4]

$$\mu = \gamma I \tag{1.1}$$

where γ is the **gyromagnetic ratio**. The gyromagnetic ratio is a value that is intrinsic to each given nucleus. The nuclear spin quantum number I can be described as the magnitude of the nuclear spin angular momentum vector which *z*-component (I_z) only takes discrete values. These values are specified by the **magnetic quantum number** (m) that can only vary between +I and -I in integer steps. The *z*-component (μ_z) of the nuclear magnetic moment and the magnetic quantum number are related by:[4]

$$\mu_z = \gamma I_z = \gamma \hbar m \tag{1.2}$$

where $\hbar$ is the reduced Planck constant. For nuclei with I = ½, there are thus two spin eigenstates, known as Zeeman states: m = +½ and m = -½. In the absence of magnetic field, these states have the same energy. Consequently, the number of nuclei in these two states is approximately the same. As a result, the sum of all individual magnetic moment is zero, and no net magnetic moment can be observed due to the nuclear magnetic moment. However, if nuclei are placed in a **magnetic field** (B_0) whose axis defines the z-direction, the two spin states no longer have the same energy. The energy of the spin states becomes:[4]

$$E = -\mu_z B_0 = -\gamma \hbar m B_0 \tag{1.3}$$

where E is the energy of a given spin state defined by m. The energy difference between the two states is thus:

$$\Delta E = \gamma \hbar B_0 = \hbar \omega \tag{1.4}$$

where ω is the **Larmor frequency** of the nucleus in rad.s^{-1}:

$$\omega = 2\pi\nu = \gamma B_0 \tag{1.5}$$

where ν represents the frequency of the electromagnetic radiation in Hz. The Larmor frequency of a given nucleus is fixed and only depends on the type of observed nucleus and the magnetic field strength. However, the actual resonant frequency of a nucleus depends, which is slightly different from the Larmor frequency, mainly depends on its chemical environment in the molecule. This resonant frequency is known as the **chemical shift** (δ).

Since the two states no longer have the same energy, the number of nuclei in each state is different. The relative **spin population** (N) of the energy levels follows a Boltzmann distribution that depends on the energy of the spin state:

$$N \propto e^{-\frac{E}{k_B T}} \tag{1.6}$$

where k_B is the Boltzmann constant, and T the temperature in units of kelvin. Since the lower energy spin state is more populated than the higher energy spin state, the sum of individual magnetic moment no longer cancels out, and the sample gives rise to a **net magnetic moment** (M).

The strength of the net magnetic moment is proportional to the spin population difference of each of these spin states. For nuclei having a spin quantum number I = ½, the spin population difference only depends on the spin populations N_+ and N_- of the two spin states m = +½ and m = -½ respectively. We can define the **polarization** (P) of the sample as:

$$P = \frac{N_+ - N_-}{N_+ + N_-} \tag{1.7}$$

By substituting equation (1.6) into equation (1.7), we get:

$$P = \frac{e^{-\frac{E_+}{k_B T}} - e^{-\frac{E_-}{k_B T}}}{e^{-\frac{E_+}{k_B T}} + e^{-\frac{E_-}{k_B T}}} = \frac{1 - e^{-\frac{\Delta E}{k_B T}}}{1 + e^{-\frac{\Delta E}{k_B T}}} \tag{1.8}$$

and since:

$$\tanh(x) = \frac{e^x - e^{-x}}{e^x + e^{-x}} = \frac{1 - e^{-2x}}{1 + e^{-2x}} \tag{1.9}$$

we finally obtain:

$$P = \tanh\left(\frac{\Delta E}{2 k_B T}\right) = \tanh\left(\frac{\gamma \hbar B_0}{2 k_B T}\right) \tag{1.10}$$

The nuclear polarization is thus a dimensionless quantity varying between 0 and 1 (or 0% and 100%) where 0 corresponds to equal spin population in both spin states, and 1 corresponds to all spins being in either one of the two spin states. **The intensity of the NMR signal is directly related to the strength of the net magnetic moment, and thus to the polarization.** We define the magnetization (M) as:

$$M = C_p \cdot N \cdot P$$

(1.11)

where C_p is the **spin capacity** in units of J.mol^{-1}, and $N = N_+ + N_-$ is the total number of spins. The spin capacity represents the amount of energy of one mole of spins all aligned in the same direction. It is defined as:

$$C_p = \frac{1}{2}\gamma\hbar B_0 N_A$$

(1.12)

where $\frac{1}{2}\gamma\hbar B_0$ is the Zeeman energy of one nuclear spin inside a magnetic field B_0 in units of joule, and N_A Avogadro's number. The polarization is what needs to be increased, but the magnetization is what is measured *in fine*.

1.1.2 Low intrinsic sensitivity

One can see from equation (1.10) that the intensity of the NMR signal is related to the gyromagnetic ratio, the applied magnetic field, and the temperature. If we calculate at the polarization of ^{1}H spins (I = ½, γ_H = 42.58 MHz.T^{-1}) inside a standard magnetic field of 9.4 T at room temperature (T = 300 K), we find **P(^{1}H) ≈ 0.003%**.

It turns out that such a small polarization is not always high enough to generate an electric signal in the detection coil that clearly rises above the electrical noise within satisfactory acquisition times. Consequently when using standard NMR spectrometers at room temperature, we observe that NMR suffers from very low intrinsic sensitivity. This comes from the fact that in NMR, the **involved energies are not big enough**. As shown in Figure 1.1a-b, we see that the NMR frequencies are associated with low intrinsic polarization.

One can see in Figure 1.1b that for systems studied by UV/VIS spectroscopy where the involved particles are electrons, much higher frequencies are involved: in that case, $\Delta E \gg k_B T$ which leads to a bigger energy difference, polarizations close to unity, and bigger measured signals.

This intrinsic low polarization sometimes imposes very long acquisition times in order to be able to observe a clear signal from the sample. The large amount of time required to generate satisfactory NMR signals is currently inhibiting NMR from a wide range of applications (materials with small surface area, low-γ nuclei, diluted spins, nuclei with poorly abundant NMR active isotopes).

But despite the intrinsic low sensitivity of NMR, it is nowadays one of the most widely used technique for molecular level characterization. It can provide useful pieces of information about spatial structure of molecules, dynamics of proteins, or chemical reactions. One of its great advantage is that it is a non-destructive technique, unlike mass spectrometry or chromatography. Nowadays, it is one of the standard techniques used by the large majority of chemical laboratories.
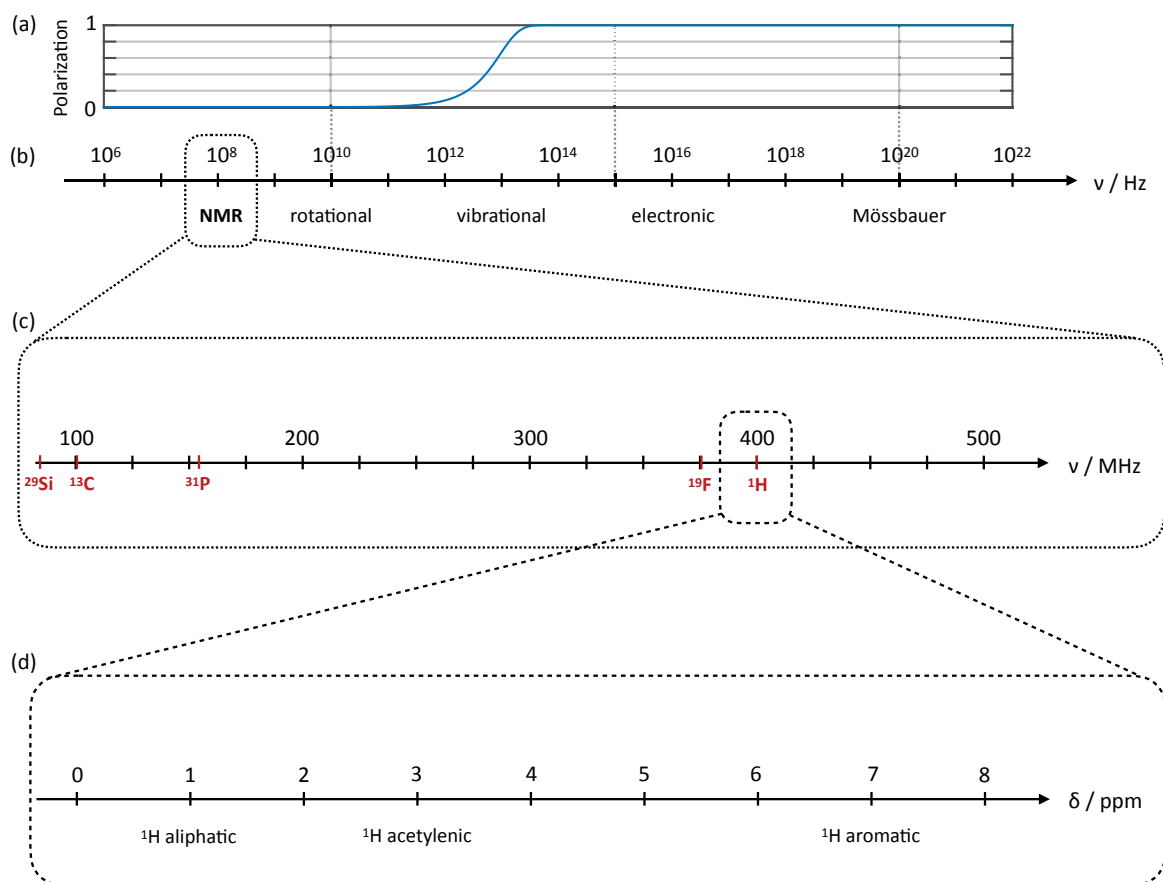
Figure 1.1: (a) Polarization as a function of the involved frequency (axis aligned with panel (b)). (b) Illustration of the electromagnetic spectrum. (c) Zoom on the region of interest for NMR inside a 9.4 T magnet, and Larmor frequencies of different nuclei. (d) Zoom on the region of interest for ^{1}H spins, and typical chemical shifts for different functional groups containing ^{1}H spins.

1.1.3 How to increase sensitivity

Equation 1.10 shows that the nuclear polarization depends on the applied magnetic field and the temperature. **It means that one can increase the nuclear polarization by either increasing the applied magnetic field, or decrease the temperature**.

First, one could plan to increase the strength of the magnetic field. But unfortunately, the strength of the magnetic field cannot be limitlessly increased due to technical limitations. Indeed, the current highest magnet available (35 T in 2018) does not provide high enough nuclear polarizations ($P(^1H) \approx 10^{-4}$). Over the last 50 years, magnetic field strengths have been increased by a factor 10, leading to a factor 10 gain in polarization. But as shown in Figure 1.2, it would still require magnetic fields in order of 10^5 T to provide a polarization close to unity.
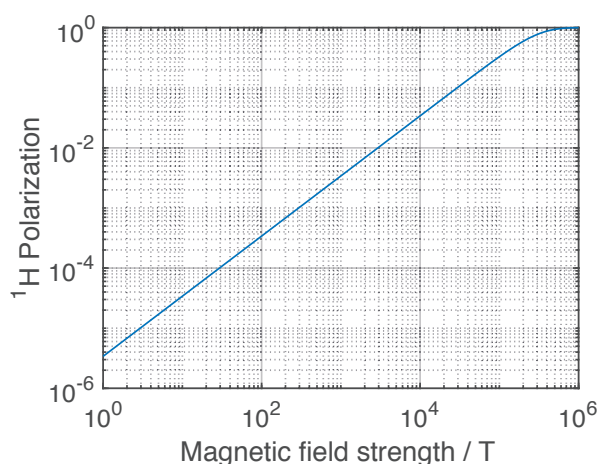
Figure 1.2: ^{1}H polarization as a function of magnetic field strength at 300 K.

One can point out in Figure 1.2 that below 10^5 T, the polarization is a linear function of the magnetic field strength. In this thesis, we will always consider that magnetic fields don't exceed 35 T.

Secondly, one could decrease the temperature in order to increase nuclear polarization. Figure 1.3 shows the temperature dependence of the polarization of electrons and different nuclei. The regions in Figure 1.3 where the polarizations inversely proportional to the temperature (beyond 10 K for electrons) are called the "*high temperature approximation*" regions. It corresponds to the regions where $\Delta E << k_B T$, thus where the hyperbolic tangent functions that describe the polarizations can be approximated as linear functions. In this thesis, unless told otherwise, we will always assume to be in the high temperature approximation.

One can notice in Figure 1.3 that a temperature of 1 K only leads to a ^{1}H polarization of 0.01, which is still far from unity.
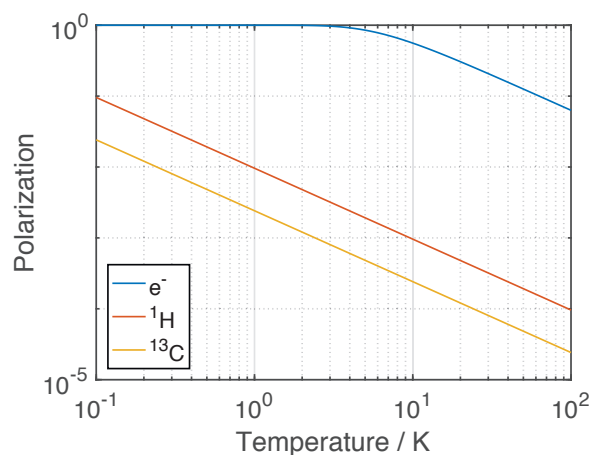
Figure 1.3: Electron, proton, and carbon polarizations as a function of temperature in a 9.4 T magnet.

Moreover, at temperatures on the orders of a few Kelvins, **longitudinal relaxation times** (T_1) that characterize how fast the signal recovers after acquisition can be quite long, which could prevent fast scan repetition, thus leading to long experimental times. Going to very low temperature is thus not ideal for short acquisition times.

One can notice in Figure 1.3 that the ^{13}C polarization is lower than the one of ^{1}H. It means that if one could, somehow, transfer the ^{1}H polarization to a ^{13}C (or ^{15}N, ^{31}P) nucleus, it would lead to a ^{13}C signal enhancement. Such polarization transfer is already achievable via specific pulse sequences such as INEPT[5], NOE[6,7] in liquid state, or **Cross-Polarization** (CP)[8,9] in solid state. These methods allow a polarization transfer from high γ nuclei to low γ nuclei. But the limitation of these methods is that the maximum achievable polarization cannot be higher than the polarization of the highest γ nucleus.

As a result, increasing the nuclear polarization is not as straightforward as it could seem. During the last decades, several techniques were developed in order to increase nuclear polarizations such as Para-Hydrogen,[10] Brute Force Hyperpolarization,[11,12] Optical Pumping,[13,14] or Dynamic Nuclear Polarization.[15,16]

The last technique: **Dynamic Nuclear Polarization** (DNP) is the technique that our laboratory at EPFL is using in order to increase nuclear polarization, as described in the next chapter.

1.2 Dynamic Nuclear Polarization

1.2.1 Theory

One can notice in Figure 1.3 that the electronic polarization is much bigger than the one of ^{1}H or ^{13}C spins. This is due to the intrinsic much higher electronic gyromagnetic ratio. Indeed, one can calculate that:

$$\frac{\gamma_e}{\gamma_H} \approx 658 \qquad (1.13)$$

where γ_e and γ_H represent the electronic and proton gyromagnetic ratios respectively. If proton spins could reach the electrons' thermal polarization, the theoretical maximum ^{1}H **signal enhancement** (ε) achievable is defined as:

$$\varepsilon = \frac{P_e}{P_H} = \frac{\tanh\left(\frac{\gamma_e \hbar B_0}{2 k_B T}\right)}{\tanh\left(\frac{\gamma_H \hbar B_0}{2 k_B T}\right)} \approx 658 \text{ for T = 100 K} \qquad (\approx 104 \text{ for T = 1 K}) \qquad (1.14)$$

where P_e and P_H represent the electronic and ^{1}H polarizations respectively.

It can be seen in equation (1.14) that the enhancement depends on the gyromagnetic ratios of the considered nuclei, the magnetic field strength, and the temperature. The electron/proton enhancement is thus different from the electron/carbon enhancement. Also, one can see that the enhancement is smaller at low temperatures, even though absolute polarizations are much bigger (approximately 10^{-2} at 1 K compared to 10^{-4} at 100 K for ^{1}H).

If one could try to use the high electronic polarization as a source of ^{1}H polarization, it would increase by several orders of magnitude the ^{1}H polarization, leading to much bigger signals, and much smaller acquisition times.

The basic idea of Dynamic Nuclear Polarization (DNP) is to transfer the high electronic polarization to coupled nuclei, in order to obtain ^{1}H polarizations much closer to unity in achievable field and temperatures. But the problem is that the electrons available in electronic orbitals of the atoms present in the sample are not good candidates, which means there is no polarization to be transferred here. The reason is that electrons in the electronic orbitals of *most* molecules are always paired. Consequently, their total spin quantum number is S = 0, which makes them non[*] magnetically active. It is thus necessary somehow have present some unpaired electrons in the system.

Albert W. Overhauser predicted in 1953[7] that "*the interaction between the electron spin magnetic moment and the nuclear spin magnetic moment*" could lead to a polarization transfer in a metallic solids possessing **unpaired electrons** in its conduction bands. The same year, Carver and Slichter confirmed the predictions of Overhauser by measuring for the first time a DNP enhanced signal of ^{7}Li in a static magnetic field.[17] Later on in 1959, Abraham[15] confirmed the possibility of enhancing ^{1}H, ^{27}Al, ^{59}Co, and ^{19}F

---

[*] they are actually very weakly magnetically active, since the observable chemical shift difference between nuclei is due to the presence of electrons in the electronic orbitals

nuclei thanks to the presence of paramagnetic impurities via microwave irradiation. Major contributions of Goldman[18] and Abragam[19] to the DNP field in the early years must also be acknowledged.

In order to drive the DNP mechanism, it is thus necessary to introduce some unpaired electrons in the system. In DNP, we usually add to the sample some paramagnetic agents that contain stable unpaired electrons. After the paramagnetic agents and the compound to be studied are mixed together, the sample is usually frozen in order to maximize the DNP efficiency as described later. Then, a microwave source is used to trigger the polarization transfer from the unpaired electron(s) to the desired nuclei. The high electron polarization is transferred to coupled nuclei via different mechanisms. Up to now, 4 different mechanisms have been described in the literature. They are known as **Solid Effect**,[20,21] **Cross Effect**,[22,23] **Thermal Mixing**,[24,25] and **Overhauser Effect**.[7] Once the mechanism is complete, the resulting sample contains hyperpolarized nuclear spins (usually protons) that can be detected through conventional techniques that require much less acquisition time.

If the acquisition is desired to be done in the solid state, a technique that is particularly suited known as **Magic Angle Spinning DNP** (MAS DNP) will be described in the section 1.2.2. However if the acquisition is needed to be performed in the liquid state, the technique called **Dissolution-DNP** (dDNP) is more appropriate, as described in section 1.2.3.

1.2.2 Magic Angle Spinning DNP

Magic Angle Spinning (MAS) DNP is the combination of MAS NMR and DNP. MAS NMR was invented by Andrew[26] *et al.* in 1958. Later on in 1984, DNP MAS was developed by Vriend *et al.*[27] but only became popular with the remarkable work of Griffin *et al.* in 1993.[28] In DNP MAS at EPFL, the experiment is performed in a temperature range between 85 K and 110 K. The main advantage is that this temperature range is accessible by cooling the sample with gas nitrogen. Consequently, one can spin the sample at the magic angle with cold gas nitrogen and perform experiments with satisfactory ^{1}H resolution. The experimental set up of DNP MAS is presented in Figure 1.4. Some recent technical advances have enabled the establishment of a set up capable of running DNP MAS experiments at ≈ 25 K using Helium gas.[29]
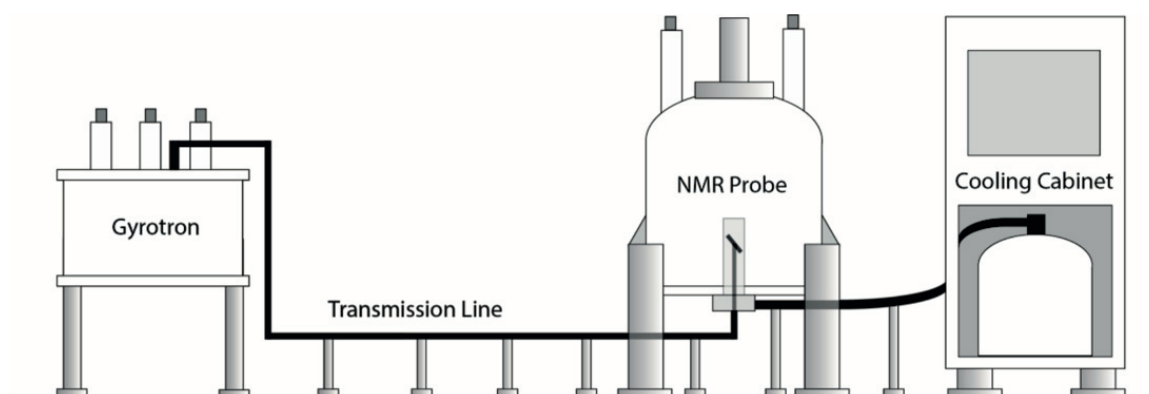
Figure 1.4: Schematic representation of the overall MAS DNP system in our laboratory at EPFL. Gyrotrons operating at 263 GHz or 593 GHz are connected via a transmission line to a 400 MHz or 900 MHz NMR spectrometer respectively. A cooling cabinet allows the sample in the NMR probe to be kept in a temperature range from 85 to 325 K while spinning from 1 to 15 kHz. Scheme reproduced with permission from the original work.[30]

Gyrotrons generate microwaves by employing the phenomenon of cyclotron resonance. The presence of a strong external magnetic field and a strong voltage difference creates a highly accelerated electron beam. The electrons radiate electromagnetic waves, creating microwave emissions. The microwaves are then converted to a Gaussian beam and transmitted to the probe using a transmission line, consisting of a corrugated waveguide. The DNP probe is kept at around 100 K with a cooling cabinet permanently blowing cold N_2 gas, while the microwaves propagate through the waveguide all the way to the MAS stator which has an opening at the bottom. This set-up allows the delivery of microwave powers on the order of 10-50 W, allowing efficient DNP at 100 K.

In a MAS DNP experiment, the sample is put into contact with a paramagnetic species such as BDPA, nitroxide or trityl radicals. Usually, the analyte to be hyperpolarized is dissolved in a solvent that already contains radical molecules. In order to optimize the DNP effect in a mixture of analyte-solvent-radical, the mixture needs to fulfil at least the following 4 conditions:

1. The solvent must solubilize the radical molecules: the radical molecules must be homogeneously dispersed in the solvent. Indeed, if the molecules are too close in space, strong electron-electron dipolar couplings shorten their intrinsic electronic relaxation times (T_{1e} & T_{2e}), preventing efficient DNP effect from occurring.[31]

2. The radical molecules must be present at an optimal concentration: two few radical molecules don't provide enough energy to polarize the entire sample, and too high radical concentration reinforces electron-electron dipolar coupling as explained above.

3. The solvent must form a glassy matrix once frozen: if the solvent crystallizes, radical molecules are segregated in restricted areas, inducing strong electron-electron dipolar coupling as explained above.

4. ^{1}H spins must be present at an optimal concentration: too many ^{1}H spins won't be efficiently polarized by a small number of electrons, while too few ^{1}H spins have high polarizations but small net magnetization.

By looking at these criteria, one can already see some of the challenges brought by the DNP formulation: does one want the highest polarization, or the highest magnetization? Where is the optimum between the number of ^{1}H spins and the number of electron spins? In order to answer these questions, one has to understand the dynamics of such a system. These questions will be answered in chapter 3, where a detailed and comprehensive description of homogeneous radical solutions will be made.

1.2.3 Dissolution DNP

Dissolution DNP (dDNP) was introduced by Ardenkjær-Larsen *et al.*[32] in 2003 when he showed for the first time that DNP could be used to generate hyperpolarized liquids. The idea of dDNP is to divide the set up in 3 distinct parts: (1) The sample is polarized at very low temperature (around 1 K) in the solid state, (2) the sample is rapidly melted and transferred to a NMR spectrometer where (3) the acquisition of the hyperpolarized sample is done in the liquid state. It is based on the idea that hyperpolarization can be most efficiently generated at low temperature and that hyperpolarization survives the solid/liquid phase transition. With this method, it is possible to obtain high sensitivity and high resolution spectra. However, the drawback is that only a single scan in the liquid state is allowed, since the hyperpolarization is lost after the first scan.

As for a MAS DNP experiment, the sample is put into contact with a paramagnetic species that possess long electronic relaxation times T_{1e}. Then, the sample is cooled down to very low temperatures in a 6.7 T polarizer at EPFL. To achieve temperatures as low as 1.2 K, the sample is put under reduced pressure (typically 0.8 mbar) in a continuous-flow cryostat. Once the sample reaches the desired temperature, the sample can be hyperpolarized using DNP.[33]

The sample is irradiated with microwaves that trigger the DNP effect via some of the DNP mechanisms mentioned earlier. The frequency of the microwaves is optimized in order to maximize the ^{1}H polarization (188 GHz optimal frequency at 6.7 T). In addition to that, frequency modulation is applied in order to increase even more the efficiency of the DNP effect and decrease the optimal radical concentration.[34] The microwaves are guided down to the sample through a home-built DNP probe.[35] During irradiation, spin populations are mixed between the electrons and the coupled ^{1}H spins, leading to high ^{1}H polarizations. The DNP build-up can take up to several hours. Once the steady state is reached, ^{1}H spins can theoretically reach a polarization as high as 100%.

Then, the frozen hyperpolarized sample is ready to be dissolved. The dissolution is usually done by adding a solution of 5 mL of superheated (1 MPa) D_2O. In the course of a few seconds, the sample is melted and pushed with high pressure Helium gas to the NMR spectrometer through a magnetic tunnel.[36] The transfer must be done through a magnetic tunnel in order to always keep the sample in a magnetic field higher than the earth's field (35 µT). Indeed, if the sample is at any point of the trip located in such a small magnetic field at room temperature, both cross-relaxation effects and short relaxation times become fatal to the survival of hyperpolarization.

Once the hyperpolarized liquid sample is in the NMR spectrometer (typically 11.7 T at EPFL), it is ready to be detected. The acquisition is done only with one scan, since the hyperpolarization cannot be recovered after the first scan. The survival of the polarization in the NMR spectrometer at room temperature is determined by T_1 of the nuclei of interest. The longer the T_1, the longer the hyperpolarization lasts during transfer and acquisition. The presence of the radical molecule has two main consequences. The first one is obviously the triggering of the DNP effect. The second effect of the presence of radical molecules is the **Paramagnetic Relaxation Enhancement** (PRE) effect.[37,38] The PRE effect induces shorter T_1's in the liquid state. The PRE effect will be described in more details in section 1.4.2. In order to increase the lifetime of the hyperpolarization after dissolution, many techniques have been developed.[39-44] Today, sample hyperpolarization can be preserved up to a few minutes after the dissolution process, allowing the hyperpolarization of a wide range of substrates.[45,46]

The set-up of a typical dDNP experiment is schematized in Figure 1.5.
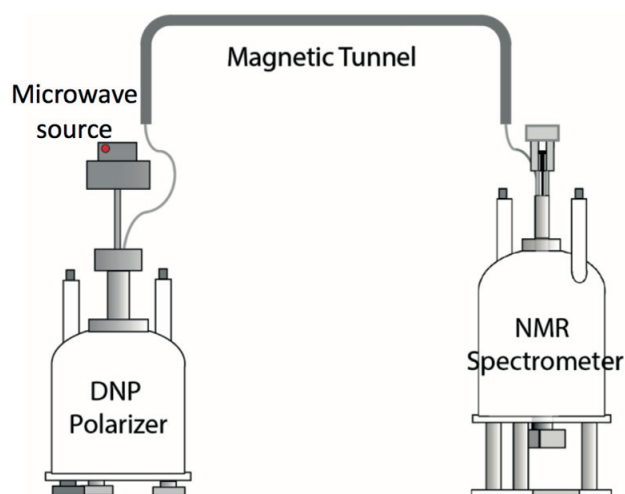
Figure 1.5: Schematic representation of the overall dDNP setup at the EPFL composed of a DNP polarizer, a microwave source, a magnetic tunnel and a NMR spectrometer (500 MHz). Scheme reproduced with permission from the original work.[30]

MAS DNP and dDNP are two hyperpolarization techniques that both require the addition of paramagnetic species in the sample. Polarization dynamics in the presence of paramagnetic species are significantly different than in diamagnetic samples. In order to understand polarization dynamics of DNP samples, one has first to understand the most important aspect of it: **Spin Diffusion**.

1.3 Spin Diffusion

In this section, we first introduce some simple concepts used in NMR, that can be found with more details in several articles and textbooks.[4,18,37,47-49] In order to explain the spin diffusion process, one must first take a look at the interaction that drives spin diffusion: the **dipolar coupling** interaction. We will then introduce the **spin diffusion coefficient**, and we will see in which cases spin diffusion can or cannot occur. Finally, we will study polarization dynamics in systems that contain paramagnets. In particular, we will see how **polarization**, **relaxation times**, and the **spin diffusion coefficient** are affected by the presence of paramagnetic species.

1.3.1 Dipolar interactions

In this section, we introduce the concept of dipolar coupling, and we show how dipolar couplings can trigger energy conserving flip-flop transitions.

Every active nuclear spin generates its own magnetic field oriented parallel to the nuclear spin vector. Consequently, two spins that are close to each other in space experience each other's magnetic field, which leads to a slightly different effective magnetic field B_{eff} at one spin. The strength of this coupling, called the dipolar coupling, mainly depends on:

1. the spin-spin distance r
2. the gyromagnetic ratios of the coupled spins γ

The secular dipolar coupling Hamiltonian of two spins I and S is given by:

$$H_D = d \cdot \left(2I_z S_z - \left(I_x S_x + I_y S_y \right) \right) \tag{1.15}$$

where d represents the **strength of the dipolar coupling**:

$$d = \frac{\gamma_I \gamma_S \hbar}{4\pi^2 r^3} [1 - 3\cos^2\theta] \tag{1.16}$$

where θ is the angle between the inter-spin vector and the external magnetic field, and r the distance between spins. In liquid state, molecular tumbling reduced the average value of d to zero. In solids, this value is different from zero.

When the sample is spun at the magic angle, the strength of the dipolar coupling between spins is progressively averaged out as the spinning frequency v_r (in Hz) increases. Maricq and Waugh[50] demonstrated from the Hamiltonian theory that the **effective dipolar coupling** of a rotating sample in Hz is given by:

$$d_{\text{MAS}} \propto \frac{d^2}{4\pi^2 v_r} \tag{1.17}$$

One must note that equation (1.17) diverges for v_r = 0: in the following, we will only consider MAS frequencies greater than 2 kHz. For a static sample, the effective dipolar coupling is simply proportional

to $d^2/4\pi^2$. By combining equation (1.16) and (1.17), one can see that the effective dipolar coupling depends on r^{-6}.

For a set of randomly dispersed spins in a given fixed volume, the average distance r between spins is directly linked to the concentration by the **Wigner-Seitz radius**[51] (r_{WS}) by the relation:

$$r = 2 \cdot r_{WS} = 2 \left(\frac{3}{4\pi C N_A} \right)^{1/3} \tag{1.18}$$

where C is the nuclear concentration, and N_A is Avogadro's number. The nuclear concentration is easily obtained from the density ρ and the molar mass M of the desired compound:

$$C = \frac{\rho n x}{M} \tag{1.19}$$

where n is the number of nuclei per molecule and x the nuclear natural isotopic abundance if the molecule is not labelled. Equation (1.18) allows use to directly link the radical concentration and the average separation between radical molecules in homogeneous frozen solutions as shown in Figure 1.6. For example, the proton concentration in water is 111 M which corresponds to an average distance between protons of 0.3 nm. Analogously, a radical concentration of 12 mM corresponds to an average distance between radical molecules of 6.3 nm.
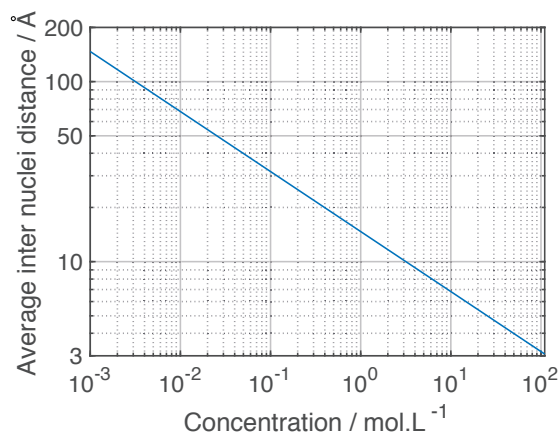
Figure 1.6: Average separation between spins as a function of the spin concentration for a set or randomly distributed spins in a given fixed volume.

Typical values of the effective dipolar coupling between identical spins under MAS is given in Figure 1.7 for various spins ½ nuclei in a sample spinning at 12.5 kHz.
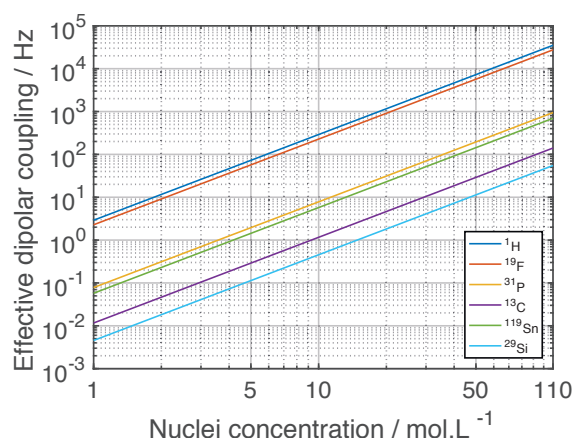
Figure 1.7: Effective dipolar coupling between two identical nuclei as a function of the nuclear concentration in a sample spinning at 12.5 kHz at the magic angle.

It becomes interesting to compare the effective dipolar coupling of a sample with the Zeeman energy of its nuclei. For water ($[^1H]$ = 111 M) in a magnetic field of 9.4 T in a sample spinning at 12.5 kHz, the effective dipolar coupling is on the order of tens of kHz, whereas the proton Zeeman energy is by definition 400 MHz. As expected here, the dipolar energy is much smaller than the Zeeman energy. It means that the dipolar coupling between two ^1H spins is not strong enough to induce a spontaneous flip of one of the spins. This transition is called a "forbidden transition". It means that **the probability W that such a transition would happen is small**.

On the contrary if two ^1H spins with the <u>same</u> total Zeeman energy are willing to proceed to a spontaneous flip-flop transition, the total energy of the system would remain unchanged. The process is energy conservative, the lattice doesn't participate, the transition occurs spontaneously. It is called an "allowed transition". Both cases are schematized in Figure 1.8:

(a)   (b)

Forbidden transition   **Allowed transition**
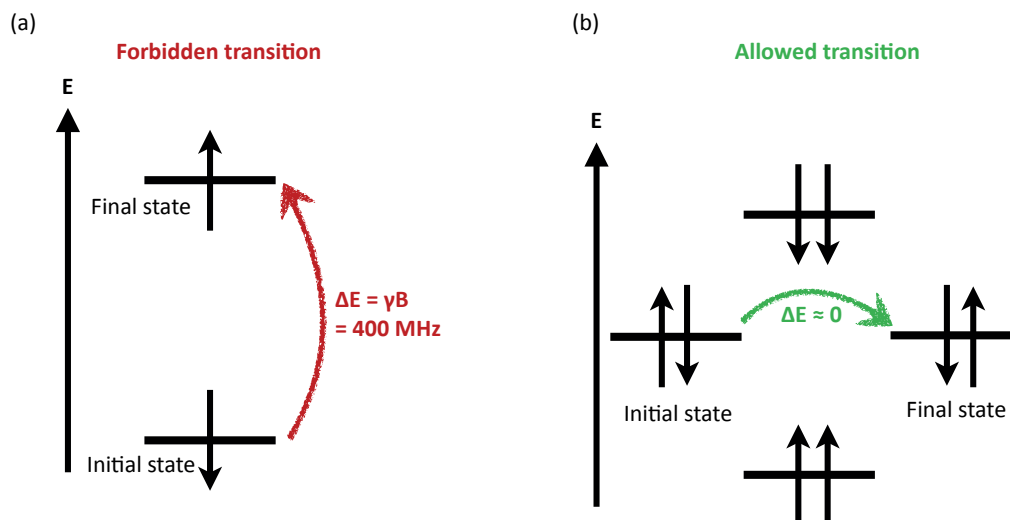
Figure 1.8: Schematic representation of (a) a forbidden transition of a single spin flip, and an (b) an allowed transition of a mutual flip-flop.

The process that describes the allowed transition wherein individual spins undergo an exchange of energy via a mutual flip-flop is called **Spin Diffusion**. We see that spin diffusion is thus a process that relies on dipolar coupling between nuclei that have sufficiently close energies. This process is characterized by the **spin diffusion coefficient** that will be defined in the next section.

1.3.2 Spin diffusion coefficient

In this section, we introduce the spin diffusion coefficient, how this coefficient varies with the gyromagnetic ratio and the spin concentration, and give several numerical values of the spin diffusion coefficient for static samples.

Bloembergen in 1949,[37] followed by Blumberg[52] and Khutsishvili[53] studied the energy operator of the dipolar interaction that causes flip-flop transitions in order to calculate the **flip-flop transition rate W_{ij}** between two identical nearest neighbours i and j separated by a distance r_{ij} in a cubic lattice. This probability is given by:

$$W_{ij} = \frac{1}{8\sqrt{2}} \hbar^2 \gamma^4 T_2 \left[1 - 3\cos^2(\theta_{ij})\right]^2 r_{ij}^{-6}$$

(1.20)

where T_2 is the transverse relaxation time of the nuclear spins. The transition rate W_{ij} depends on the orientation θ_{ij} of the inter-spin vector relative to the external magnetic field. According to Bloembergen since the transition rate diminishes with the sixth power of the distance between spins, the transport of polarization can almost only occur between nearest neighbours, and can therefore be represented as a random walk. Macroscopically, such a random walk is described by a diffusion equation. Bloembergen showed that the **z component of the bulk magnetization M** was described by the following diffusion equation:

$$\frac{\partial M(x,t)}{\partial t} = \sum_{j \neq i} W_{ij} \cdot r_{ij}^2 \cdot \frac{\partial^2 M(x,t)}{\partial x^2}$$

(1.21)

where M is the magnetization, r is the distance between nearest neighbours, and x the position in space. In three dimensions, equation (1.21) becomes:[53]

$$\frac{\partial M(x,t)}{\partial t} = D \cdot \Delta M(x,t)$$

(1.22)

where

$$D \stackrel{\text{def}}{=} \sum_{j \neq i} W_{ij} \cdot r_{ij}^2$$

(1.23)

describes the **nuclear spin diffusion coefficient** in $\mu m^2.s^{-1}$, and ΔM is the Laplacian of the magnetization. Physically, the spin diffusion coefficient describes how fast bulk magnetization can be transported over space. The time required to transport the magnetization M over a distance r is on the order of $t = r^2/(4D)$. The distance $r = (Dt)^{\frac{1}{2}}$ is called the **characteristic spin diffusion length**. It represents the length that spin diffusion can travel in a time t. Since:[53]

$$T_2 = 0.65 \frac{r^3}{\hbar \gamma^2}$$

(1.24)

we combine equations (1.20), (1.23) and (1.24) to obtain:

$$D \propto \frac{\gamma^2}{r} \propto \gamma^2 C^{1/3} \qquad (1.25)$$

Consequently, two of the factors that influence the probability of a mutual flip-flop transition (and thus the diffusion coefficient) are the **concentration of nuclear spins** (i.e. the average separation between spins), and their **gyromagnetic ratio**. In addition, magic angle spinning, chemical shift anisotropy, or chemical shift differences can also influence the spin diffusion coefficient.

In the case of a polycrystalline solid (i.e. a powder), the spin diffusion coefficient can be estimated as:[53]

$$D = \frac{r^2}{12 \cdot T_2} \qquad (1.26)$$

Typical values of the predicted spin diffusion coefficient from equation (1.26) are graphically represented in Figure 1.9:
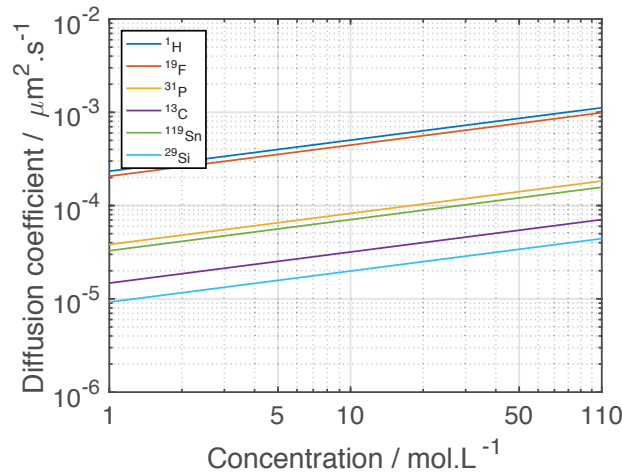
Figure 1.9: Predicted spin diffusion coefficient for various nuclei as a function of nuclear concentration.

Looking at Figure 1.9 one can observe that the predicted ^{1}H spin diffusion coefficient in polystyrene ([^{1}H] = 70 M) is on the order of 10^{-3} $\mu m^2 s^{-1}$. We will see in chapter 4 that the measured spin diffusion coefficients are smaller than the one predicted in Figure 1.9 since here magic angle spinning, chemical shift anisotropy, or chemical shift differences are not taken into account.

The previous calculations were made in the case of identical spins displaying the same energy. One can wonder if nuclear spin diffusion can still occur in the case where spins possess different energies? We will examine these cases in the next section.

1.3.3 Criteria for spin diffusion

In this section, we examine how efficient spin diffusion is among nuclei that don't possess similar nuclear frequencies and establish simple criteria. We introduce the concept of proton-driven spin diffusion, and how spin diffusion can be enhanced by adding external energy to the system.

Spin diffusion among nuclear spins displaying different nuclear frequency is called **spectral diffusion**. This process has been extensively studied by Suter and Ernst,[54] but we only give simple guidelines here. When considering a system where spins display a Gaussian distribution of frequencies, it is necessary to establish a criterion for spin diffusion. In order for spin diffusion to occur, the chemical shift difference must be smaller than the effective dipolar coupling between the two nuclei. In the case of identical spins displaying a Gaussian distribution of frequencies, we state that:

Homonuclear spin diffusion becomes substantial when $\Delta\omega < d_{AB}(v_r)$

where $\Delta\omega$ is the width of the Gaussian distribution.

For the heteronuclear case the principle is the same: among the previously plotted nuclei, the ones that are the closest in frequency are ^1H and ^{19}F. Inside a 9.4 T magnet, the frequency difference is 23.6 MHz. The effective dipolar coupling between ^1H and ^{19}F in a sample with a spin concentration of 50 M is on the order of tens of kHz for a sample spinning at 12.5 kHz. As expected, the difference in Larmor frequencies is much bigger than the effective ^1H-^{19}F dipolar coupling. Consequently, no nuclear spin diffusion is possible between ^1H and ^{19}F at 9.4 T. We can thus create a simple general criterion for heteronuclear spin diffusion:

Heteronuclear spin diffusion becomes substantial when $|\omega_A\text{-}\omega_B| < d_{AB}(v_r)$

Here, the word "substantial" means that nuclear spin diffusion travels atomic length scales in a time shorter than an average NMR experiment (hours). In the described case of a mixture of ^1H and ^{19}F, the time required for magnetization to travel 1 nm is of about 2 hours. Consequently, heteronuclear spin diffusion is not observable by NMR with high fields. The flip-flop process in the case of two spins is schematized in Figure 1.10.
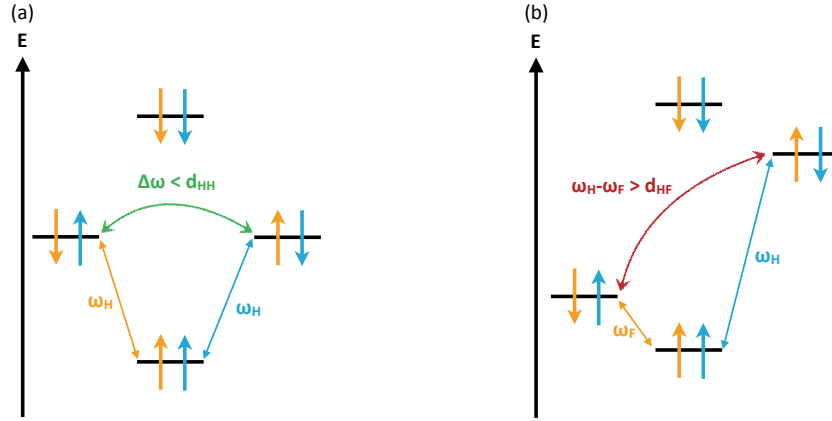
Figure 1.10: Schematic representation of a two spin system with (a) an allowed flip-flop when spins have identical frequencies, and an (b) a forbidden flip-flop transition of spins with different frequencies (here ^{1}H and ^{19}F) at high field. d_{HH} and d_{HF} represent the effective dipolar coupling.

Let's consider a general case where two spins of the same kind S display a chemical shift offset δ. When spins S are in the presence of abundant nearby spin I (e.g. S = ^{19}F spins in the presence of nearby I = ^{1}H spins), S-S spin diffusion can be enhanced by I-I flip-flops. The phenomenon is called **proton-driven spin diffusion**. In such cases, the probability W_{SS} of a S-S flip-flop transition between S spins was determined by Suter & Ernst [54] to be:

$$W_{SS} = \frac{1}{T_2^{ZQT}} \frac{b_{SS}^2}{\left(\frac{1}{T_2^{ZQT}}\right)^2 + \Omega^2}$$

(1.27)

where b_{SS} is the S-S dipolar coupling, Ω the chemical shift difference, and $1/T_2^{ZQT}$ encodes the contribution from spins I as:

$$\frac{1}{T_2^{ZQT}} \propto b_{II} \cdot b_{IS}$$

(1.28)

where b_{II} and b_{IS} encode the I-I and I-S dipolar coupling respectively.

It is also possible to enhance spin diffusion by bringing some energy to the system in order to foster flip-flop transition rates, by irradiating the system with long-wavelength acoustic phonons waves, called phonon-assisted spin diffusion.[55]

Another way of increasing spin diffusion is to decrease the magnetic field strength B_0 so that the difference in Larmor frequencies becomes on the order of the effective heteronuclear dipolar coupling. In the case where the field is sufficiently small, spontaneous spin diffusion can occur.

A similar phenomenon occurs when a radio frequency (RF) field is applied to trigger Cross Polarization,[8,9] the magnetic field B_1 brings few kHz of energy to the nuclei in the rotating frame. In this case, the

criterion is satisfied, mutual flip-flop can occur in the rotating frame, and magnetization is spontaneously exchange between non identical nuclei. Triggering nuclear spin diffusion under radio frequency irradiation is a technique called **RF-driven spin diffusion** and has already allowed the enhancement of ^{13}C spin diffusion by two orders of magnitude.[56]

One last method is to lift the sample up from the magnet for a few milliseconds so that the effective magnetic field is lower than the effective dipolar coupling. This technique is known as the **Low Field Thermal Mixing** and has allowed successful polarization transfers between ^{1}H and ^{13}C spins.[19]

Now that the spin diffusion coefficient is defined, we want to show how it is affected in DNP systems due to the presence of paramagnets, as described in the next section.

1.4 Presence of paramagnets

The presence of a DNP effect cannot occur without the presence of paramagnets. Usually in DNP, these paramagnets are carbon or oxygen based stable radicals. We show in this section that the presence of free electrons substantially changes magnetization dynamics in the sample. The first observed effect is the change in the spin diffusion coefficient, and the second effect is the change in the relaxation times called **paramagnetic relaxation enhancement** (**PRE**), leading to a quenching barrier and short T_1s.

1.4.1 Spin diffusion barrier

In this section, we show how the presence of a free electron can inhibit spin diffusion in its nearest environment, and try to find an estimate of the size of the volume where this inhibition occurs.

As mentioned earlier, the presence of a strong coupling between a free electron and nearby nuclei has consequences. Nuclear spins in an inner core around the paramagnet experience a large local field gradient due to the electron spin and as a consequence have significantly different effective Zeeman energies. Khutsishvili was the first to define the radius of the "**spin diffusion barrier**" as the distance r_b from the electron at which the difference of the hyperfine-shifted Zeeman frequencies of two neighbouring nuclei is equal to the dipolar-broadened NMR line width.[53] Bloembergen and Blumberg defined it as the distance where the electron-nucleus dipolar coupling d_{H-e} is equal to the nucleus-nucleus dipolar coupling d_{H-H}.[37,52] The spin diffusion barrier physically represents the distance from the electron below which spin diffusion is significantly reduced due to the proximity of the electron spin. By equalizing the electron-nucleus and nucleus-nucleus dipolar couplings from equation (1.16), one gets:

$$\frac{\gamma_e \gamma_H}{r_{eH}^3} = \frac{\gamma_H \gamma_H}{r_{HH}^3} \tag{1.29}$$

leading to

$$r_{eH} = r_{HH} \left(\frac{\gamma_e}{\gamma_H}\right)^\alpha \overset{\text{def}}{=} r_b \tag{1.30}$$

Blumberg's definition leads naturally to $\alpha = 1/3$ whereas Khutsishvili's definition leads to $\alpha = ¼$, leading to a slightly different diffusion barrier. If the z component of the electron spin is fluctuating rapidly in a $T_2(^1H)$ time (i.e. $T_{1e} < T_2(^1H)$), the local field on the electron is averaged out and only this averaged field is felt by the nearby nucleus. The equation (1.30) must then be modified:[52,53]

$$r_b \overset{\text{def}}{=} r_{HH} \left(\frac{\gamma_e}{\gamma_H} B_S \left(\frac{\hbar \gamma_e B_0}{2 k_B T}\right)\right)^\alpha \tag{1.31}$$

where B_s is the Brillouin function and B_0 the main magnetic field strength. The first observation on equation (1.31) is that the spin diffusion barrier depends on the nuclear concentration. Using the definition given by Blumberg, Goldman[57] predicted the radius of the spin diffusion barrier in paradibromobenzene ($[^1H] = 39$ M) to be $r_b = 1.7$ nm. Schmugge and Jeffries[58] estimated the size of the barrier in Nd-doped lanthanum magnesium nitrate ($[^1H] = 40$ M) to be $r_b = 1.6$ nm, on the basis of the same model. However, experiments on calcium fluoride by Lowe and Tse suggested that the diffusion barrier was in fact smaller than this.[59] Ramakrishna and Robinson[60] were able to study the dynamics of

the protons close to a paramagnetic site and found that a spin diffusion barrier of r_b = 0.7 nm, which is even smaller than the value predicted by Khutsishvili's theory (r_b = 0.9 nm). Using high-sensitivity NMR techniques to directly detect the nuclei close to the paramagnetic impurity, Wolfe *et al.* were able to directly probe the thermal contact between these hyperfine-shifted nuclei and the bulk nuclear spins. They observed that very few spins were not in thermal contact with the bulk and that the diffusion barrier only contained 1 to 2 shells of nuclear spins around the impurity, indicating a barrier on the order of 0.3 nm.[61] Bloembergen[37] suggested that the transport through the spin diffusion barrier could be facilitated by the fluctuation of the electron spin itself. This theory was confirmed by Wolfe's experiments in doped calcium fluoride solids.[61] It is also possible that the size of the diffusion barrier changes during microwave irradiation.[58] Ramakrishna was even able to observe an anisotropy of the spin diffusion barrier.[62] Besides, the spin diffusion barrier radius can be modified by the MAS rate due to frequency fluctuation. Finally, dipolar and hyperfine interactions are anisotropic, which suggest a non-spherical spin diffusion barrier (Figure 1.11).

In this thesis, we will follow experimental results, and consider that the spin diffusion coefficient inside a radius of r_b = 0.5-1.0 nm will be reduced.

1.4.2 Paramagnetic relaxation enhancement

In this section, we examine how transverse and longitudinal relaxation times are influenced by the presence of a free electron. We then introduce a way of determining if the paramagnetic relaxation enhancement (PRE) effect is stronger or weaker than spin diffusion in paramagnetic samples, in order to know if the PRE effect is a diffusion-limited process or not.

In 1949 Bloembergen[37] demonstrated that NMR relaxation in solids containing paramagnets was mediated by nuclear spin diffusion from the bulk to the sites of paramagnets, and that T_1's were significantly shortened at increased paramagnet concentrations. The dynamics of the nuclear magnetization (M) can therefore be described by a diffusion equation modified from equation (1.22):

$$\frac{\partial M(r,t)}{\partial t} = D\Delta M - \frac{M(r,t) - M_0(r)}{T_1(r)} \tag{1.32}$$

where D is the nuclear spin diffusion coefficient, and T_1 describes the time constant of nuclear spins at a distance r from the paramagnet. Solomon & Bloembergen[37,38,63,64] demonstrated that the longitudinal and transverse relaxation times $T_{1/2}$ were the sum of the paramagnetic and diamagnetic contributions:

$$\frac{1}{T_{1/2}(r)} = \frac{1}{T_{1/2,para}(r)} + \frac{1}{T_{1/2,dia}} \tag{1.33}$$

where

$$\frac{1}{T_{1,para}(r)} = \frac{2}{15}\left(\frac{\mu_0}{4\pi}\right)^2 \frac{\gamma_n^2 g_e^2 \mu_B^2 S(S+1)}{r^6}$$

$$\left[\frac{\tau}{1+(\omega_n-\omega_e)^2\tau^2} + \frac{3\tau}{1+(\omega_n-\omega_e)^2\tau^2} + \frac{6\tau}{1+(\omega_n-\omega_e)^2\tau^2}\right] \stackrel{\text{def}}{=} \frac{K_1}{r^6} \tag{1.34}$$

and

$$\frac{1}{T_{2,para}(r)} = \frac{1}{15}\left(\frac{\mu_0}{4\pi}\right)^2 \frac{\gamma_n^2 g_e^2 \mu_B^2 S(S+1)}{r^6}$$

$$\left[4\tau + \frac{\tau}{1+(\omega_n-\omega_e)^2\tau^2} + \frac{3\tau}{1+(\omega_n-\omega_e)^2\tau^2} + \frac{6\tau}{1+(\omega_n-\omega_e)^2\tau^2} + \frac{6\tau}{1+\omega_e^2\tau^2}\right] \stackrel{\text{def}}{=} \frac{K_2}{r^6} \tag{1.35}$$

represent the relaxation contribution of the PRE effect. In equations (1.34) and (1.35), μ_0 is the vacuum permittivity, γ_n is the gyromagnetic ratio of the nucleus, r the distance between the nucleus and the electron, g_e the electron spin g-factor, τ the electronic correlation time, S the total electronic spin number, and $\omega_{e/n}$ the electron/nuclear Larmor frequency. In solid systems where the interactions between free electrons can be neglected, τ becomes the longitudinal/transverse relaxation time of the electron $T_{1e/2e}$.[52,64] We note that Lowe & Tse,[59] studied the PRE effect on longitudinal relaxation times in the rotating frame $T_{1\rho}$, where they showed that the PRE effect could be smaller than in the laboratory frame.

Equation (1.33) describes the direct PRE effect <u>alone</u> (i.e. without taking into account nuclear spin diffusion). Only considering these equations to study polarization dynamics would mean that the relaxation time of each individual nucleus only depends on its distance from the free electron. However,

spin diffusion is capable of relaying this PRE effect. It becomes interesting to determine which effect dominates polarization dynamics: PRE, or nuclear spin diffusion?

De Gennes defined the **peusopotential** ρ_1 which characterizes the competition between the PRE and spin diffusion.[65] He defines:

$$\rho_1 = 0.68 \left(\frac{K_1}{D}\right)^{1/4} \tag{1.36}$$

where K_1 represents the PRE contribution to longitudinal relaxation times from equation (1.34) and D represents the spin diffusion contribution. ρ_1 represents the distance from the electron where spin diffusion and PRE effect are compensating each other. Beyond this distance, spin diffusion can relay the PRE effect, and below this length the PRE effect is too strong. It means that if the pseudopotential ρ_1 is smaller than the length scale involved, i.e. the Wigner-Seitz radius, spin diffusion averages out the PRE effect, and otherwise longitudinal relaxation times are not averaged out and only depend on the distance from the electron.

First, we can calculate the electronic Wigner-Seitz for radical concentrations of 16 mM. It leads to r_{WS} = 2.9 nm. Calculating numerical values of the pseudopotential for TEKPol in (T_{1e} = 20 μs),[31] and D = 1.10^{-4} μm^{2}s^{-1} ([^{1}H] = 18 M for 1,1,2,2-tetrachloroethane (TCE) at 12.5 kHz MAS), we find ρ_1 = 1 Å. Consequently, $\rho_1 < r_{WS}$, spin diffusion equalizes T_1s over space, and the effective longitudinal relaxation time is constant over space. It also means that the measured T_1 cannot be calculated with equation (1.33) alone, and further investigations are necessary to predict the build-up behaviour taking into account spin diffusion. It also explains why Bloembergen had such good agreements between his relaxation theory and his experimental measurements, since the solid samples that he examined were networks of ^{55}Mn or ^{51}V in which the spin diffusion coefficient is reduced by several orders of magnitude compared to proton, leading to a case where $\rho_1 > r_{WS}$ and where relaxation is diffusion limited.[37]

1.4.3 Quenching barrier

In this section, we show how the PRE effect on transverse relaxation times generates a quenching volume around the electron, and we try to find an estimate of the volume where this quenching occurs.

Equation (1.35) describes the transverse relaxation time due to the contribution of the free electron. Due to strong couplings between the electron and nearby nuclei, these nuclei will see their signal rapidly dephased during signal acquisition. This effect is called **paramagnetic quenching**.

Experimental measurements[66] show that at 18.8 T, 10 % of the sample is quenched at a radical concentration of 10 mM for AMUPol. This leads to a quenching barrier radius $r_q = (0.1)^{1/3}r_{WS}$ = 1.3 nm. At 9.4 T, we also assume 10% quenching.

Analogously as De Gennes' longitudinal pseudopotential, we can define the transverse pseudopotential:

$$\rho_2 = 0.68 \left(\frac{K_2}{D}\right)^{1/4} \tag{1.37}$$

The difference here is that in the transverse plane, nuclear spins dephase so quickly that spin diffusion is almost inexistent. Consequently, $\rho_2 \gg r_{WS}$ and the transverse relaxation is diffusion limited: the dephasing of the spins depends on their distance relative to the electron location, transverse relaxation is not averaged out by spin diffusion, and the presence of a quenching barrier is justified.

For the following of this thesis, we will follow experimental measurements and use r_q = 1.3 nm (10 %) at 8 kHz spinning rate for AMUPol and TEKPol at 18.8 and 9.4 T.[67]

Table 1.1 summarizes the typical radii for a system of a ^{1}H network with [^{1}H] = 11 M at 9.4 T with [AMUPol] = 10 mM.

	Electronic Wigner-Seitz r_{WS}	Pseudo-potential ρ_1	Pseudo-potential ρ_2	Diffusion barrier r_b	Quenching barrier r_q	T_1 barrier r_{T1}
Radius estimation	29 Å	1 Å	/	7 Å	13 Å	12 Å

Table 1.1: Estimation of radii for a system with [^{1}H] = 11 M doped with 12 mM of radical molecules.

In Table 1, we define the T_1 barrier as the distance from the electron at which T_1 is half the one of the diamagnetic bulk $T_{1,dia}$. A representation of equation (1.33) showing the contribution of paramagnetic and diamagnetic relaxation as a function of the distance from the electron for $T_{1,dia}$ = 45 s and $T_{2,dia}$ = 5 ms is shown in Figure 1.11a.
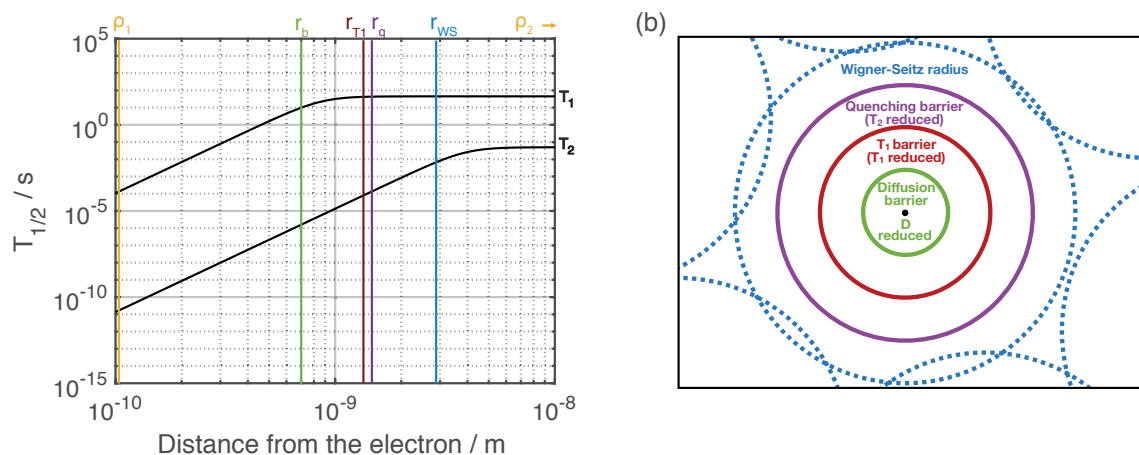
Figure 1.11: (a) Longitudinal and transverse relaxation times in the presence of an electron as a function the distance from this electron. Overlapped are the longitudinal (ρ_1) and transverse (ρ_2) pseudopotentials, the estimated spin diffusion barrier radius r_b, the T_1 barrier r_{T1}, the quenching radius r_q, and the electronic Wigner-Seitz radius r_{WS}. (b) Schematic representation of the different radii around the electron location.

The last radius to be defined is the radius at which nuclear spins are directly polarized by the DNP mechanism in the case of cross-effect r_{CE} for MAS DNP or other mechanism for dDNP r_{DNP}. There is *a priori* no way of measuring such a radius directly, but estimations of its length will be made in chapter 3.

We need to keep in mind that these radii are calculated assuming that radical molecules can be modelled as single points. However, it is a simplifying approximation since binitroxide molecules possess 2 electrons and are about 1.4 nm wide in the case of TEKPol[31] (1.3 nm for AMUPol).[68]

It must also be kept in mind that these radii represent blurred borders. Indeed, spatially dependent parameters such as T_1, T_2, or D don't vary as step functions but are rather continuous functions. The volumes defined here should not be representing perfect spheres but are rather ellipsoids that encode the surface for which the zz-component of the hyperfine tensor is constant. Wenckebach showed that the shape of the diffusion barrier and directly polarized ellipsoids should be as shown in Figure 1.12.[69]
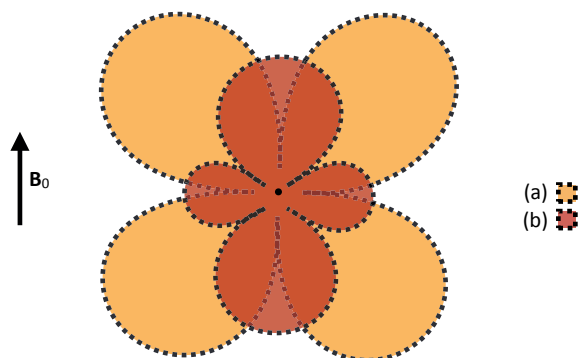
Figure 1.12: Regions around an electron where (a) spins are polarized directly by DNP, and (b) spins are inside the spin diffusion barrier.[69]

In summary, we observe that dipolar couplings can trigger nuclear spin diffusion between identical spins, and that spin diffusion dynamics are modified with the presence of paramagnets. In such systems, several phenomena are occurring at the same time: DNP mechanism(s), PRE effects, and nuclear spin diffusion. In order to have quantitative insights on how these phenomena interact together, numerical simulations will be of great help, as described in the next chapter.

References

(1) Rabi, II; Zacharias, J. R.; Millman, S.; Kusch, P. A new method of measuring nuclear magnetic moment *Phys. Rev.* **1938**, *53*, 318-318.

(2) Bloch, F. NUCLEAR INDUCTION *Phys. Rev.* **1946**, *70*, 460-474.

(3) Purcell, E. M.; Torrey, H. C.; Pound, R. V. RESONANCE ABSORPTION BY NUCLEAR MAGNETIC MOMENTS IN A SOLID *Phys. Rev.* **1946**, *69*, 37-38.

(4) Abragam, A. THE PRINCIPLES OF NUCLEAR MAGNETISM *Current Contents/Physical Chemical & Earth Sciences* **1982**, 18-18.

(5) Morris, G. A.; Freeman, R. ENHANCEMENT OF NUCLEAR MAGNETIC-RESONANCE SIGNALS BY POLARIZATION TRANSFER *Journal of the American Chemical Society* **1979**, *101*, 760-762.

(6) Anderson, W. A.; Freeman, R. INFLUENCE OF A SECOND RADIOFREQUENCY FIELD ON HIGH-RESOLUTION NUCLEAR MAGNETIC RESONANCE SPECTRA *Journal of Chemical Physics* **1962**, *37*, 85-&.

(7) Overhauser, A. W. POLARIZATION OF NUCLEI IN METALS *Phys. Rev.* **1953**, *92*, 411-415.

(8) Hartmann, S. R.; Hahn, E. L. NUCLEAR DOUBLE RESONANCE IN ROTATING FRAME *Phys. Rev.* **1962**, *128*, 2042-&.

(9) Pines, A.; Waugh, J. S.; Gibby, M. G. PROTON-ENHANCED NUCLEAR INDUCTION SPECTROSCOPY - METHOD FOR HIGH-RESOLUTION NMR OF DILUTE SPINS IN SOLIDS *Journal of Chemical Physics* **1972**, *56*, 1776-&.

(10) Natterer, J.; Bargon, J. Parahydrogen induced polarization *Progress in Nuclear Magnetic Resonance Spectroscopy* **1997**, *31*, 293-315.

(11) Hirsch, M. L.; Kalechofsky, N.; Belzer, A.; Rosay, M.; Kempf, J. G. Brute-Force Hyperpolarization for NMR and MRI *Journal of the American Chemical Society* **2015**, *137*, 8428-8434.

(12) Hirsch, M. L.; Smith, B. A.; Mattingly, M.; Goloshevsky, A. G.; Rosay, M.; Kempf, J. G. Transport and imaging of brute-force C-13 hyperpolarization *Journal of Magnetic Resonance* **2015**, *261*, 87-94.

(13) Kastler, A. OPTICAL METHODS OF ATOMIC ORIENTATION AND OF MAGNETIC RESONANCE *Journal of the Optical Society of America* **1957**, *47*, 460-465.

(14) Walker, T. G.; Happer, W. Spin-exchange optical pumping of noble-gas nuclei *Reviews of Modern Physics* **1997**, *69*, 629-642.

(15) Abraham, M.; McCausland, M. A. H.; Robinson, F. N. H. DYNAMIC NUCLEAR POLARIZATION *Physical Review Letters* **1959**, *2*, 449-451.

(16) Abragam, A.; Goldman, M. PRINCIPLES OF DYNAMIC NUCLEAR-POLARIZATION *Reports on Progress in Physics* **1978**, *41*, 395-467.

(17) Carver, T. R.; Slichter, C. P. POLARIZATION OF NUCLEAR SPINS IN METALS *Phys. Rev.* **1953**, *92*, 212-213.

(18) Goldman, M. *Spin temperature and nuclear magnetic resonance in solids*; Clarendon Press, 1970.

(19) Abragam, A.; Goldman, M. *Nuclear magnetism: order and disorder*; Clarendon Press, 1982.

(20) Jeffries, C. D. POLARIZATION OF NUCLEI BY RESONANCE SATURATION IN PARAMAGNETIC CRYSTALS *Phys. Rev.* **1957**, *106*, 164-165.

(21) alternatives, C. à. l. é. a. e. a. é. *Une nouvelle méthode de polarisation dynamique des noyaux atomiques dans les solides: par A. [Anatole] Abragam et W.G. [Warren George] Proctor*; Centre d'études nucléaires, Service de documentation, 1958.

(22) Hu, K. N.; Debelouchina, G. T.; Smith, A. A.; Griffin, R. G. Quantum mechanical theory of dynamic nuclear polarization in solid dielectrics *Journal of Chemical Physics* **2011**, *134*.

(23) Hovav, Y.; Feintuch, A.; Vega, S. Theoretical aspects of dynamic nuclear polarization in the solid state - The cross effect *Journal of Magnetic Resonance* **2012**, *214*, 29-41.

(24) Atsarkin, V. A.; Rodak, M. I. TEMPERATURE OF SPIN-SPIN INTERACTIONS IN ELECTRON-PARAMAGNETIC RESONANCE *Uspekhi Fiz. Nauk* **1972**, *107*, 3-+.

(25) Goertz, S. T. The dynamic nuclear polarization process *Nucl. Instrum. Methods Phys. Res. Sect. A-Accel. Spectrom. Dect. Assoc. Equip.* **2004**, *526*, 28-42.

(26) Andrew, E. R.; Bradbury, A.; Eades, R. G. NUCLEAR MAGNETIC RESONANCE SPECTRA FROM A CRYSTAL ROTATED AT HIGH SPEED *Nature* **1958**, *182*, 1659-1659.

(27) Wind, R. A.; Duijvestijn, M. J.; Vanderlugt, C.; Manenschijn, A.; Vriend, J. APPLICATIONS OF DYNAMIC NUCLEAR-POLARIZATION IN C-13 NMR IN SOLIDS *Progress in Nuclear Magnetic Resonance Spectroscopy* **1985**, *17*, 33-67.

(28) Becerra, L. R.; Gerfen, G. J.; Temkin, R. J.; Singel, D. J.; Griffin, R. G. DYNAMIC NUCLEAR-POLARIZATION WITH A CYCLOTRON-RESONANCE MASER AT 5-T *Physical Review Letters* **1993**, *71*, 3561-3564.

(29) Bouleau, E.; Saint-Bonnet, P.; Mentink-Vigier, F.; Takahashi, H.; Jacquot, J. F.; Bardet, M.; Aussenac, F.; Purea, A.; Engelke, F.; Hediger, S.; Lee, D.; De Paepe, G. Pushing NMR sensitivity limits using dynamic nuclear polarization with closed-loop cryogenic helium sample spinning *Chemical Science* **2015**, *6*, 6806-6812.

(30) Vuichoud, B. Novel Sample Formulations for Pure and Persistent Hyperpolarized Solutions via Dissolution Dynamic Nuclear Polarization *PhD thesis* **2017**.

(31) Zagdoun, A.; Casano, G.; Ouari, O.; Schwarzwalder, M.; Rossini, A. J.; Aussenac, F.; Yulikov, M.; Jeschke, G.; Coperet, C.; Lesage, A.; Tordo, P.; Emsley, L. Large Molecular Weight Nitroxide Biradicals Providing Efficient Dynamic Nuclear Polarization at Temperatures up to 200 K *Journal of the American Chemical Society* **2013**, *135*, 12790-12797.

(32) Ardenkjaer-Larsen, J. H.; Fridlund, B.; Gram, A.; Hansson, G.; Hansson, L.; Lerche, M. H.; Servin, R.; Thaning, M.; Golman, K. Increase in signal-to-noise ratio of > 10,000 times in liquid-state NMR *Proceedings of the National Academy of Sciences of the United States of America* **2003**, *100*, 10158-10163.

(33) Comment, A.; van den Brandt, B.; Uffmann, K.; Kurdzesau, F.; Jannin, S.; Konter, J. A.; Hautle, P.; Wenckebach, W. T. H.; Gruetter, R.; van der Klink, J. J. Design and performance of a DNP prepolarizer coupled to a rodent MRI scanner *Concepts in Magnetic Resonance Part B-Magnetic Resonance Engineering* **2007**, *31B*, 255-269.

(34) Bornet, A.; Milani, J.; Vuichoud, B.; Linde, A. J. P.; Bodenhausen, G.; Jannin, S. Microwave frequency modulation to enhance Dissolution Dynamic Nuclear Polarization *Chemical Physics Letters* **2014**, *602*, 63-67.

(35) Bornet, A.; Melzi, R.; Jannin, S.; Bodenhausen, G. Cross Polarization for Dissolution Dynamic Nuclear Polarization Experiments at Readily Accessible Temperatures 1.2 < T < 4.2 K *Applied Magnetic Resonance* **2012**, *43*, 107-117.

(36) Milani, J.; Vuichoud, B.; Bornet, A.; Mieville, P.; Mottier, R.; Jannin, S.; Bodenhausen, G. A magnetic tunnel to shelter hyperpolarized fluids *Review of Scientific Instruments* **2015**, *86*.

(37) Bloembergen, N. ON THE INTERACTION OF NUCLEAR SPINS IN A CRYSTALLINE LATTICE *Physica* **1949**, *15*, 386-426.

(38) Bloembergen, N.; Morgan, L. O. PROTON RELAXATION TIMES IN PARAMAGNETIC SOLUTIONS EFFECTS OF ELECTRON SPIN RELAXATION *Journal of Chemical Physics* **1961**, *34*, 842-&.

(39) Vuichoud, B.; Bornet, A.; de Nanteuil, F.; Milani, J.; Canet, E.; Ji, X.; Mieville, P.; Weber, E.; Kurzbach, D.; Flamm, A.; Konrat, R.; Gossert, A. D.; Jannin, S.; Bodenhausen, G. Filterable Agents for Hyperpolarization of Water, Metabolites, and Proteins *Chemistry-a European Journal* **2016**, *22*, 14696-14700.

(40) Gajan, D.; Bornet, A.; Vuichoud, B.; Milani, J.; Melzi, R.; van Kalkeren, H. A.; Veyre, L.; Thieuleux, C.; Conley, M. P.; Gruning, W. R.; Schwarzwalder, M.; Lesage, A.; Coperet, C.; Bodenhausen, G.; Emsley, L.; Jannin, S. Hybrid polarizing solids for pure hyperpolarized liquids through dissolution dynamic nuclear

polarization *Proceedings of the National Academy of Sciences of the United States of America* **2014**, *111*, 14693-14697.

(41) Bornet, A.; Ji, X.; Mammoli, D.; Vuichoud, B.; Milani, J.; Bodenhausen, G.; Jannin, S. Long-Lived States of Magnetically Equivalent Spins Populated by Dissolution-DNP and Revealed by Enzymatic Reactions *Chemistry-a European Journal* **2014**, *20*, 17113-17118.

(42) Ji, X.; Bornet, A.; Vuichoud, B.; Milani, J.; Gajan, D.; Rossini, A. J.; Emsley, L.; Bodenhausen, G.; Jannin, S. Transportable hyperpolarized metabolites *Nature Communications* **2017**, *8*.

(43) Capozzi, A.; Cheng, T.; Boero, G.; Roussel, C.; Comment, A. Thermal annihilation of photo-induced radicals following dynamic nuclear polarization to produce transportable frozen hyperpolarized C-13-substrates *Nature Communications* **2017**, *8*.

(44) Dumez, J. N.; Vuichoud, B.; Mammoli, D.; Bornet, A.; Pinon, A. C.; Stevanato, G.; Meier, B.; Bodenhausen, G.; Jannin, S.; Levitt, M. H. Dynamic Nuclear Polarization of Long-Lived Nuclear Spin States in Methyl Groups *Journal of Physical Chemistry Letters* **2017**, *8*, 3549-3555.

(45) Albers, M. J.; Bok, R.; Chen, A. P.; Cunningham, C. H.; Zierhut, M. L.; Zhang, V. Y.; Kohler, S. J.; Tropp, J.; Hurd, R. E.; Yen, Y. F.; Nelson, S. J.; Vigneron, D. B.; Kurhanewicz, J. Hyperpolarized C-13 Lactate, Pyruvate, and Alanine: Noninvasive Biomarkers for Prostate Cancer Detection and Grading *Cancer Research* **2008**, *68*, 8607-8615.

(46) Gallagher, F. A.; Kettunen, M. I.; Day, S. E.; Hu, D. E.; Ardenkjaer-Larsen, J. H.; in't Zandt, R.; Jensen, P. R.; Karlsson, M.; Golman, K.; Lerche, M. H.; Brindle, K. M. Magnetic resonance imaging of pH in vivo using hyperpolarized (13)C-labelled bicarbonate *Nature* **2008**, *453*, 940-U973.

(47) Slichter, C. P. *Principles of Magnetic Resonance*; Springer Berlin Heidelberg, 1996.

(48) Levitt, M. H. *Spin Dynamics: Basics of Nuclear Magnetic Resonance*; Wiley, 2001.

(49) Keeler, J. *Understanding NMR Spectroscopy*; Wiley, 2011.

(50) Maricq, M. M.; Waugh, J. S. NMR IN ROTATING SOLIDS *Journal of Chemical Physics* **1979**, *70*, 3300-3316.

(51) Girifalco, L. A. *Statistical Mechanics of Solids*; Oxford University Press, 2000.

(52) Blumberg, W. E. NUCLEAR SPIN-LATTICE RELAXATION CAUSED BY PARAMAGNETIC IMPURITIES *Phys. Rev.* **1960**, *119*, 79-84.

(53) Khutsishvili, G. R. SPIN DIFFUSION *Soviet Physics Uspekhi-Ussr* **1966**, *8*, 743-+.

(54) Suter, D.; Ernst, R. R. SPIN DIFFUSION IN RESOLVED SOLID-STATE NMR-SPECTRA *Physical Review B* **1985**, *32*, 5608-5627.

(55) Dolinsek, J.; Cereghetti, P. M.; Kind, R. Phonon-assisted spin diffusion in solids *Journal of Magnetic Resonance* **2000**, *146*, 335-344.

(56) Robyr, P.; Meier, B. H.; Ernst, R. R. RADIO-FREQUENCY-DRIVEN NUCLEAR-SPIN DIFFUSION IN SOLIDS *Chemical Physics Letters* **1989**, *162*, 417-423.

(57) Goldman, M. IMPURITY-CONTROLLED NUCLEAR RELAXATION *Phys. Rev.* **1965**, *138*, 1675-&.

(58) Schmugge, T. J.; Jeffries, C. D. HIGH DYNAMIC POLARIZATION OF PROTONS *Phys. Rev.* **1965**, *138*, 1785-&.

(59) Lowe, I. J.; Tse, D. NUCLEAR SPIN-LATTICE RELAXATION VIA PARAMAGNETIC CENTERS *Phys. Rev.* **1968**, *166*, 279-&.

(60) Ramakrishna, J.; Robinson, F. N. A TRANSIENT EFFECT IN DYNAMIC NUCLEAR POLARIZATION *Proc. Phys. Soc. Lond.* **1966**, *87*, 945-+.

(61) Wolfe, J. P. DIRECT OBSERVATION OF A NUCLEAR SPIN DIFFUSION BARRIER *Physical Review Letters* **1973**, *31*, 907-910.

(62) Ramakrishna, J. A NOTE ON ANISOTROPY OF SPIN DIFFUSION BARRIER *Proc. Phys. Soc. Lond.* **1966**, *89*, 473-+.

(63) Solomon, I. RELAXATION PROCESSES IN A SYSTEM OF 2 SPINS *Phys. Rev.* **1955**, *99*, 559-565.

(64) Bertini, I.; Luchinat, C.; Parigi, G.; Ravera, E. *NMR of Paramagnetic Molecules: Applications to Metallobiomolecules and Models*; Elsevier Science, 2016.

(65) Degennes, P. G. SUR LA RELAXATION NUCLEAIRE DANS LES CRISTAUX IONIQUES *Journal of Physics and Chemistry of Solids* **1958**, *7*, 345-350.

(66) Chaudhari, S. R.; Berruyer, P.; Gajan, D.; Reiter, C.; Engelke, F.; Silverio, D. L.; Coperet, C.; Lelli, M.; Lesage, A.; Emsley, L. Dynamic nuclear polarization at 40 kHz magic angle spinning *Physical Chemistry Chemical Physics* **2016**, *18*, 10616-10622.

(67) Kubicki, D. J.; Casano, G.; Schwarzwalder, M.; Abel, S.; Sauvee, C.; Ganesan, K.; Yulikov, M.; Rossini, A. J.; Jeschke, G.; Coperet, C.; Lesage, A.; Tordo, P.; Ouari, O.; Emsley, L. Rational design of dinitroxide biradicals for efficient cross-effect dynamic nuclear polarization *Chemical Science* **2016**, *7*, 550-558.

(68) Sauvee, C.; Rosay, M.; Casano, G.; Aussenac, F.; Weber, R. T.; Ouari, O.; Tordo, P. Highly Efficient, Water-Soluble Polarizing Agents for Dynamic Nuclear Polarization at High Frequency *Angewandte Chemie-International Edition* **2013**, *52*, 10858-10861.

(69) Wenckebach, W. T. *Essentials of Dynamic Nuclear Polarization*; Spindrift Publications, 2016.

Chapter 2:
Numerical model
of polarization dynamics

The following chapter is adapted with permission from the publication:

Pinon, A. C.; Schlagnitweit, J.; Berruyer, P.; Rossini, A. J.; Lelli, M.; Socie, E.; Tang, M. X.; Pham, T.; Lesage, A.; Schantz, S.; Emsley, L. *Measuring Nano- to Microstructures from Relayed Dynamic Nuclear Polarization NMR J. Phys. Chem. C* **2017**, *121*, 15993-16005.

2.1 Description of the model

2.1.1 Context and implementation

Modern materials such as polymers or pharmaceuticals, as well as porous materials, are usually well-designed nano- or microstructured systems. The physical properties of these materials are strongly related to domain sizes. Therefore, methods to determine architectures on these nano- to micrometer length scales are necessary for the development of next-generation materials.

Depending on the nature of the sample, domain sizes may be measurable by laser diffraction, scattering methods, or by electron microscopy methods.[1-3] However, in complex multicomponent mixtures, these methods become much more difficult to apply since they often cannot resolve more than two components. NMR would be a method of choice in these cases. Indeed, based on chemical shift differences or relaxation properties of different compounds, NMR often allows clear distinction among several components. Consequently, the study of *in situ* domain sizes becomes feasible with NMR methods.[4,5]

Proton spin diffusion experiments are the most widely used methods for domain size measurement.[6,7] In these experiments an initial spatially heterogeneous non-equilibrium distribution of magnetization is created, and the return to equilibrium driven by spin diffusion is monitored.[8] In order to create the non-equilibrium distribution by selecting proton magnetization from particular domains, different procedures have been proposed including filters based on dipolar couplings,[7,9,10] differences in relaxation properties,[8] or proton or carbon chemical shift differences.[11-15] These methods work well in two-component systems where the components exhibit significant differences in the properties chosen for selection. However, for more complex multiple component systems these methods are usually not feasible.

It has recently been shown that domain sizes can be determined in complex systems using dynamic nuclear polarization (DNP) where the non-equilibrium distribution of magnetization is obtained by locally enhancing polarization.[16-19] It has also been shown that the selection process can be replaced by selective doping of one of the domains of the diamagnetic system with paramagnetic species, and using paramagnetic relaxation enhancement to estimate the domain sizes.[20]

In these approaches, the initial out of equilibrium state is achieved by selective doping followed by either comparison with spin diffusion dynamics in an undoped sample, or comparison to a state in which the doped region is hyperpolarized. The curves obtained through comparison of the two initial states for different recovery times in experiments can then be interpreted using numerical solutions of the diffusion equations.

The DNP method has previously been used to determine domain sizes for an active pharmaceutical ingredient (API), cetirizine dihydrochloride, in a drug formulation.[19] Griffin and coworkers previously studied the dynamics of hyperpolarization,[21] and the diffusion of polarization through peptide nanocrystals in a frozen solution.[16]

In this chapter using numerical simulations we model the flow of magnetization in homogeneous and heterogeneous DNP systems in order to explain experimental data and to predict the outcome of future experiments. **We find explicit relationships between steady state enhancement, build-up time, and domain size.**

We consider here systems suitable for DNP: they are doped with radical molecules. We only consider spin diffusion between proton spins, and we only study the z-component of the magnetization. Finally, we consider here systems that fulfil the high temperature approximation, i.e. where the ratio of spins up and down is small enough not to inhibit flip-flop transitions.

The basic principle behind the idea of doping the sample is that it will create two types of proton spins:

1. proton spins directly coupled to the electron spin of the radical molecule, referred here as the **source spins**,
2. proton spins not directly coupled to the electron spin of the radical molecule, referred here as the **target spins**

The first effect is that the presence of free electrons creates a PRE effect on the directly coupled source spins, that leads to a fast polarization build-up. Then, the polarization flows through proton spin diffusion into the target spins due to spatial heterogeneity of polarization. Finally, proton spin diffusion is either helped or inhibited by the intrinsic relaxation time T_1 of the target spins depending on the microwave irradiation, as detailed later. Finally, the proton polarization can then be then transferred to the desired heteronuclei via cross polarization.

It is now important to distinguish two cases. In the first case of **homogeneous systems** (homogeneous frozen radical solutions) where the length scale to be studied is on the order of angstroms up to few nanometres, the spatial variation of parameters (T_1, T_2, D) is governed by electron-proton couplings. In the second case of **hetergeneous systems** (micro particles impregnated with a radical solution) where the length scale to be studied is on the order of micrometres, the spatial variation of parameters is rather defined by the interface between the macroscopic source (the radical solution) and target domain (the micro particle). For homogeneous system, we consider that the spatial variation of parameters follows functions that change as r^{-6}, while for heterogeneous systems, fore sake of convenience, we choose to use a hyperbolic secant function that are more suited to describe such borders. For heterogeneous systems, the shape of the function has little or no effect on the observables because the width of the objects considered here is on the order of micrometers.

In order to obtain a quantitative insight into the polarization dynamics of such systems, we discuss in this chapter the development of a numerical approach that allows the visualisation of the spatial propagation of nuclear polarisation during the DNP process.

Since the fifties, several models purely based on quantum mechanics have been proposed for describing the behaviour of spin diffusion.[22-27] Spin diffusion can also be simulated using *ab-initio* approaches on a quantum mechanical basis.[28-34] However, even though exact solution are expected form such treatments, these methods need significant mathematical treatment and calculation power. When studied systems are on the order of µm, the number of nuclei to consider is on the order of 10^6 spins. Such enormous number of spins cannot be treated with the previously mentioned methods.

We follow here a thermodynamic approach that describes ensembles of spins as domains, based on the work of Bloembergen[27] who was one of the first to use the theory of heat conduction to describe polarization dynamics. We use a finite element method in order simulate the propagation of magnetic energy and visualize the polarization as a function of space and time, as described in the next section.

2.1.2 Parameters definition

Vocabulary: We use the following terms:

- r or x refers to the position in space
- t refers to the time
- P refers to the polarization
- M refers to the magnetization
- D refers to the spin diffusion coefficient
- T_1 refers to the intrinsic longitudinal relaxation time of the target
- T_B refers to the effective build-up time of the source in presence of spin diffusion
- µwave(s) refers to the word: microwave(s)
- v_r refers to the MAS rate
- index "s" and "t" refer to "source" and "target" respectively

The polarization can be described using the **Spin Temperature**.[35] Using equation (1.10), one can define the spin temperature as:

$$T_S = \frac{\gamma \hbar B_0}{2k_B \tanh^{-1}(P)} \tag{2.1}$$

When the system is not hyperpolarized, the equilibrium spin temperature corresponds to the lattice temperature. For a hyperpolarized sample, <u>the spin temperature corresponds to the temperature it would be necessary to reach to achieve the same hyperpolarization</u>. In some cases, describing the system in terms of spin temperature can be convenient: cold regions correspond to high polarization, and hot regions to low polarization. It becomes even more convenient when two different spins exchange magnetization (e.g. protons and electrons) since different gyromagnetic ratios are involved. But here, since we only study homonuclear spin diffusion, we choose to describe the system in terms of polarization rather than in terms of spin temperature.

The polarization dynamics of a sample of proton spins doped with paramagnets is described analogously as a heat transfer, where here the quantity to be transferred is the **magnetic energy**. During microwave irradiation (µwaves on) or simply with MAS (µwaves off), the electronic magnetic energy is propagated from the electron reservoir to the source protons reservoir via the DNP mechanisms, and then relayed to the target protons reservoir via spin diffusion. Once hyperpolarization has reached target protons, they are subject to longitudinal relaxation. The overall process is schematized in Figure 2.1:
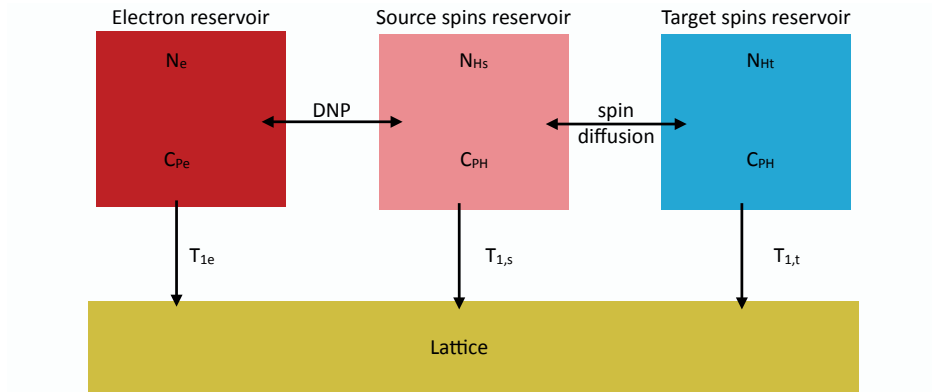
Figure 2.1: Scheme of energy reservoirs in a DNP system. N_e is the number of electrons in the electron reservoir, $N_{Hs/Ht}$ the number of ^1H spins in the source/target reservoir, $C_{Pe/H}$ the spin capacity of electron/proton spins, and $T_{1,e/s/t}$ the intrinsic relaxation time of the electron/source protons/target protons reservoir.

In this thesis, numerical simulations are only focusing on the source/target spin reservoirs (right hand side of Figure 2.1), connected via spin diffusion. Indeed, our model doesn't simulate the efficiency of the DNP mechanism itself. It only simulates the propagation of polarization from the hyperpolarized source spins to the target spins. The source will always be represented in pink, whereas the target will always be represented in blue.

2.2 Diffusion of magnetic energy

In these sections, we introduce the diffusion equation that governs polarization dynamics in both homogeneous and heterogeneous systems. We define all the parameters that play a role in polarization dynamics, and how each of them varies as a function of space, time, MAS rate, proton or radical concentration. We introduce the concepts of polarizing and relaxing powers, as well as the characteristic diffusion length, that will be used in chapters 3 and 4. Finally, we examine typical numerical results in order to find a relationship between the steady state enhancement, the build-up/relaxation time, the spin diffusion coefficient, and domain sizes.

2.2.1 Diffusion equation

One of the most common experiments that we model in this thesis are saturation recovery experiments. A representation of the saturation recovery pulse sequence can be found in chapter 3. In such an experiment, all ^{1}H spins are all first saturated, and then the return to equilibrium is monitored. Processes that dominate polarization dynamics in a saturation recovery experiment are schematized in Figure 2.2 for the case of a source + target system:
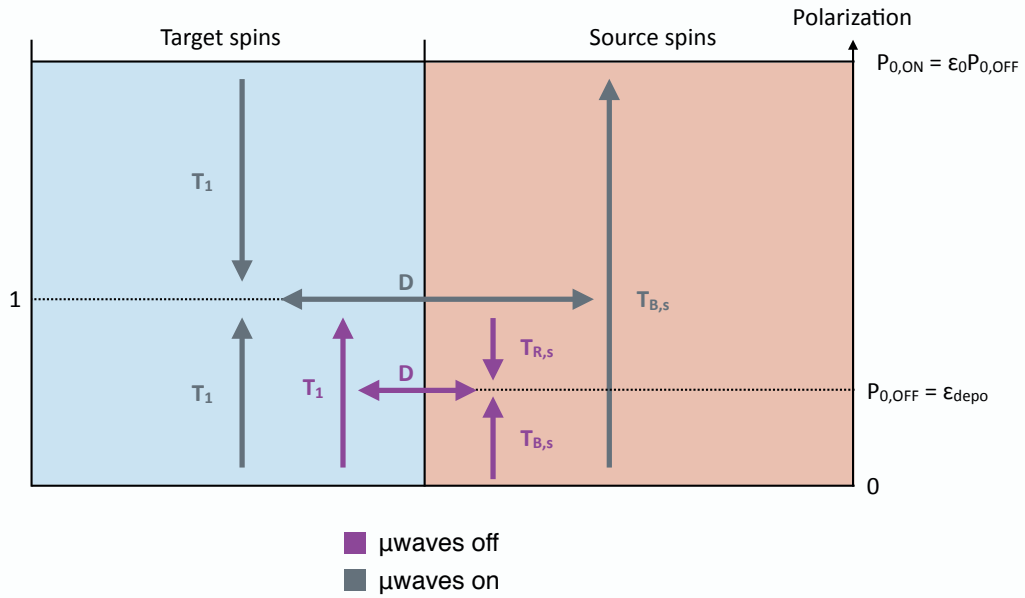
Figure 2.2: Scheme of processes happening in a source + target system during a saturation recovery experiment. The polarizations are quantified in units of Boltzmann polarization for a fixed temperature. Here, the source represents a region doped with paramagnetic species. $T_{R,s}$ represents the effective relaxation time of the source spins.

The polarization dynamics during a saturation recovery experiment can be described as a classical heat transfer process that follows Fick's second law:[36]

$$C_p \cdot C_{eff}(x) \cdot \frac{\partial P(x,t)}{\partial t} = \nabla\big(D(x) \cdot C_p \cdot C_{eff}(x) \cdot \nabla P(x,t)\big) - C_p \cdot C_{eff}(x) \cdot \frac{P(x,t) - P_0(x,t)}{T_{1/B}(x)} \qquad (2.3)$$

where x is the position vector in space in μm, t the time in seconds, P the instantaneous polarization relative to the equilibrium polarization at the given (and fixed) temperature, in units of Boltzmann polarization, P_0 the local equilibrium polarization in units of Boltzmann polarization, D the diffusion coefficient in $\mu m^2 s^{-1}$, $T_{1/B}$ the relaxation/build-up time constants in seconds, C_{eff} the concentration of participating spins in mol.L^{-1}, C_p the molar capacity in J.mol^{-1}, and ∇ the Nabla operator of the system that contains first derivatives with respect to spatial coordinates.

The initial and boundary conditions of equation (2.3) are:

$$P(x, 0) = 0 \tag{2.4}$$

and

$$\frac{\partial P}{\partial x}(x_{lim}, t) = 0 \tag{2.5}$$

where x_{lim} corresponds to the position at the extremities of the system. Equation (2.4) corresponds to no initial polarization, since spins are usually all saturated at the beginning of the experiment. Equation (2.5) corresponds to no flux at the edges of the system. It means that one side of the system represents to the center of the target object (left limit on Figure 2.2), and the other side of the system corresponds to a periodic system (each unit "feels" the presence of its neighbour, right limit on Figure 2.2).

Here, the concentration of spins that participate to the process is lower than the total spin concentration since in the source some spins are located inside the spin diffusion barrier. We have:

$$C_{eff}(x) = C(x) \cdot \left[1 - \left(\frac{r_b}{r_{WS}} \right)^3 \right] \tag{2.6}$$

where r_b is the spin diffusion barrier radius and r_{WS} the Wigner-Seitz radius as defined in chapter 1. Numerical values for a radical concentration of 16 mM and r_b = 0.7 nm lead to $C_{eff}(x)$ = 0.99 C(x). In the following, we will consider that both concentrations are equal, and use C instead of C_{eff}. In equation (2.3), the product:

$$M(x, t) = C_p \cdot C(x) \cdot P(x, t) \tag{2.7}$$

is defined as the **spin magnetization** per unit of volume. Equation (2.3) can now be simplified:

$$\frac{\partial M(x, t)}{\partial t} = \nabla(D(x)\nabla M(x, t)) - \frac{M(x, t) - M_0(x, t)}{T_{1/B}(x)} \tag{2.8}$$

Equation (2.8) does not have general analytical solution. Under few approximations, it is possible to find some analytical solutions for the steady state regime, as described at the end of this chapter. But for time-dependent solutions, we resort to numerical solutions.

The spin diffusion coefficient D is taken to be a function of the spinning frequency v_r as:

$$D(v) = \frac{D_0}{1 + k \cdot v_r} \tag{2.9}$$

where D_0 corresponds to a fictive ^1H spin diffusion coefficient in a static sample ($D_0 = 1.5 \; 10^{-4} \; \mu m^2 s^{-1}$) at a proton concentration of C = 70 M and k = 0.6 ms.[37,38] For static samples, we simply take the experimentally measured spin diffusion coefficient at 6.7 T and 1.2 K, as detailed in chapter 4.

The local equilibrium polarization corresponds to the polarization that each unit of volume would reach if no spin diffusion was occurring with ($P_{0,ON}$) or without microwave irradiation ($P_{0,OFF}$). P and P_0 are thus dimensionless quantities. The local equilibrium polarization in the target is $P_{0,OFF} = 1$ with and without microwave irradiation. Indeed, the large majority of target spins are not directly coupled to the electron spins located in the source, which implies that their equilibrium polarization is the Boltzmann polarization. This assumption can however be not valid in the case where a significant amount of radical molecules is in close proximity to the border between source and target, and directly transfers its polarization to the nearby target spins at the surface of the target. These so called **surface effects**[39] will be studied in chapter 4.

In the source without microwave irradiation, depolarization may occur in the case of a nitroxide radical under MAS at a spinning rate (v_r), and the local equilibrium polarization $P_{0,OFF}$ is lower than the Boltzmann polarization:

$$P_{0,OFF}(v_r) = \varepsilon_{depo}(v_r) \tag{2.10}$$

where ε_{depo} is an experimentally measured parameter:

$$\varepsilon_{depo}(v_r) = \frac{S_{0,OFF}(v_r > 0)}{S_{0,OFF}(v_r = 0)} \tag{2.11}$$

where $S_{0,OFF}(v_r > 0)$ and $S_{0,OFF}(v_r = 0)$ are the source signals for spinning and static samples, respectively. In the following for AMUPol radicals, we will take $\varepsilon_{depo} = 0.9$ at 18.8 T and 8 kHz MAS, and $\varepsilon_{depo} = 0.5$ at 9.4 T and 8 kHz MAS in line with values found in the literature.[40,41] For TEKPol, we take $\varepsilon_{depo} = 0.9$ at 18.8 T and 9.4 T. We take for carbon based radicals $\varepsilon_{depo} = 1$ in line with values found in the literature.[38,41]

In the presence of microwaves, the local equilibrium polarization within the source is greatly enhanced such that:

$$P_{0,ON} = \varepsilon_0 P_{0,OFF} \tag{2.12}$$

where ε_0 is the enhancement of the source spins.

Once all parameters are all defined, equation (2.8) can be solved numerically twice: for µwaves on and off cases, in order to obtain the polarization as a function of space and time. To calculate the signal, the polarization per unit of volume is integrated over the desired region V as:

$$S_{ON/OFF}(t) = \int_V C(x) \cdot P_{ON/OFF}(x,t) \cdot \theta(x) \cdot |J(x)| \, dx \tag{2.15}$$

42

where $P_{ON/OFF}$ corresponds to the polarization as a numerical solution of equation (2.8), $S_{ON/OFF}$ the signal with/without microwave irradiation respectively, $|J(x)|$ refers to the Jacobian determinant: $|J(x)| = 1$ for linear symmetry, $|J(x)| = 2\pi x$ for cylindrical symmetry and $|J(x)| = 4\pi x^2$ for spherical symmetry, and where θ is the contribution factor defined as:

$$\theta(x) = 1 - \left(\frac{r_q}{r_{WS}}\right)^3$$

(2.16)

where r_q is the quenching radius as defined in chapter 1. We will take $\theta = 0.9$ in line with the values found in the literature.[40] For enhancement calculations for which the quenching factor is the same with or without microwaves, the value of θ doesn't change numerical result. Before looking at typical numerical results, it is important to define the polarizing and relaxing powers, as well as the characteristic diffusion length.

2.2.2 Polarizing and relaxing powers

It is time to define one of the most important concepts of this chapter, the **polarizing power** and the **relaxing power**. The polarizing power corresponds to the amount of magnetic energy that a reservoir of spins can provide per unit of time. Analogously, the relaxing power corresponds to the amount of magnetic energy that a reservoir of spins can relax per unit of time. **These powers define how well the source spin can polarize the target spins, and how well the target spins can relax this polarization**. They are expressed in watts per unit of volume and are defined as:

$$W_P = C_p \frac{C_s}{T_B} \qquad (2.13)$$

with W_P being the source polarizing power, and

$$W_R = C_p \frac{C_t}{T_1} \qquad (2.14)$$

with W_R being the target relaxing power, where $C_{s/t}$ are the spins concentration in the source/target, and where C_p is the spin capacity as described in chapter 1.

These polarizing and relaxing powers are key numbers that are characteristic of the dynamics of the system. The source wants to be hyperpolarized, whereas the target wants to stay at the Boltzmann polarization. Consequently, these powers will be fighting each other, and the final polarization is determining by which of these powers is the strongest.

The communication between the source and the target is established via spin diffusion. It is then interesting to see how W_P, W_R and D interact together. We can distinguish the following cases:

- $W_P \ll W_R$: the source polarizing power is much smaller than the target relaxing power: the target is not hyperpolarized (Figure 2.3a, yellow solid lines)
- $W_P \gg W_R$: the polarizing power of the source is much bigger than the relaxing power of the target: the hyperpolarization is efficiently diffused from the source to the target. The target polarization will be a function of D_t, T_1 and the target size (L_t) (Figure 2.3a, blue solid lines)
- $W_P = W_R$: the source will partially polarize the target but will be partially depleted at the same time (Figure 2.3a, red solid lines)

Each case is represented in Figure 2.3 where the powers are implicitly varied by changing either the spin concentrations $C_{s/t}$, or the time constants $T_{B/1}$ in the source/target respectively. We see for the example of a µwaves on experiment (Figure 2.3a) that when the spin concentration is much higher in the source than in the target or when the source build-up time is much smaller than the target relaxation time (blue solid line), the target steady state polarization is higher (blue solid line) than when concentrations or time constant are equal (red lines), because the source polarizing power is increased.
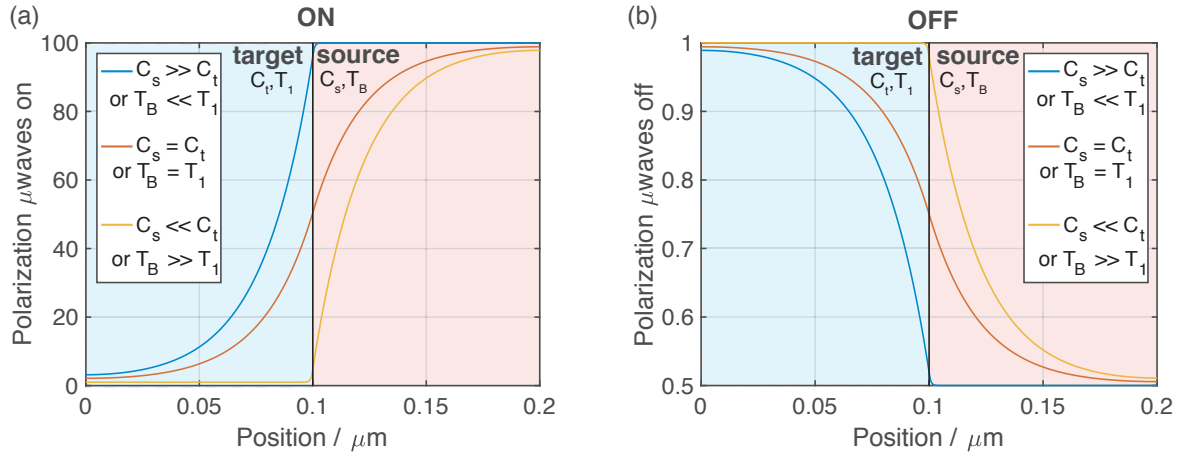
Figure 2.3: Simulated steady state polarizations of a source (pink) + target (blue) system as a function of the polarizing/relaxing powers that are either influenced by the spin concentration C_s/C_t, or by the time constant T_B/T_1. The parameters used in numerical simulations are shown in the following table.

parameter	L_s	L_t	T_B	T_1	C_s	C_t	D_s	D_t	ε_0	ε_{depo}	v_r
value	100	100	1 or 0.001	1 or 0.001	70 or 7000	70 or 7000	varies	varies	200	0.5	12.5
unit	nm	nm	s	s	mol.L^{-1}	mol.L^{-1}	µm^{2}s^{-1}	µm^{2}s^{-1}			kHz

A similar effect is observed for the µwaves off experiment (Figure 2.3b) where the source is depolarized. When the source (de)polarizing power is higher than the target relaxing power (blue solid line) the target is partially depolarized, whereas when the source (de)polarizing power is smaller than the target relaxing power (yellow solid line), the target is not depolarized.

Consequently in a saturation recovery experiment with microwave irradiation, a high source polarizing power increases the steady state polarization in the target.

45

2.2.3 Characteristic diffusion length

Let us consider the case of a very powerful source: the source polarizing power is much bigger than the target relaxing power: **W_P >> W_R:**

In such cases, it is convenient to define the **characteristic diffusion length** in the target ρ_t as:

$$\rho_t = \sqrt{D_t T_1} \tag{2.17}$$

The characteristic diffusion length in the target is defined as the distance from the source at which the polarization is about 36% of the source polarization: $P_t(\rho_t)$ = 0.36 P_s. Details for the mathematical definition of the characteristic diffusion length are given in the section 2.3.2. By comparing the characteristic diffusion length and the size of the target L_t, we can distinguish several cases.

- ρ_t >> L_t: the target is smaller than the diffusion length: the target is hyperpolarized up to $P_{0,ON}$ = ε_0. This corresponds to the case of a bulk radical solution where only a few nanometres of protons are polarized between each radical molecule, as detailed in chapter 3.
- ρ_t << L_t: the target is much bigger than the diffusion length: the target is not hyperpolarized, and target spins build-up following a monoexponential with a T_1 time constant.
- $\rho_t \approx L_t$: the target is hyperpolarized to a polarization value between P = ε_0 and Boltzmann (P=1), with a time constant varying between T_B and T_1. This is the most interesting case for us, since it corresponds to cases where distances can be efficiently measured.

Going back to Figure 2.3, one can obtain a numerical value of the characteristic diffusion length for D_t = 5 10^{-4} $\mu m^2 s^{-1}$ and T_1 = 1 s, leading to ρ_t = 22.3 nm. Since here L_t = 100 nm, it means that the target length is on the order of the spin diffusion length. However in the case of a frozen radical solution where the distance between the electrons is on the order of the Wigner-Seitz radius (2.9 nm for 16 mM), the diffusion length is much bigger than the Wigner-Seitz radius, leading to $P_{0,ON}$ = ε_0, to quasi instantaneous spin diffusion, and to a homogeneous distribution of polarization between radical molecules.

2.3 Typical numerical results

In this section, we show typical results of numerical simulations in order to show the reader how the source build-up time T_B and the target size L_t are influencing the target enhancement ε_t. Finally, by examining the diffusion equation (2.8) at steady state, we find a direct relationship between the steady state enhancements, the build-up/relaxation times, and the spin diffusion coefficient.

For source + target systems, typical polarization and signal build-up curves are shown in Figure 2.4 in the case of $W_P = 10^3 \, W_R$.
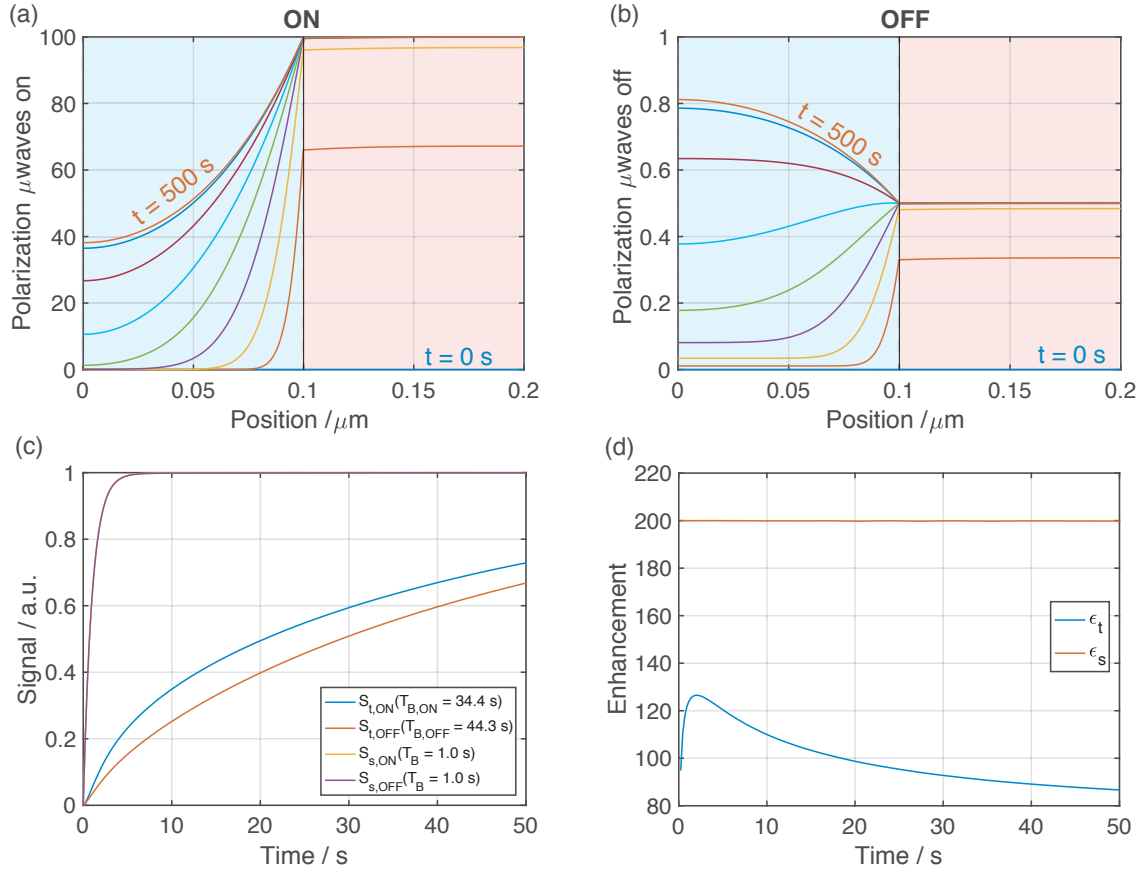

Figure 2.4: Simulated polarization in a source (pink) + target (blue) system as a function of the position, for exponential time steps with (a) and without (b) microwave irradiation. (c) Simulated normalized signal build-up for the source ($S_{s,ON/OFF}$) and target ($S_{t,ON/OFF}$). The source signals with and without microwaves are overlapped. (d) Simulated signal enhancements as a function of time for the source (ε_s) and target (ε_t). The parameters are shown in the following table.

parameter	L_s	L_t	T_B	T_1	C_s	C_t	D_s	D_t	ε_0	ε_{depo}	v_r
value	100	100	1	100	110	10	$8.8 \, 10^{-4}$	$3.7 \, 10^{-5}$	200	0.5	12.5
unit	nm	nm	s	s	mol.L^{-1}	mol.L^{-1}	µm^{2}s^{-1}	µm^{2}s^{-1}			kHz

In Figure 2.4a-b, we see that the polarization starts at P = 0 everywhere (blue line), and that the build-up is faster in the source than in the target. We see in Figure 2.4a-b that the source polarization is homogeneously dispersed, since the source polarizing power is much bigger than the target relaxing power. We also notice that the target polarization is not homogeneous: spin diffusion brings

hyperpolarization with microwaves (or depolarization without microwaves) from the source, whereas relaxation always drags the target polarization towards equilibrium (i.e. towards Boltzmann where P = 1).

Moreover, we notice in Figure 2.4c that the target signal build-ups are accelerated in the presence of microwaves. Indeed, T_1 = 100 s whereas $T_{B,ON}$ = 34.4 s and $T_{B,OFF}$ = 44.3 s. This is due to the presence of spin diffusion that accelerates both build-ups. We also notice that both the source and target build-up times are smaller with than without microwave irradiation. This is due to the fact that the polarization gradient between the source and the target is much bigger in the µwaves on case than in the µwaves off case, leading to more spin diffusion and a faster build-up. **Having a signal build-up $T_{B,ON}$ different from $T_{B,OFF}$ is a signature of polarization heterogeneity**. An important consequence of this observation is that, because proportionally more spins are closer to the source in smaller objects, we predict shorter build-up times for smaller targets. A final observation is that the source signal build-up is identical with or without microwaves. This is because no polarization heterogeneity is present in neither of the µwaves on nor off cases.

For a source + target system as presented above during a saturation recovery experiment, the target signal follows a stretched exponential build-up:

$$S_{ON/OFF}(t) = S_0 \left[1 - e^{-\left(\frac{t}{T_{B,ON/OFF}} \right)^{\beta}} \right]$$
(2.18)

where $T_{B,ON/OFF}$ is the effective build-up time of the target with or without microwave irradiation respectively, β the stretch parameter, and S_0 the steady state value of the signal. The stretch parameter is indicative of the range of T_1's probed. The smaller the T_1's range, the closer β gets to 1. The enhancement as a function of time can then be calculated:

$$\varepsilon(t) = \frac{S_{ON}(t)}{S_{OFF}(t)}$$
(2.19)

Figure 2.4d shows the enhancement as a function time. We notice that **the target enhancement varies significantly with time, and this is another key signature of heterogeneous polarization**. Indeed, if the sample polarization is homogeneous, spin diffusion doesn't cause any change in local polarization, and the enhancement is constant as a function of the polarization time, as it is the case for the source enhancement shown in Figure 2.4d. Finally we notice that target spins closer to the border are more polarized than the ones further from the surface. **We then predict higher enhancements for smaller targets**.

In summary, we predict faster build-ups and bigger enhancement for smaller targets.

The late stage decay of the enhancement as a function of time can be explained physically as follows. With time, the target polarization builds-up to 1 in the µwaves off case (without considering depolarization), whereas it is far from reaching ε_0 in the µwaves on case, because of longitudinal relaxation T_1. Thus, with time, the target polarization increases relatively more in the µwaves off than in the µwaves on case. The early behaviour of the enhancement is less trivial to explain. First, we state that the early stage behaviour of the enhancement corresponds to a hyperpolarization located at the border between the source and the target (no significant spin diffusion had time to occur yet). **Let us now examine the influence of the source build-up time on the enhancements' early behaviour.**

2.3.1 Influence of the source build-up time

Figure 2.5a shows the enhancement at 2 s as a function of time for different source build-up times.
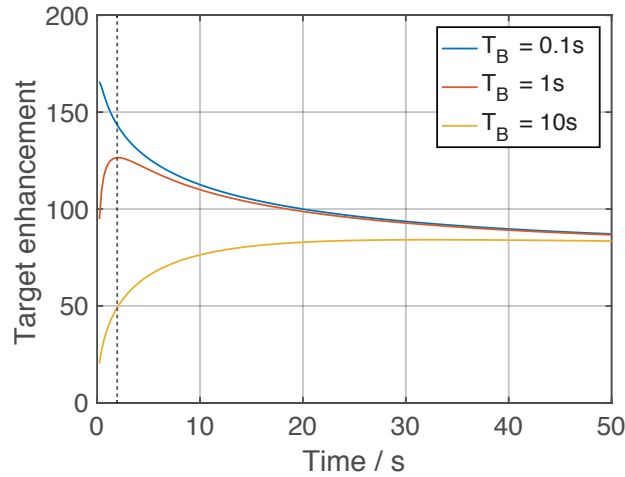

Figure 2.5: Simulated target enhancements as a function of time, for different values of T_B. Parameters are shown in the following table.

parameter	L_s	L_t	T_B	T_1	C_s	C_t	D_s	D_t	ε_0	ε_{depo}	v_r
value	100	100	varies	100	110	10	$8.8\ 10^{-4}$	$3.7\ 10^{-5}$	200	0.5	12.5
unit	nm	nm	s	s	$mol.L^{-1}$	$mol.L^{-1}$	$\mu m^2 s^{-1}$	$\mu m^2 s^{-1}$			kHz

We notice on Figure 2.5 that the early behaviour of the enhancement is largely influenced by T_B. We also notice that to the extent that the source polarizing power remains much bigger than the target relaxing power, **the steady state enhancement doesn't depend on $T_{B,s}$**. The early behaviour is the signature of surface effects: if some radical molecules are adsorbed/aggregated at the surface of the target, the surface radical concentration becomes higher than in the bulk of the radical solution, and the effective build-up at the surface of the target will be much faster than in the bulk of the radical solution. We will study these surface effects in chapter 4.

2.3.2 Influence of the target size

As mentioned earlier, we predict bigger enhancement and faster build-ups for smaller targets. Figure 2.6 shows simulations of the normalized target signal build-up curves and target enhancements for different target sizes.
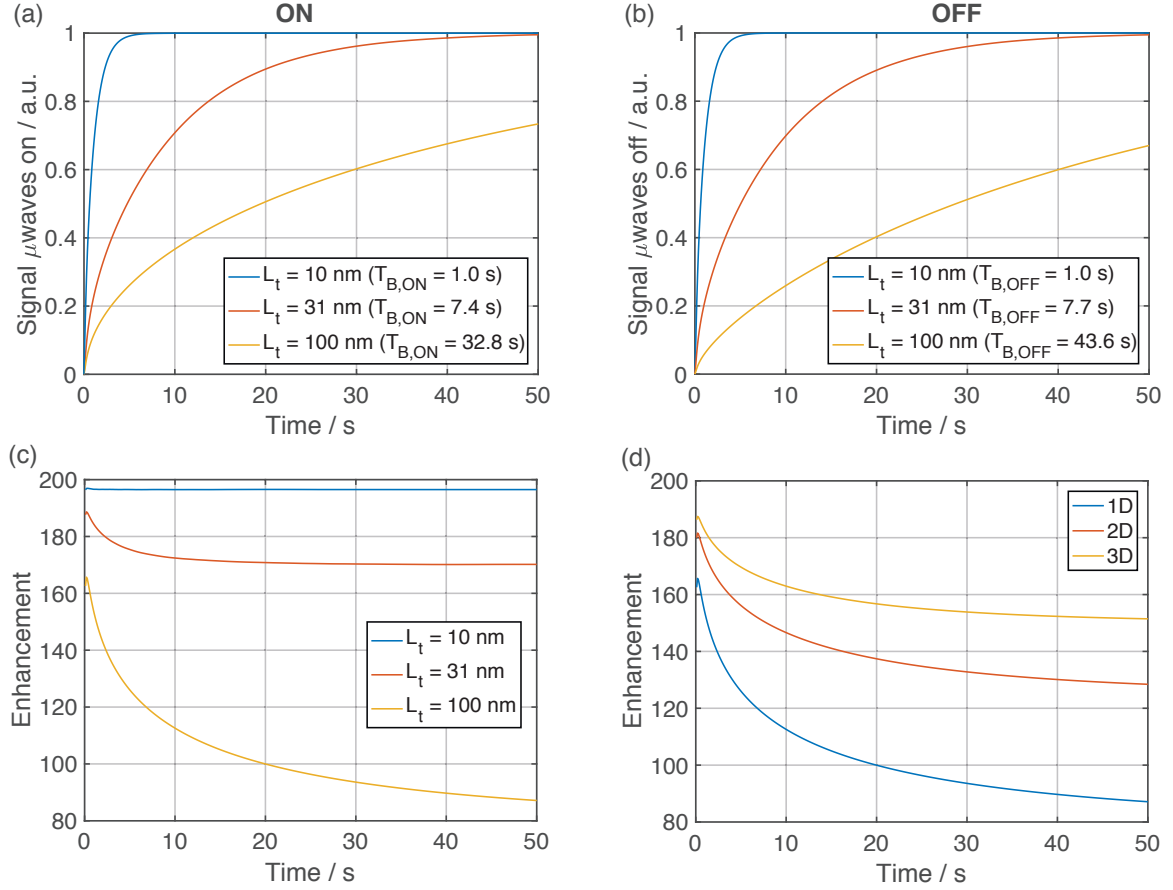

Figure 2.6: Simulated target signals with (a) and without (b) microwave irradiation and enhancements (c) as a function of time for different target sizes (L_t). For panel (d) the size L_t was fixed to 100 nm and only the dimensionality was changed. Parameters are shown in the following table.

parameter	L_t	L_s	$T_{B,s}$	T_1	C_s	C_t	D_s	D_t	ε_0	ε_{depo}	v_r	θ
value	varies	100	1	100	110	10	$8.8\ 10^{-4}$	$3.7\ 10^{-5}$	200	0.5	12.5	0.5
unit	nm	nm	s	s	$mol.L^{-1}$	$mol.L^{-1}$	$\mu m^2 s^{-1}$	$\mu m^2 s^{-1}$			kHz	

In Figure 2.6a-b as expected, both target build-up times with and without microwaves is predicted to increase with the size of the target. The enhancement decreases with the size of the target (Figure 2.6c), because relaxation in the target destroys the propagating hyperpolarization before it has time to spin diffuse through the whole target. As shown in Figure 2.6d, we observe that the enhancement of a spherical object is higher, with all other parameters being identical, than the enhancement for a linear object being polarized from the ends. Mathematically, it is coming from the fact that the ratio surface/volume is getting bigger with the dimensionality. Physically, it means that proportionally more spins are close to the surface inside a sphere than inside a disk or in a line.

At long polarization times, a steady state is achieved in which relaxation exactly balances the polarization flow into the target. The change in the steady-state enhancement and target build-up times as a function of the size of the target are shown in Figure 2.7. **The great interest of the steady-state enhancement is that it is only a function of the geometry (linear, cylindrical, or spherical), the target size L_t, and the characteristic diffusion length $\sqrt{D_t T_1}$.**
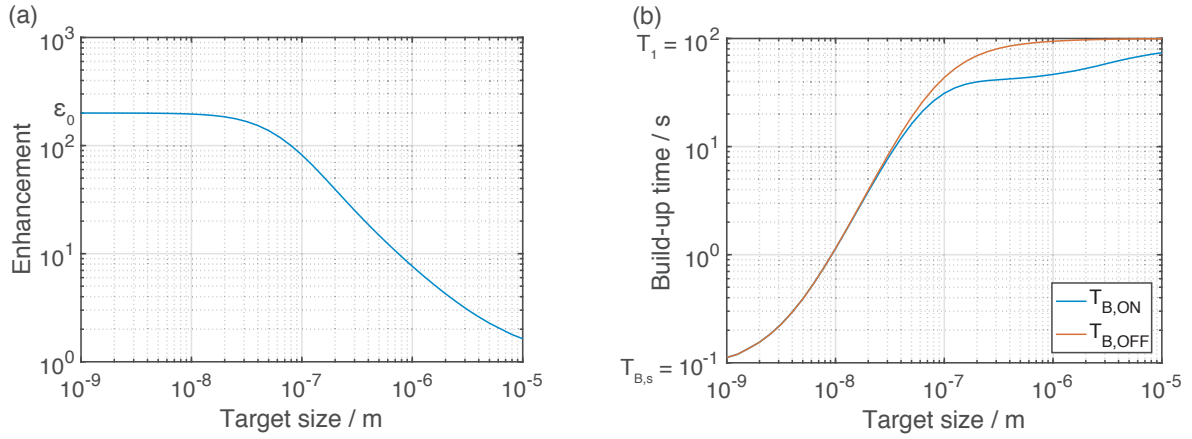

Figure 2.7: Simulated target (a) steady state enhancements and (b) build-up times as a function the target size for a linear symmetry (1D). In the simulations, $W_P \gg W_R$.

parameter	L_s	L_t	$T_{B,s}$	T_1	C_s	C_t	D_s	D_t	ε_0	ε_{depo}	v_r	θ
value	varies	100	0.1	100	110	10	$8.8\ 10^{-4}$	$3.7\ 10^{-5}$	200	1	12.5	0.5
unit	nm	nm	s	s	mol.L^{-1}	mol.L^{-1}	µm^{2}s^{-1}	µm^{2}s^{-1}			kHz	

As expected when the source polarizing power is much bigger than the target relaxing power, the steady state enhancement decreases with increasing target size, and the target build-up times increase with increasing target size. But now we want a quantitative relationship. When one is looking at the steady state solution of equation (2.8) assuming $W_P \gg W_R$, we find the steady state target polarization[42]:

$$P_{t,\infty}(x) = 1 + (P_s - 1)\frac{\cosh\left(\dfrac{x}{\sqrt{D_t T_1}}\right)}{\cosh\left(\dfrac{L_t}{\sqrt{D_t T_1}}\right)} \tag{2.20.1D}$$

for a 1D system represented by two infinite plans separated by $2L_t$ where P_s is the source steady state polarization, and w the position, we find

$$P_{t,\infty}(x) = 1 + (P_s - 1)\frac{I_1\left(\dfrac{x}{\sqrt{D_t T_1}}\right)}{I_0\left(\dfrac{L_t}{\sqrt{D_t T_1}}\right)} \tag{2.20.2D}$$

for a 2D system represented by an infinite cylinder radius L_t polarized by the outside, where I_1 and I_0 are the modified Bessel functions of first and zero order respectively, and we find

51

$$P_{t,\infty}(x) = 1 + \frac{P_s - 1}{x} \frac{L_t}{\sqrt{D_t T_1}} \frac{\sinh\left(\frac{x}{\sqrt{D_t T_1}}\right)}{\sinh\left(\frac{L_t}{\sqrt{D_t T_1}}\right)} \tag{2.20.3D}$$

for a 3D system represented by a sphere of radius L_t polarized by the outside. These functions were found with Mathematica.

When taking equation (2.20.1D), we find $P_{t,\infty}(\rho_t) \approx 0.36 \cdot P_s$ which confirms that the diffusion length is defined as the distance from the source where the target polarization is about 36% of the source polarization.

Assuming no depolarization in the source, we can deduce from equations (2.20) the steady state enhancements:

$$\varepsilon_{t,\infty} = 1 + (\varepsilon_0 - 1)\frac{\sqrt{D_t T_1}}{L_t}\left[\tanh\left(\frac{L_t}{\sqrt{D_t T_1}}\right)\right] \tag{2.21.1D}$$

for a 1D system,

$$\varepsilon_{t,\infty} = 1 + (\varepsilon_0 - 1)\frac{2\sqrt{D_t T_1}}{L_t}\left[\frac{I_1\left(\frac{L_t}{\sqrt{D_t T_1}}\right)}{I_0\left(\frac{L_t}{\sqrt{D_t T_1}}\right)}\right] \tag{2.21.2D}$$

for a 2D system, and

$$\varepsilon_{t,\infty} = 1 + (\varepsilon_0 - 1)\frac{3\sqrt{D_t T_1}}{L_t}\left[\coth\left(\frac{L_t}{\sqrt{D_t T_1}}\right) - \frac{\sqrt{D_t T_1}}{L_t}\right] \tag{2.21.3D}$$

for a 3D system. It is interesting to see that the factor in front of $\sqrt{D_t T_1}$ at the left of the brackets increases when increasing dimensionality. This comes from the fact that the surface/volume ratio increases with dimensionality, i.e. more spins are close to the surface in a sphere than in a cylinder than in a plan. **Equations (2.21) fit perfectly to the simulated steady state enhancements in Figure 2.7a.** With depolarization, equation (2.21.1D) becomes:

$$\varepsilon_{t,\infty} = \frac{1 + \left(P_{0,ON} - 1\right)\frac{\sqrt{D_t T_1}}{L_t}\left[\tanh\left(\frac{L_t}{\sqrt{D_t T_1}}\right)\right]}{1 + \left(P_{0,OFF} - 1\right)\frac{\sqrt{D_t T_1}}{L_t}\left[\tanh\left(\frac{L_t}{\sqrt{D_t T_1}}\right)\right]} \tag{2.21.1D.bis}$$

In real cases however, the polarizing power of the radical solution is not necessarily much bigger than the target relaxing power. In the general case without assuming anything on the polarizing powers, it is still possible to extract analytical solutions from equation (2.8). We define the scaling parameter λ as:

$$\lambda = \frac{C_s}{C_t} \sqrt{\frac{D_s T_1}{D_t T_B}} \tag{2.22}$$

where C_s and C_t represent the proton concentration of the source and target respectively. At the edge of the system, the boundary conditions are the same as in the previous case. But at the border between the source and target, two conditions must be added:

$$P_s(L_t) = P_t(L_t) \tag{2.23}$$

where L_t represents the position at the border between source and target, and

$$C_s D_s \frac{\partial P_s}{\partial x}(L_t) = C_t D_t \frac{\partial P_t}{\partial x}(L_t) \tag{2.24}$$

Equation (2.23) imposes that the polarization must be continuous at the border, and equation (2.24) imposes the magnetization flux to be constant through the border. With these conditions added, we find that the steady state target polarization is in 1D systems:

$$P_{t,\infty}(x) = 1 + (P_s - 1) \frac{\lambda \cosh\left(\frac{x}{\sqrt{D_t T_1}}\right)}{\lambda \cosh\left(\frac{L_t}{\sqrt{D_t T_1}}\right) + \sinh\left(\frac{L_t}{\sqrt{D_t T_1}}\right)\left[\dfrac{\tanh\left(\frac{L_t + L_s}{\sqrt{D_s T_B}}\right) - \coth\left(\frac{L_t}{\sqrt{D_s T_B}}\right)}{1 - \tanh\left(\frac{L_t + L_s}{\sqrt{D_s T_B}}\right)\coth\left(\frac{L_t}{\sqrt{D_s T_B}}\right)}\right]} \tag{2.25}$$

Assuming no depolarization, the steady state target enhancement can be calculated as:

$$\varepsilon_{t,\infty} = 1 + (\varepsilon_0 - 1)\frac{\sqrt{D_t T_1}}{L_t} \frac{1}{\coth\left(\frac{L_t}{\sqrt{D_t T_1}}\right) + \frac{1}{\lambda}\left[\dfrac{\tanh\left(\frac{L_t + L_s}{\sqrt{D_s T_B}}\right) - \coth\left(\frac{L_t}{\sqrt{D_s T_B}}\right)}{1 - \tanh\left(\frac{L_t + L_s}{\sqrt{D_s T_B}}\right)\coth\left(\frac{L_t}{\sqrt{D_s T_B}}\right)}\right]} \tag{2.26}$$

for 1D. We confirm for $\lambda \gg 1$ (i.e. when the source polarizing power is much bigger than the target polarizing power, i.e. $W_P \gg W_R$) that equations (2.25) and (2.26) reduce to equation (2.20.1D) and (2.21.1D), respectively.

Again, these analytical expressions fit perfectly the numerical simulations.

Now that the numerical model is build and seems reliable, we can use this model to simulate polarization dynamics during saturation recovery experiments in radical frozen solutions (chapter 3) and heterogeneous systems (chapter 4).

References

(1) Wilson, J. D.; Bechtel, D. B.; Todd, T. C.; Seib, P. A. Measurement of wheat starch granule size distribution using image analysis and laser diffraction technology *Cereal Chemistry* **2006**, *83*, 259-268.

(2) Hendrich, C.; Favre, L.; Ievlev, D. N.; Dobrynin, A. N.; Bras, W.; Hormann, U.; Piscopiello, E.; Van Tendeloo, G.; Lievens, P.; Temst, K. Measurement of the size of embedded metal clusters by mass spectrometry, transmission electron microscopy, and small-angle X-ray scattering *Appl. Phys. A-Mater. Sci. Process.* **2007**, *86*, 533-538.

(3) Amaral, S. S.; de Carvalho, J. A., Jr.; Martins Costa, M. A.; Pinheiro, C. An Overview of Particulate Matter Measurement Instruments *Atmosphere* **2015**, *6*, 1327-1345.

(4) Telkki, V. V.; Lounila, J.; Jokisaari, J. Determination of pore sizes and volumes of porous materials by Xe-129 NMR of xenon gas dissolved in a medium *Journal of Physical Chemistry B* **2005**, *109*, 24343-24351.

(5) Chemmi, H.; Petit, D.; Levitz, P.; Denoyel, R.; Galarneau, A.; Korb, J.-P. Noninvasive Experimental Evidence of the Linear Pore Size Dependence of Water Diffusion in Nanoconfinement *J. Phys. Chem. Let.* **2016**, *7*, 393-398.

(6) Clauss, J.; Schmidt-Rohr, K.; Spiess, H. W. Determination of Domain Sizes in Heterogeneous Polymer by Solid-State NMR *Acta Polymerica* **1993**, *44*, 1-17.

(7) Demco, D. E.; Johansson, A.; Tegenfeldt, J. Proton spin diffusion for spatial heterogeneity and morphology investigations of polymers *Solid State Nucl. Magn. Reson.* **1995**, *4*, 13.

(8) Schmidt-Rohr, K.; Spiess, H. W. *Multidimensional Solid-State NMR and Polymers*; Second ed.; Academic Press: London, 1996.

(9) Graf, R.; Demco, D. E.; Gottwald, J.; Hafner, S.; Spiess, H. W. Dipolar couplings and internuclear distances by double-quantum nuclear magnetic resonance spectroscopy of solids *J. Chem. Phys.* **1997**, *106*, 885-895.

(10) Goldman, M.; Shen, L. Spin-Spin Relaxation in LaF3 *Phys. Rev.* **1966**, *144*, 321.

(11) Schmidt-Rohr, K.; Clauss, J.; Blumich, B.; Spiess, H. W. Miscibility of polymer blends investigated by H-1 spin diffusion and C-13 NMR detection *Magn. Reson. Chem.* **1990**, *28*, S3-S9.

(12) VanderHart, D. L.; McFadden, G. B. Some perspectives on the interpretation of proton NMR spin diffusion data in terms of polymer morphologies *Solid State Nucl. Magn. Reson.* **1996**, *7*, 45-66.

(13) Schmidt-Rohr, K.; Clauss, J.; Blümich, B.; Spiess, H. W. Miscibility of polymer blends investigated by H-1 spin diffusion and C-13 NMR detection *Magn. Reson. Chem.* **1990**, *28*, S3.

(14) Schmidt-Rohr, K.; Clauss, J.; Spiess, H. W. Correlation of structure, mobility, and morphological information in heterogeneous polymer materials by 2-dimensional wideline-separation NMR spectroscopy *Macromolecules* **1992**, *25*, 3273-3277.

(15) Schlagnitweit, J.; Tang, M.; Baias, M.; Richardson, S.; Schantz, S.; Emsley, L. A solid-state NMR method to determine domain sizes in multi-component polymer formulations *J. Mag. Res.* **2015**, *261*, 43-48.

(16) van der Wel, P. C. A.; Hu, K. N.; Lewandowski, J.; Griffin, R. G. Dynamic nuclear polarization of amyloidogenic peptide nanocrystals: GNNQQNY, a core segment of the yeast prion protein Sup35p *Journal of the American Chemical Society* **2006**, *128*, 10840-10846.

(17) Rossini, A. J.; Zagdoun, A.; Hegner, F. S.; Schwarzwälder, M.; Gajan, D.; Copéret, C.; Lesage, A.; Emsley, L. Dynamic Nuclear Polarization NMR Spectroscopy of Microcrystalline Solids *J. Am. Chem. Soc.* **2012**, *134*, 16899–16908.

(18) Lafon, O.; Thankamony, A. S. L.; Kobayashi, T.; Carnevale, D.; Vitzthum, V.; Slowing, II; Kandel, K.; Vezin, H.; Amoureux, J. P.; Bodenhausen, G.; Pruski, M. Mesoporous Silica Nanoparticles Loaded with Surfactant: Low Temperature Magic Angle Spinning C-13 and Si-29 NMR Enhanced by Dynamic Nuclear Polarization *Journal of Physical Chemistry C* **2013**, *117*, 1375-1382.

(19) Rossini, A. J.; Widdifield, C. M.; Zagdoun, A.; Lelli, M.; Schwarzwälder, M.; Copéret, C.; Lesage, A.; Emsley, L. Dynamic Nuclear Polarization Enhanced NMR Spectroscopy for Pharmaceutical Formulations *J. Am. Chem. Soc.* **2014**, *136*, 2324-2334.

(20) Schlagnitweit, J.; Tang, M.; Baias, M.; Richardson, S.; Schantz, S.; Emsley, L. Nanostructure of Materials Determined by Relayed Paramagnetic Relaxation Enhancement *J. Am. Chem. Soc.* **2015**, *137*, 12482-12485.

(21) Smith, A. A.; Corzilius, B.; Barnes, A. B.; Maly, T.; Griffin, R. G. Solid effect dynamic nuclear polarization and polarization pathways *J. Chem. Phys.* **2012**, *136*, 015101.

(22) Redfield, A. G. SPATIAL DIFFUSION OF SPIN ENERGY *Phys. Rev.* **1959**, *116*, 315-316.

(23) Redfield, A. G.; Yu, W. N. MOMENT-METHOD CALCULATION OF MAGNETIZATION AND INTERSPIN-ENERGY DIFFUSION *Phys. Rev.* **1968**, *169*, 443-&.

(24) Lowe, I. J.; Gade, S. DENSITY-MATRIX DERIVATION OF SPIN-DIFFUSION EQUATION *Phys. Rev.* **1967**, *156*, 817-&.

(25) Kaplan, J. I. Modified linear-response method for obtaining the spin-diffusion constant of a rigid dipole system *Physical Review B-Solid State* **1970**, *2*, 4578-4579.

(26) Suter, D.; Ernst, R. R. SPIN DIFFUSION IN RESOLVED SOLID-STATE NMR-SPECTRA *Physical Review B* **1985**, *32*, 5608-5627.

(27) Bloembergen, N. ON THE INTERACTION OF NUCLEAR SPINS IN A CRYSTALLINE LATTICE *Physica* **1949**, *15*, 386-426.

(28) Nolden, I. M.; Silbey, R. J. Simulation of spin diffusion in a disordered system *Physical Review B* **1996**, *54*, 381-387.

(29) Butler, M. C.; Dumez, J. N.; Emsley, L. Dynamics of large nuclear-spin systems from low-order correlations in Liouville space *Chemical Physics Letters* **2009**, *477*, 377-381.

(30) Dumez, J. N.; Butler, M. C.; Salager, E.; Elena-Herrmann, B.; Emsley, L. Ab initio simulation of proton spin diffusion *Physical Chemistry Chemical Physics* **2010**, *12*, 9172-9175.

(31) Dumez, J. N.; Emsley, L. A master-equation approach to the description of proton-driven spin diffusion from crystal geometry using simulated zero-quantum lineshapes *Physical Chemistry Chemical Physics* **2011**, *13*, 7363-7370.

(32) Dumez, J. N.; Halse, M. E.; Butler, M. C.; Emsley, L. A first-principles description of proton-driven spin diffusion *Physical Chemistry Chemical Physics* **2012**, *14*, 86-89.

(33) Halse, M. E.; Zagdoun, A.; Dumez, J. N.; Emsley, L. Macroscopic nuclear spin diffusion constants of rotating polycrystalline solids from first-principles simulation *Journal of Magnetic Resonance* **2015**, *254*, 48-55.

(34) Veshtort, M.; Griffin, R. G. Proton-driven spin diffusion in rotating solids via reversible and irreversible quantum dynamics *Journal of Chemical Physics* **2011**, *135*.

(35) Abragam, A.; Proctor, W. G. SPIN TEMPERATURE *Phys. Rev.* **1958**, *109*, 1441-1458.

(36) Fick, A. *Ueber diffusion*; J.A. Barth, 1855.

(37) Roos, M.; Micke, P.; Saalwachter, K.; Hempel, G. Moderate MAS enhances local H-1 spin exchange and spin diffusion *Journal of Magnetic Resonance* **2015**, *260*, 28-37.

(38) Chaudhari, S. R.; Wisser, D.; Pinon, A. C.; Berruyer, P.; Gajan, D.; Tordo, P.; Ouari, O.; Reiter, C.; Engelke, F.; Coperet, C.; Lelli, M.; Lesage, A.; Emsley, L. Dynamic Nuclear Polarization Efficiency Increased by Very Fast Magic Angle Spinning *Journal of the American Chemical Society* **2017**, *139*, 10609-10612.

(39) Perras, F. A.; Wang, L. L.; Manzano, J. S.; Chaudhari, U.; Opembre, N. N.; Johnson, D. D.; Slowing, I.; Pruski, M. Optimal sample formulations for DNP SENS: The importance of radical-surface interactions *Current Opinion in Colloid & Interface Science* **2018**, *33*, 9-18.

(40) Chaudhari, S. R.; Berruyer, P.; Gajan, D.; Reiter, C.; Engelke, F.; Silverio, D. L.; Coperet, C.; Lelli, M.; Lesage, A.; Emsley, L. Dynamic nuclear polarization at 40 kHz magic angle spinning *Physical Chemistry Chemical Physics* **2016**, *18*, 10616-10622.

(41) Mentink-Vigier, F.; Paul, S.; Lee, D.; Feintuch, A.; Hediger, S.; Vega, S.; De Paepe, G. Nuclear depolarization and absolute sensitivity in magic-angle spinning cross effect dynamic nuclear polarization *Physical Chemistry Chemical Physics* **2015**, *17*, 21824-21836.

(42) Pinon, A. C.; Schlagnitweit, J.; Berruyer, P.; Rossini, A. J.; Lelli, M.; Socie, E.; Tang, M. X.; Pham, T.; Lesage, A.; Schantz, S.; Emsley, L. Measuring Nano- to Microstructures from Relayed Dynamic Nuclear Polarization NMR *Journal of Physical Chemistry C* **2017**, *121*, 15993-16005.

Chapter 3:
Polarization dynamics
in homogeneous systems

In this chapter, we study polarization dynamics in homogeneous systems, and compare experimental measurements of saturation recovery experiments with numerical simulations in order to understand ins and outs of polarization dynamics. Here, "homogeneous" means that the typical length to be polarized is smaller than the characteristic diffusion length. It is the case for frozen solutions containing few mM of radical molecules. We study frozen radical solutions here. We first start by using the numerical model described in chapter 2 to model the flow of polarization in a radical frozen solution. Then, we examine the influence of the proton and radical concentration

3.1 Radical frozen solution

The most used radical molecules in MAS DNP at EPFL are the radicals TEKPol[1] and AMUPol.[2] For dDNP, the most commonly used radical molecule is TEMPO or its derivatives such as 4-hydroxy-TEMPO (TEMPOL).
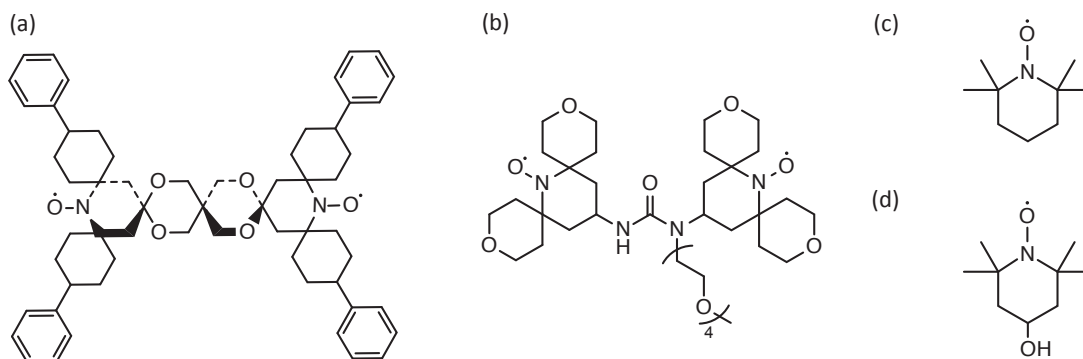

Figure 3.1: Schematic representation of the biradicals (a) TEKPol, (b) AMUPol, (c) TEMPO, and (d) 4-hydroxy-TEMPO (TEMPOL).

As mentioned in chapter 1, the DNP samples are optimized for DNP at 100 K since, among other conditions, they fulfil at least 2 of the 4 criteria mentioned in chapter 1:

1. TEKPol is soluble in 1,1,2,2-tetrachloroethane (TCE) and AMUPol is soluble in glycerol-d_8/D$_2$O/H$_2$O (6/3/1).
2. These solvents form a glassy matrix once frozen, which provides a homogeneous distribution of radicals in the frozen state.

Now for even better performance, we try fulfil the two last criteria:

3. The sample must have the optimal radical concentration

4. The sample must have the optimal proton concentration

We study the effect of radical and proton concentrations in the two next sections.

3.1.1 Radical concentration

In this section, we show how the radical concentration of a frozen solution influences its enhancement and build-up time.

Concerning criterion 3, several examples from the literature have shown that the enhancement provided by a biradical is greatly dependent on the radical concentration. Takahashi *et al.*[3] have measured the ^{1}H enhancement as well as the ^{1}H build-up time $T_{B,ON}$(^{1}H) in the presence of microwaves for a radical solution of DMSO-d_6/D_2O/H_2O (6/3/1) containing 2 M of ^{13}C-urea for various TOTAPOL[4] concentrations as shown in Figure 3.2g. It is possible to reproduce most of these experimental results with numerical simulations described in chapter 2 with considering the environment around the electron as described in chapter 1.

In Figure 3.2a-b-d, r_{CE} corresponds to the radius at which spins are directly polarized by cross-effect. It is, by definition, the border between the source spins and the target spins in such systems. In panel (c) is represented the percentage of detectable signal as a function of the distance from the electron. Panel (e) represents the spatial variation of the spin diffusion coefficient close to the electron. In Panel (f), we plot the variation of T_1 due to PRE effect close to the electron location. In panel (g) is represented the proton enhancement as a function of the TOTAPOL concentration, and in panel (h) is represented the build-up time as a function of the TOTAPOL concentration.

We can see from Figure 3.2g that the early behaviour (below 20 mM) of the enhancement as a function of the TOTAPOL concentration is well reproduced. This region corresponds to where the directly polarized protons [1]H$_s$ inside the source (i.e. inside r_{CE}) must polarize relatively less and less protons [1]H$_t$ in the target (i.e. outside r_{CE}) when increasing the TOTAPOL concentration. For example, at 2 mM TOTAPOL, one [1]H$_s$ must polarize 380 [1]H$_t$, whereas at 20 mM TOTAPOL, one [1]H$_s$ must polarize only 38 [1]H$_t$. It is thus expected that at low radical concentration, the polarization provided by one source proton must be spread out over a large number of target protons, resulting in small individual target proton enhancements, and vice versa. In other words, the polarizing power of the source protons is the limiting factor. The decreasing part of the graph in Figure 3.2g is expected not to be reproduced by numerical simulations. Indeed, the numerical model only simulates the transfer of polarisation from the source protons to the target protons **through spin diffusion**. It does **not** simulate the efficiency of the cross effect, or the unfavourable electron-electron dipolar couplings at high radical concentrations. This is why the decreasing enhancement at high radical concentration which is due to strong electron-electron dipolar couplings is not reproduced by numerical simulations.

We need to be careful in this situation not to over fit the data: only two data sets are fitted whereas 5 parameters can be changed to fit the data. As long the fitted parameters are physically reasonable, we will consider that these fitted parameters are good guesses for future fittings.

In Figure 3.2h we notice that the build-up time of the radical solution depends on the radical concentration. The reasoning is the same: at low radical concentration, the fast build-up (here less than a second, see Figure 3.2f) of the source protons is overwhelmed by the high number of target protons having a slow build-up time (here 45 s). As the radical concentration increases, the average build-up time shifts in favour of the source build-up time as the number of source protons proportionally increases compared to the number of target protons.
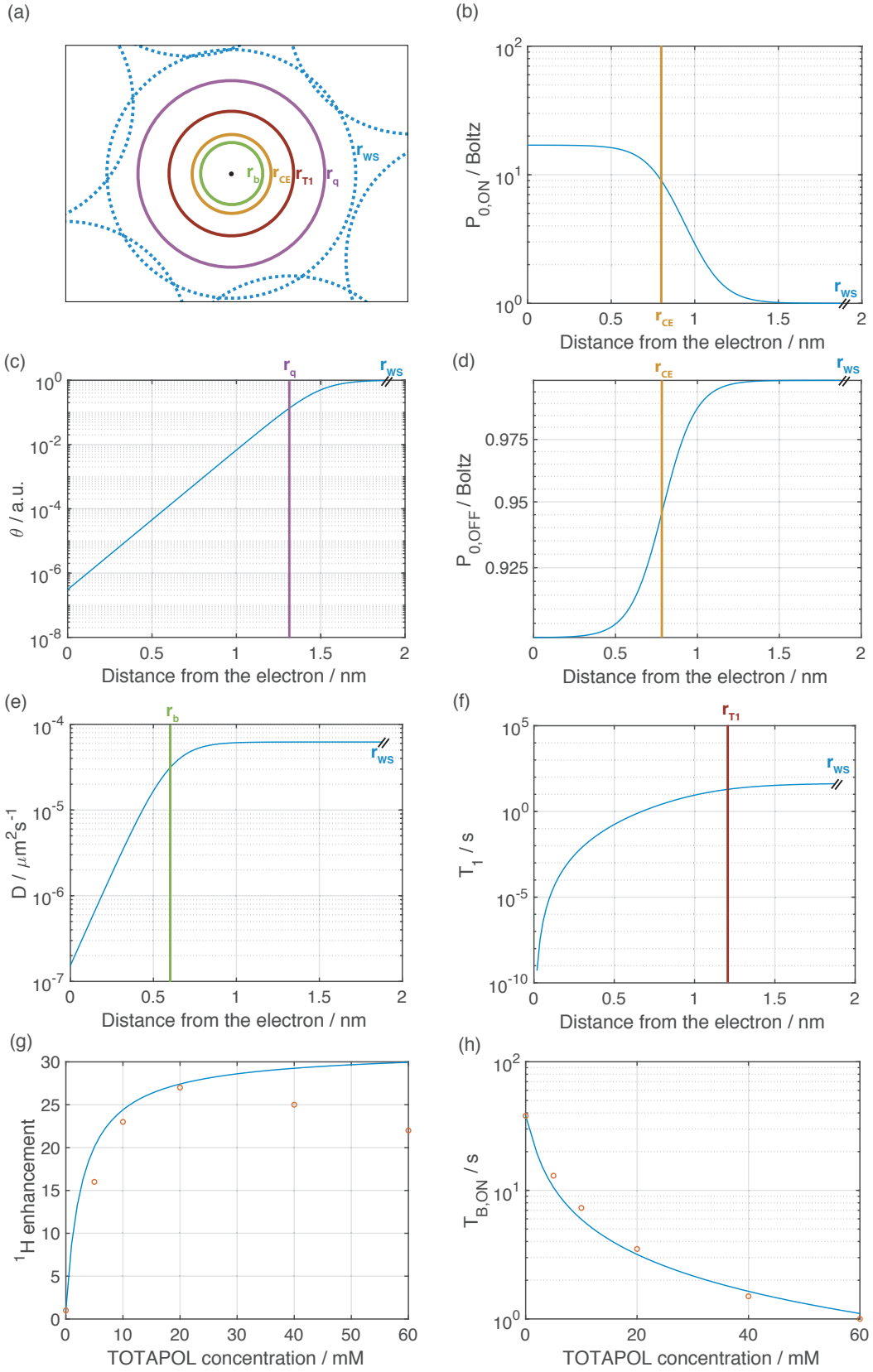
Figure 3.2: (a) Schematic representation of the characteristic radii around the electron location (black point). (b) & (d) Local equilibrium polarizations as a function of the distance from the electron. Spins at a shorter distance from the electron than r_{CE} (i.e. spins located in the source) are hyperpolarized by direct cross-effect up to a value of 32 in the µwaves on case (b) or to 0.5 because of depolarization in the µwaves off case (d). Remember: the polarization is expressed in units of Boltzmann polarization. The rest of the spins outside r_{CE} (i.e. spins located in the target) are hyperolarized by spin diffusion (c) Quenching factor as a function of the distance from the electron. Spins closer than r_q from the electron participate less and less to the NMR signal. (e) Diffusion coefficient as a function of the distance from the electron. Spins closer than r_b are less and less able to spin diffuse their polarization. (f) Longitudinal relaxation time as a function of the distance from the electron. Spins closer than r_{T1} have significantly reduced T_1. The two parallel black solid lines in (b) to (f) correspond to the fact that the Wigner-Seitz radius varies with the radical concentration. (g) ^{1}H enhancement and (h) ^{1}H build-up time µwaves on for a radical solution of DMSO-d_6/D_2O/H_2O (6/3/1) containing 2 M of ^{13}C-urea as a function of the TOTAPOL concentration at 100 K, 9.4 T and 8 kHz MAS. Experimental data were taken from ref 3. Error bars were not shown in original publication. All solid lines represent numerical simulations with the following parameters.

parameter	r_{CE}	r_{WS}	r_q	r_{T1}	r_b	C_H	D	$T_{1,t}$	ε_0	ε_{depo}	v_r
value	0.8	varies	1.3	1.2	0.6	11	6.2 10^{-5}	45	32	0.5	8
unit	nm	nm	nm	nm	nm	mol.L^{-1}	µm^{2}s^{-1}	s			kHz

The curve shape in Figure 3.2g can be characterized with the polarizing power of the source spins and the relaxing power of the target spins. Here, the polarizing/relaxing powers of the source/target spins are proportional the spin concentration in the source/target and their build-up/relaxation time T_B/T_1. We can plot the evolution of each polarizing and relaxing power as defined in chapter 2 as a function of the radical concentration (note here that the powers are expressed in watts instead of watts/litre as in chapter 2, which indicates that the source and target volumes are taken into account):
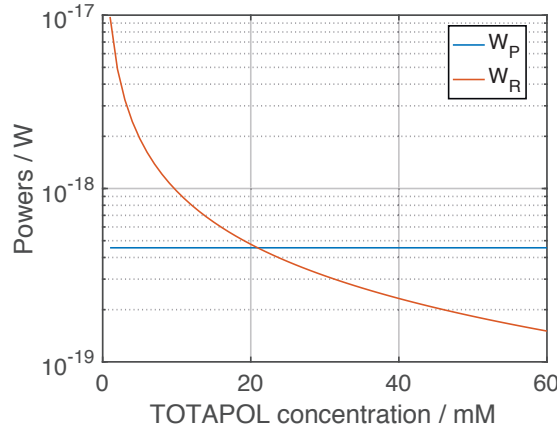

Figure 3.3: Simulated source polarizing W_P and target relaxing W_R powers as a function of the TOTAPOL concentration. The parameters for the simulations are the same as in Figure 3.2.

As expected, the polarizing power of the source spins doesn't vary as a function of the TOTAPOL concentration since r_{CE} doesn't vary. On the contrary, the number of spins in the target varies with the radical concentration since the average distance between radical changes. We notice that the source polarizing power at lower concentrations than 20 mM is smaller than the target relaxing power. It means that in this region, the polarization provided by the source must indeed be spread over the target protons. At higher TOTAPOL concentration than 20 mM, the energy provided by the source spins is bigger than the energy dissipated through the lattice from the target spins: the enhancement is close to reaching its maximum. But at higher TOTAPOL concentration than 20 mM, the strong electron-electron dipolar couplings decrease the efficiency of the cross-effect mechanisms at increase the PRE of target protons, leading to a decreasing enhancement.

The optimal radical concentration is at 20 mM for TOTAPOL but has been measured to be around 16 mM for TEKPol and AMUPol.[5,6]

Similar behaviour is found for the dDNP case in a static sample containing the water-soluble radical TEMPOL, as shown in Figure 3.4. In dDNP however, the mechanisms are solid effect, cross effect, and thermal mixing.[7] During a thermal mixing process, all protons and electrons are coupled. The build-up time thus depends on the relative electron-proton polarizing/relaxing powers. Consequently here, numerical simulations only reproduce the "cross-effect part" of the DNP mechanism.
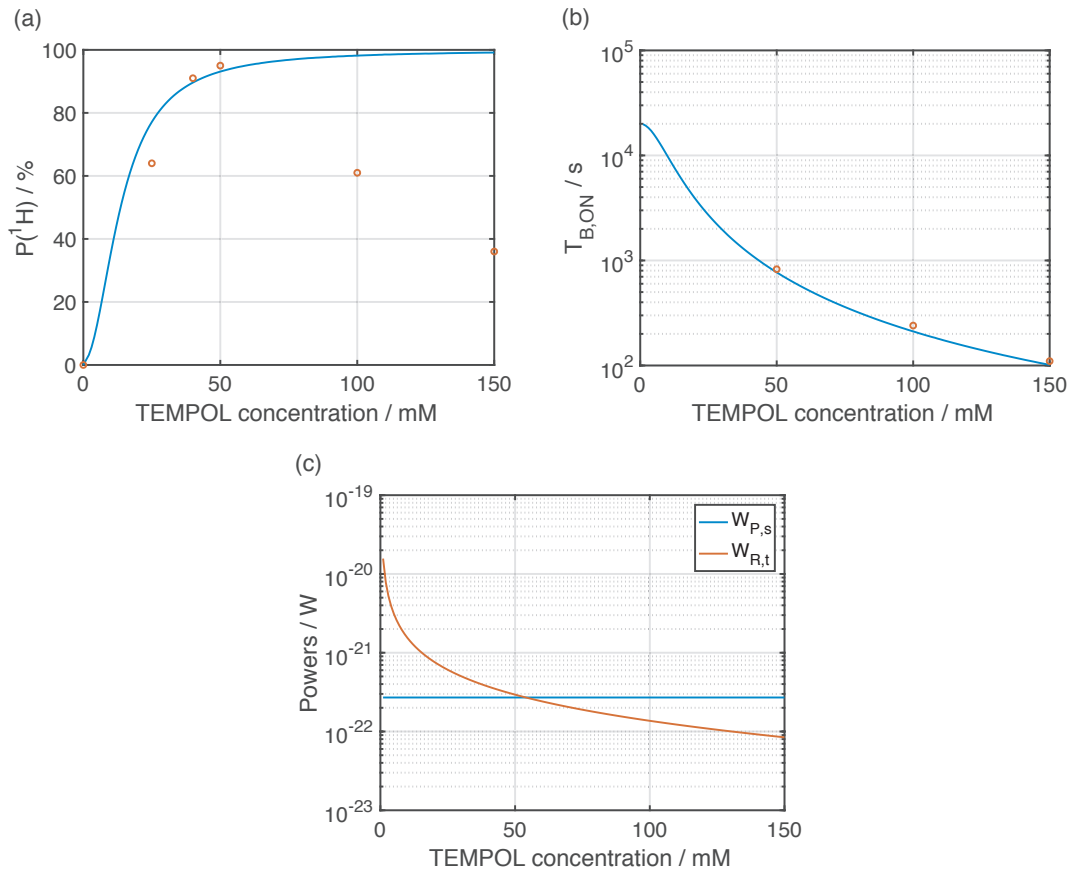

Figure 3.4: (a) ^{1}H polarization and (b) ^{1}H build-up time with microwaves for a radical solution of glycerol-H_8/H_2O (6/4) for different TEMPOL concentrations in a static sample at 1.2 K and 6.7 T. (c) Simulated source and target polarizing and relaxing powers as a function of the TOTAPOL concentration. Error bars are within the points' width. Solid lines represent numerical simulations with the following parameters.

parameter	r_{CE}	r_{WS}	r_q	r_{T1}	r_b	$C(^1H)$	D_0	$T_{1,t}$	$T_{B,s}$	P_0	ε_{depo}	v_r
value	1	varies	1.3	1.2	0.6	110	$1.4\ 10^{-3}$	$20\ 10^3$	1500	100	1	0
unit	nm	nm	nm	nm	nm	mol.L^{-1}	µm^{2}s^{-1}	s	s	%		kHz

In both Figures 3.2 and 3.4, a random distribution of molecules leads to a random distribution of inter particle distances and Wigner-Seitz radii. A Weibull distribution of Wigner-Seitz radii could be taken for these numerical simulations, but this has no or little effect on the observable parameters.

We thus use 10-15 mM radical concentration in MAS DNP and 50 mM in dDNP. But this optimization was made at a given proton concentration. It means that the proton concentration must also be optimized, as shown in the next section.

3.1.2 Proton concentration

In this section, we vary the proton concentration of a radical solution in order to show that high enhancements can still be achieved at low radical concentration. We also show that optimizing the enhancement is quite different from optimizing the polarizing power, and that sometimes the polarizing power matters more than the enhancement.

The polarization and the μwaves on build-up time of a solution of glycerol-d_8/glycerol-H_8/D_2O/H_2O (w/x/y/z) containing 50 mM of TEMPOL where the ratios w/x/y/z were varied was measured. We make sure that there is always 60% of glycerol and 40% of water in the sample, in order to have a nice glassy matrix. The experimental results are reported in Figure 3.5.
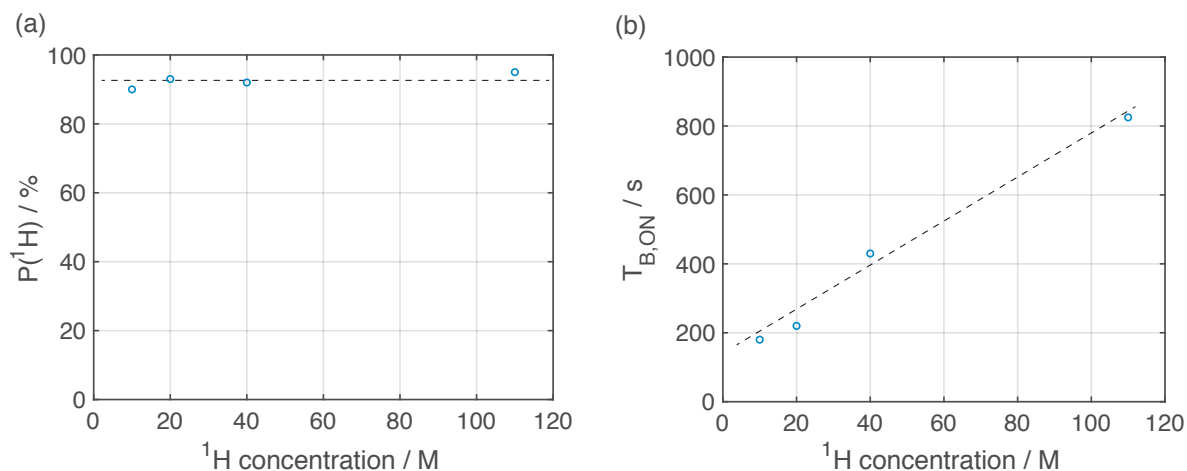

Figure 3.5: (a) ^{1}H enhancement and (b) ^{1}H build-up time with microwaves for a radical solution of glycerol-d_8/glycerol-H_8/D_2O/H_2O (w/x/y/z) containing 50 mM of TEMPOL as a function of the proton concentration at 1.2 K and 6.7 T in a static sample. Dashed lines are represented to guide the eye.

When the hyperpolarization is occurring in dDNP, the sample is at a temperature of 1.2 K. At this temperature, the intrinsic T_1 of the target protons is on the order of tens of thousands of seconds, as predicted by numerical simulations in Figure 3.4. Here, the relative number of source and target spins remains constant since the radical concentration is unchanged. Thus, the powers to be compared here are no longer the source and target powers, but rather the electron and proton powers.

At 50 mM TEMPOL in a solvent containing 111 M of proton spins, 1 electron must polarize 4440 proton spins, whereas at a concentration of 11 M of proton spins (and identical TEMPOL concentration), 1 electron must polarize 444 proton spins to achieve a given level of polarization. One could then expect a higher polarization when 1 electron would polarize 444 protons. But we notice in Figure 3.5 that the steady state polarization in the presence of microwaves is not a function of the TEMPOL concentration in the range of concentrations probed. The only variation observed is the time required to reach this steady state polarization, as shown in Figure 3.5b. **It means that at 1.2 K, the polarizing power of the electrons is bigger than the relaxing power of the protons, since T_1s here are much bigger than the observed build-up times.** This explains why the steady state polarization is constant whereas the build-up time varies with the proton concentration.

Similar experiments were performed at 100 K in MAS DNP. At 100 K, the difference is that the intrinsic T_1 cannot be considered as much bigger than typical build-up times, in fact they do vary with the proton concentration (Figure 3.6a).

In order to probe the PRE strength in the presence of radicals (here 2 and 12 mM), it is thus important to plot $1-T_B/T_1$ which encodes the PRE strength (Figure 3.6b: higher $1-T_B/T_1$ implies higher PRE due to free electrons). We notice that the PRE strength is becoming smaller as the proton concentration increases. It means that the relaxing power of AMUPol molecules is becoming the limiting factor when increasing proton concentration: one AMUPol molecule has to relax too many protons, thus the relaxation is less efficient. We notice that the PRE strength is bigger for 12 mM than for 2 mM as expected, due to a higher radical concentration. The proton dependence of the PRE strength is less intense for 12 mM than for 2 mM since more electrons are relatively less sensible to the proton concentration for 12 than for 2 mM.

The proton enhancement also depends on the proton concentration as shown in Figure 3.6c. We first see that the enhancement is higher at 12 mM than at 2 mM radical concentration, since the source polarizing power is relatively higher at 12 mM than at 2 mM. We also notice that the enhancement decreases with increasing proton concentration, since the same magnetic energy must be spread over more protons at high proton concentrations. We finally notice that the dependence with the proton concentration is more intense for 2 mM than for 12 mM since at 2 mM the polarizing power of the electron is a more limiting factor than at 12 mM. At very low proton concentration, we see that the enhancement is roughly the same at 2 and 12 mM AMUPol. This is not surprising, since at very low protons concentration, T_1s are getting much longer, and the number of protons to be polarized is no longer the limiting factor. We must also note that an enhancement of 265 was measured at 100 s polarization time for 2 mM **and** 12 mM AMUPol at 3.5 M and 1.2 M protons respectively. This shows that **big enhancements (ε=265) can be reached even at low radical concentrations (2mM)**, as long as the proton concentration is low enough, and relaxation times are high enough, which is the case here.
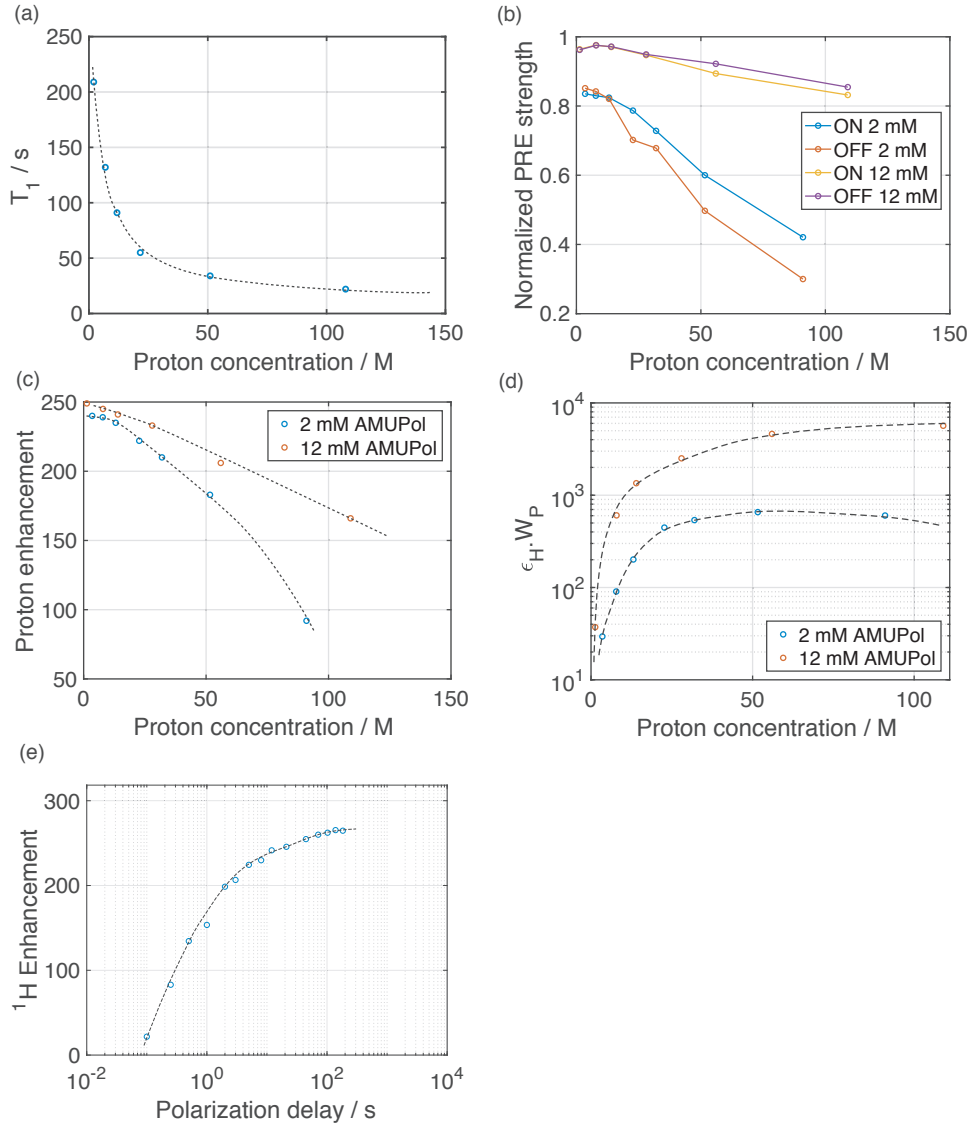
Figure 3.6: (a) Proton T_1 for a radical solution of glycerol-d_8/glycerol-H_8/D_2O/H_2O (w/x/y/z) as a function of the proton concentration at 100 K, 12.5 kHz MAS and 9.4 T. (b) PRE strength $(1-T_B/T_1)$ as a function of proton concentration for a radical solution of 2 and 12 mM AMUPol. (c) Proton enhancement measured at 10 s at 2 mM and 12 mM AMUPol as a function of proton concentration. (d) Product of enhancement times polarizing power as a function of proton concentration for 2 and 12 mM AMUPol. (e) Proton enhancement as a function of polarization delay for a solution containing 2 mM AMUPol and 3.5 M of protons.

In Figure 3.6d is plotted the product of the proton enhancement and the polarizing power (i.e. $\varepsilon_H.C_P.C_H/T_{B,ON}$). We notice that this product is maximized for a proton concentration of about 50 M for 2 mM. For 12 mM, this maximum is reached at even higher proton concentrations. **It means that the polarizing power is maximized at higher proton concentrations whereas the enhancement is maximized at lower proton concentrations.** This is why goals must be defined for each experiment: in an experiment where only surface enhancement is desired, low proton concentrations are preferable (usually 11 M is fine, since significant spin diffusion is still needed), whereas **if the sample to be**

polarized contains a high proton concentration (typically 70 M for polystyrene), higher proton concentrations in the radical solution are preferable, as explained in more details in chapter 4.

Figure 3.6e shows that at 2 mM AMUPol and 3.5 M protons, the enhancement takes time to establish. Indeed, at 2 mM AMUPol, the average distance between radicals is 11.7 nm and at 3.5 M, the spin diffusion coefficient is greatly reduced. This explains why the enhancement increases with time at 3.5 M protons whereas was measured to be constant with time for higher proton concentrations.

Reducing the radical and proton concentration can still lead to high enhancements, but we measured that the contribution factor (part of the signal observed due to both quenching and depolarization, introduced in chapter 2) is not increased: it is still about 50% as for AMUPol and TEKPol at 9.4 T and 100 K, whereas build-up times are much longer at low radical concentrations. Thus, the overall sensitivity enhancement Σ as defined in ref 5 is not increased by diluting radical and proton concentrations. The fact that the contribution factor is not reduced at low radical concentrations comes from the fact that depolarization is mainly responsible for the contribution factor in these nitroxide radicals.

These dDNP and MAS DNP observations still cannot be reproduced with current numerical simulations. Indeed, when the proton concentration changes, the quantities to be compared are the electron and proton polarizing powers. The electronic polarizing power depends on the cross effect and thermal mixing efficiencies[7], which are not in the scope of these numerical simulations which only simulate thermodynamic processes: here we only simulate what is transferred via spin diffusion.

It must be noted that deuteration of the radical molecule itself has an impact on the enhancement. Perras *et al.*[8] showed that bTbK and TOTAPOL derivative display a significant increase in DNP enhancement as well as longer build-up times. As a result of deuteration, less electron polarization will be spent repolarizing the rapidly relaxing ^{1}H spins inside the spin diffusion barrier. Besides, deuteration leads to longer T_{1e}, rending the cross effect mechanism more efficient.

Since polarization is diffused from the source to the target through spin diffusion, it seems legitimate to wonder what happens when the spin diffusion coefficient changes, such as when the MAS rate varies.

3.2 effect of MAS

In these sections, we show that the effect of MAS on the enhancement is some system can be counter-intuitive. We explain how the enhancement can increase with increasing MAS rate using the numerical model presented in chapter 2. We also explain why this effect is occurring with Overhauser DNP and not with cross-effect DNP.

3.2.1 Overhauser effect vs MAS

Part of this section is adapted with permission from Chaudhari, S. R.; Wisser, D.; Pinon, A. C.; Berruyer, P.; Gajan, D.; Tordo, P.; Ouari, O.; Reiter, C.; Engelke, F.; Coperet, C.; Lelli, M.; Lesage, A.; Emsley, L. Dynamic Nuclear Polarization Efficiency Increased by Very Fast Magic Angle Spinning *Journal of the American Chemical Society* **2017**, *139*, 10609-10612.

Bulk radical solutions may contain some paramagnetic impurities, even at very low concentrations. We will see here that these impurities can lead to unexpected effects.

Let us consider here the Overhauser effect (OE).[9] The radical molecule suited for the Overhauser effect is here α,γ-bisdiphenylene-β-phenylallyl (BDPA). This carbon-centered radical molecule displays efficient OE in the solvent *orto*-terphenyl (OTP) and leads to no depolarization.[10] A mixture of OTP-d_{14}/OTP-H_{14} (95/5) possesses a long intrinsic proton spin-lattice relaxation time ($T_1 > 90$ s). Consequently, it was predicted[10] that a radical solution of 60 mM BDPA in OTP displays a proton build-up time of $T_{B,RS} = 73$ s if no impurities were present (we use here the $T_{B,RS}$ notation to designate the build-up time in a radical solution for a given radical concentration in absence of paramagnetic impurities). Let us now examine the presence of impurities in such a system.

First, the presence of paramagnetic impurity decreases the effective build-up time T_B of the radical frozen solution. Secondly, let's consider that *a priori* the paramagnetic impurity is not suited for OE, and thus the impurities relax hyperpolarization of their surroundings. As a result, both the enhancement and the build-up time of such impure radical frozen solution are smaller than without impurities. But how small?

Analogously to the model described in chapter 2, the proton spins nearby the impurity electrons relaxed by the impurities are here the target spins (their local equilibrium polarization is Boltzmann), and the spins from the OTP+BDPA volume are the source spins (their local equilibrium polarization is ε_0). Considering a $T_1 = 1$ ms for protons nearby the impurity, an impurities concentration of 2 μM, and a volume of 0.5 nm relaxed around the impurity, we can estimate:

$$\frac{W_P}{W_R} \propto \frac{V_s}{V_t}\frac{T_{1,t}}{T_{B,RS}} \approx 0.37$$

(3.2)

where $V_{s/t}$ are the source/target volumes respectively. We see in equation (3.2) that the target relaxing power is slightly bigger than the source polarizing power. As a result, the polarization in the target will not be significantly higher than 1, whereas the source polarization will be struggling reaching the local equilibrium polarization $P_{0,ON}=\varepsilon_0 P_{0,OFF}$, as shown by numerical simulations in Figure 3.7.

Since the target relaxation wins, it means that the better the communication between the source and the target, the smaller the source polarization. The communication between the source and the target is established through spin diffusion. Consequently, the higher the diffusion coefficient D, the smaller the polarization in the source. Consequently, the OTP+BDPA polarization is expected to increase with MAS, and so the enhancement (since there is no depolarization).

A more convenient way of understanding this system is by calculating the characteristic spin diffusion length ρ and compare it with the impurity's Wigner-Seitz radius. Considering an impurity concentration of 2 μM, we find that the impurity's Wigner-Seitz radius is r_{WS} = 61 nm. Following the MAS dependence of the diffusion coefficient of equation (2.9) with [^{1}H] = 3.4 M, D_0 = 2.0 10^{-4} μm^{2}s^{-1} and k = 0.6 ms, we can calculate the characteristic diffusion length for different MAS rates. We find that ρ(2kHz) = 83 nm and ρ(40kHz) = 24 nm. We see here that <u>the characteristic diffusion length is exactly in the range of the impurity's Wigner-Seitz radius</u>: ρ(40kHz) < r_{WS} < ρ(2kHz). In order to understand this process, 3 cases are presented in Figure 3.7. In Figure 3.7a, the average distance between impurity is too small to let the bulk hyperpolarization establish. On the opposite in Figure 3.7c, the average distance between impurity is too big to efficiently relax the source hyperpolarization.
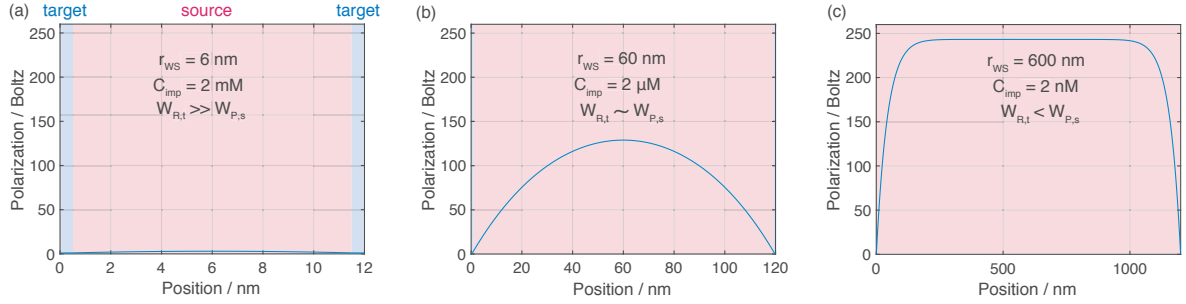

Figure 3.7: Simulated ^{1}H steady state polarization μwaves on for an impurity concentration of (a) 2 mM, (b) 2 μM, and (c) 2 nM. The volume where proton spins are relaxed by the paramagnetic impurity is shown in blue (the target), whereas the volume where protons from OTP are polarized by BDPA is shown in red (the source). The parameters taken for the simulation are shown in the following table.

parameter	L_t	L_s	D	C(^{1}H)	$T_{1,t}$	$T_{B,s}$	ε_0	ε_{depo}	v_r
value	0.5	r_{WS} (varies)	2 10^{-4}	3.4	1	73	260	1	10
unit	nm	nm	μm^{2}s^{-1}	mol.L^{-1}	ms	s			kHz

It is then possible to simulate the evolution of the polarization in such impure solutions as a function of the MAS rate, for an impurity concentration of 2 μM, as shown in Figure 3.8. A Weibull distribution of impurity separation (which is twice their Wigner-Seitz radius) was taken for this system:

$$P(r) = \frac{3}{r_{WS}} \left(\frac{r}{r_{WS}}\right)^2 e^{-\left(\frac{r}{r_{WS}}\right)^3} \tag{3.3}$$
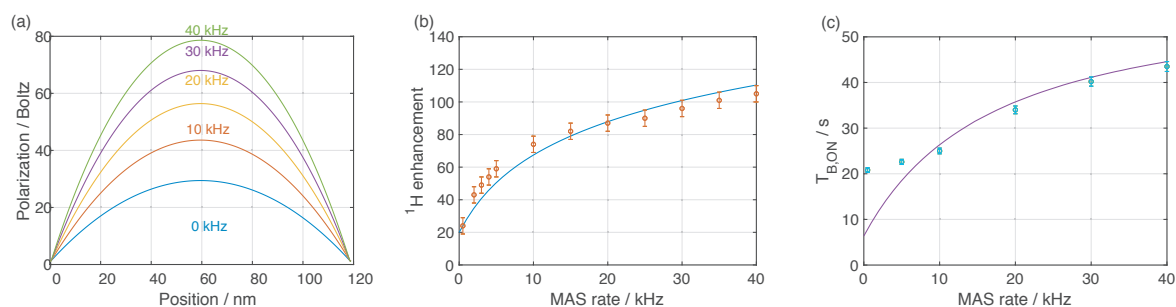
Figure 3.8: (a) Simulated ^{1}H steady state polarization μwaves on for an impurity concentration 2 μM for different MAS rate. Simulated (b) proton enhancement and (c) build-up time as a function of the MAS rate in a solution of OTP-d_{14}/OTP-H_{14} (95/5) containing 60 mM BDPA at 18.8 T and 100 K. In (b), the enhancement was measured and simulated at 15 s (not at steady state). The parameters taken for the simulation are shown in the following table. Adapted from ref 10.

parameter	L_t	L_s	k	C(^{1}H)	D_0	$T_{1,t}$	$T_{B,s}$	ε_0	ε_{depo}	v_r
value	0.5	P(r)	0.6	3.4	2 10^{-4}	1	73	260	1	varies
unit	nm	nm	ms	mol.L^{-1}	μm^{2}s^{-1}	ms	s			kHz

As shown in Figure 3.8b-c, the experimental enhancement and build-up time are well reproduced by numerical simulations. Besides, the enhancement was measured to be increasing with the recycle delay, which was also reproduced by numerical simulations.[10] We see in Figure 3.8c that the build-up time is not well reproduced for spinning rates smaller than 5 kHz, probably because the diffusion coefficient decreases between 2 and 0 kHz.[11] However overall, we think that what the model here corresponds to what we measure: a small concentration of impurities (2 μM) is relaxing less and less the bulk of the sample as the MAS rate increases due to a decreasing diffusion coefficient.

It must be noted that the phenomenon that the observed phenomenon cannot be the result of the presence of BDPA alone. The first reason is that the BDPA concentration is 60 mM leading to a r_{WS} = 1.9 nm, which is much smaller than the range of characteristic diffusion length accessible by MAS, i.e. no effect can be observed. The second reason is that a decrease of the diffusion coefficient with the MAS rate would lead to a smaller polarization transfer between BDPA and OTP, resulting in a lower enhancement as the MAS increase, which is the opposite behaviour as the one measured.

Similar behaviours were reproduced as well with trytil-nitroxide biradicals. This reasoning leads us to wonder: why didn't we ever measured such a behaviour with a radical solution of nitroxide molecules such as AMUPol in aqueous solutions? We answer this question in the next section.

3.2.2 Cross Effect vs MAS

In a radical solution of 10 mM AMUPol in glycerol-d_8/D_2O/H_2O (6/3/1), depolarization is occurring. This depolarization effect depends on MAS, but the MAS dependence of depolarization was only measured up to 10 kHz.[12] No effect can thus be predicted from such a system. Let us first examine the system if there was no depolarization.

The proton build-up time is estimated to be around $T_{B,RS}$ = 8 s without the presence of paramagnetic impurities at 100 K and 18.8 T. The characteristic diffusion length at 2 kHz is thus ρ = 26 nm and ρ = 8 nm at 40 kHz. To observe an effect on the enhancement within this range of MAS rate, the impurity's Wigner-Seitz radius would have to be around 15 nm, leading to an impurity of 0.8 mM. Such a high concentration of paramagnetic impurity seems unreasonable in glycerol-d_8/D_2O/H_2O (6/3/1), since this radical solution has been shown not to contain significant amount of oxygen[13,14] Alternatively, if the impurity concentration was identical as in the OTP/BDPA case (2 μM), we would need a diffusion rate of D = 8 10^{-3} μm^{2}s^{-1} in order to observe an effect with MAS, which is too big compared to the expected value of spin diffusion coefficient in a solid containing only 11 M of protons (see chapter 4 for more details on experimental measurements of the spin diffusion coefficient). This is why even without depolarization, the presence of paramagnetic impurities is not expected to lead to significant variations of the enhancement.

Experimental measurements were performed on the proline resonances of a sample containing 0.25 M of ^{13}C-labeled proline in glycerol-d_8/D_2O/H_2O (6/3/1) containing 10 mM AMUPol at 18.8 T and 115 K as shown in Figure 3.9.[15]
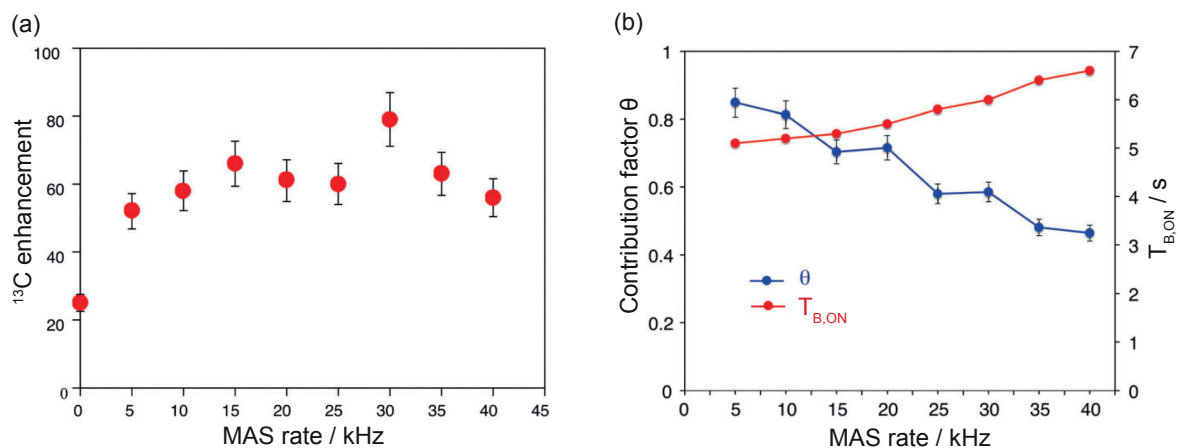

Figure 3.9: MAS frequency dependence of (a) the enhancement, (b, red) the build-up time with microwaves, and (b, blue) the contribution factor measured from ^{13}C CPMAS experiments measured on the proline resonances of a sample containing ^{13}C-labeled proline (0.25 M proline) in glycerol-d_8/D_2O/H_2O (6/3/1) containing 10 mM AMUPol at 18.8 T and 115 K. Adapted from ref 15.

In Figure 3.9a is shown show the ^{1}H enhancement measured via ^{1}H-^{13}C CP on the proline ^{13}C resonance. We notice in Figure 3.9a that the enhancement is roughly constant as a function of MAS. We know from the literature that with increasing MAS rate, the spin diffusion coefficient decreases, depolarization increases, and quenching should slightly decrease.[11,12] Since the MAS dependence of these parameters is not perfectly known, we choose here not to fit the data in Figure 3.9a to avoid overfitting. We however

point out that the signal with and without microwaves are both observed to slightly decrease at MAS rates higher than 5 kHz in the literature, which would result in a constant enhancement.[12,16]

We also notice that the µwaves on build-up time increases as the MAS rate increases. This is probably due to the fact that the spin diffusion coefficient decreases with the MAS rate (since depolarization doesn't affect the measured build-up time).

Once the behaviour of proton spins has been studied in the case of bulk frozen radical solutions, we can now use cross polarization to transfer the proton hyperpolarization to nearby low-γ nuclei.

3.3 Cross polarization and DNP

The cross polarization technique was first introduced by Pines in 1972.[17,18] This technique is used to transfer polarization from high-γ nuclei to low-γ nuclei. It consists in applying a broad band continuous radio frequency pulse in order to equalize the energy levels of the two considered nuclei. Once this is done, spontaneous transfer of polarization is occurring between the high γ (usually proton) nuclei to the low γ nucleus (usually ^{13}C, ^{15}N, ^{31}P, ^{119}Sn, ^{29}Si). This technique is used both in MAS DNP and dDNP. In this section, we show how flipping the proton magnetization back to the z-axis can enhance the sensitivity and we explain this effect using the numerical model presented in chapter 2. We also show with the numerical model that gating the microwaves in dDNP can significantly increase the polarization transfer efficiency during CP.

3.3.1 Flip-back cross polarization

This section is partially adapted with permission from Björgvinsdóttir, S.; Walder, B. J.; Pinon, A. C.; Yarava, J. R.; Emsley, L. DNP enhanced NMR with flip-back recovery *Journal of Magnetic Resonance* **2018**, *288*, 69-75.

In MAS DNP, the typical saturation recovery sequence that allows us to measure the build-up time is shown in Figure 3.10.
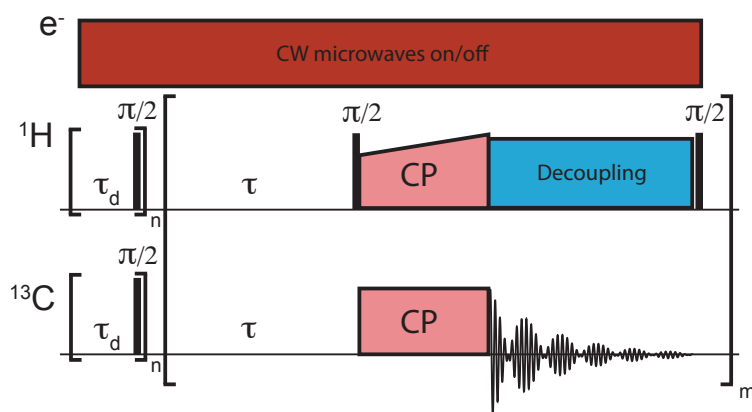

Figure 3.10: CP saturation recovery in DNP MAS with flip-back recovery. n corresponds to the number of saturation loops. m corresponds to the number of CP contacts performed during the experiment. The filp-back pulse is applied after acquisition.

However, after the acquisition, some part of the transverse magnetization can sometimes be recovered to the z axis by adding a 90° pulse as shown in Figure 3.10. We denote by f_0 the fraction of recovered proton magnetization from the flip-back pulse. With this technique, it is possible to increase the sensitivity and decrease the optimal recycle delay. Numerical simulations reproduce well the behaviour of the sensitivity as a function of the recycle delay as shown in Figure 3.11b for a solution of OTP containing 75 mM of BDPA.

In Figure 3.11a is shown the temporal evolution of the signal during several scans (each scan is 4 s) of a saturation recovery experiment for a fixed τ delay, with (blue) or without (orange) the flip-back pulse after acquisition. Without flip-back, the proton magnetization is lost after each CP pulse, whereas with

flip-back, 43% of the proton magnetization is recovered after each CP, which increases the signal intensity.
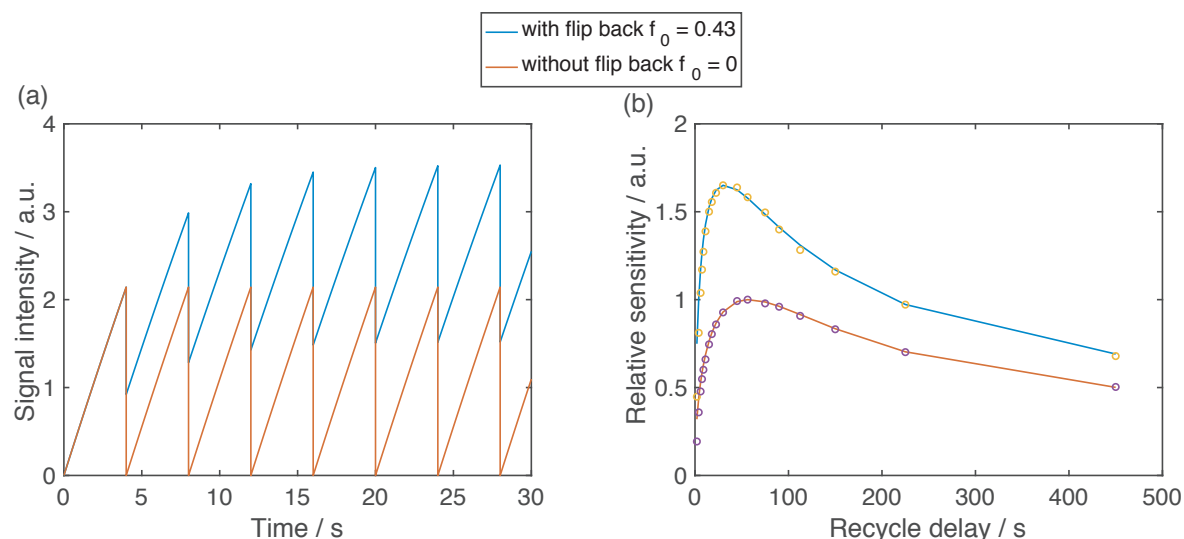

Figure 3.11: (a) Simulated signal as a function of time in a homogeneous mixture with (blue) and without (orange) flip-back recovery for a recycle delay of 4 s between CP contacts for 7 contacts (m = 7 in Figure 3.10). Relative (b) simulated (lines) and experimental (circles) ^{1}H sensitivity of a radical solution of OTP-d_{14}/OTP-H_{14} (95/5) + 75 mM BPDA at 9.4 T, 100 K and 12.5 kHz MAS rate with (blue) and without (orange) flip-back recovery. The parameters taken for the simulation are shown in the following table. Adapted from ref 19.

parameter	D	C(^{1}H)	$T_{B,RS}$	ε_0	ε_{depo}	v_r
value	$1.7\ 10^{-4}$	3.4	46	73	1	12.5
unit	$\mu m^2 s^{-1}$	mol.L^{-1}	s			kHz

In Figure 3.11a we notice that after 5 scans (20 s total time) the advantage of recovering 43% of the signal after each CP leads to a signal enhancement of about 1.6. Figure 3.11b presents the experimental (circles) and simulated (solid lines) relative sensitivity as a function of the recycle delay with and without the flip-back pulse (more details in ref 19). In Figure 3.11b we notice that the optimal recycle delay is decreased by almost 50% (going from 60 s without flip-back down to 30 s with flip-back). Such a *small* value (f_0 = 0.43) of recovered signal after CP for homogeneous mixtures is explained by the fact that the relaxation time in the rotating frame $T_{1\rho}$s are short in radical solution due to the presence of free electrons.

In cases where spins would be far away from electrons such as when organic microcrystals are impregnated with radical solutions since $T_{1\rho}$ inside the microcrystals are expected to increase, this f_0 factor would increase, resulting in a bigger enhancement of the relative sensitivity and bigger reduction of the optimal effective recycle delay.

The idea of impregnating organic microcrystal in order to polarize them by spin diffusion was introduced by Rossini *et al.*[20] in 2012. This technique will be described in more details in chapter 4 where a comprehensive explanation of polarization dynamics will be made. Here, we focus on the fact that we expect much higher f_0 in microcrystalline solids.

Microcrystals of salicylic acid were impregnated with TCE containing 16 mM TEKPol. Identical saturation recovery experiments were performed as in Figure 3.11, and results are shown in Figure 3.12.
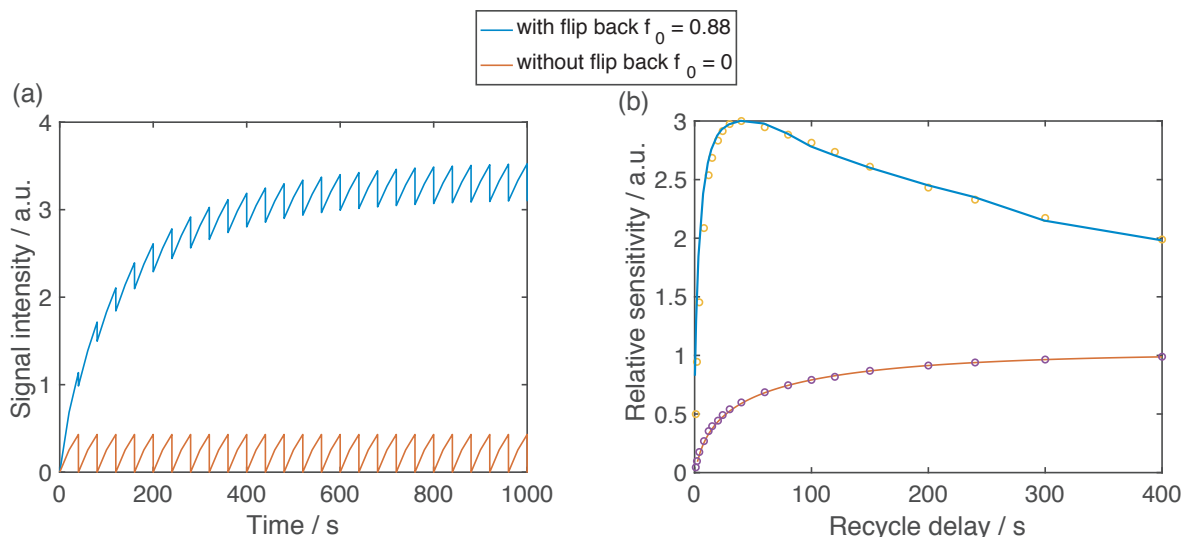

Figure 3.12: (a) Simulated signal from a microcrystal of salicylic acid as a function of time with (blue) and without (orange) flip-back recovery for a recycle delay of 40 s between CP contacts. Relative (b) simulated (lines) and experimental (plots) ^{1}H sensitivity (measured on the ^{13}C resonance lines) of a radical solution of TCE + 16 mM TEKPol impregnating microcrystalline particles of salicylic acid at 9.4 T, 100 K and 12.5 kHz MAS rate with (blue) and without (orange) flip-back recovery. The parameters taken for the simulation are shown in the following table. Adapted from ref 19.

parameter	L_t	L_s	D_s	D_t	C_s	C_t	T_1	$T_{B,s}$	ε_0	ε_{depo}	v_r	$f_{0,s}$
value	1.9	1.9	$1.7\ 10^{-4}$	$4.4\ 10^{-4}$	18	62	1	0.5	280	0.9	12.5	0.5
unit	µm	µm	$µm^2s^{-1}$	$µm^2s^{-1}$	$mol.L^{-1}$	$mol.L^{-1}$	day	s			kHz	

As expected on Figure 3.12a-b we notice that a bigger recovered fraction leads to a bigger enhancement of the relative sensitivity (here multiplied by 3) and a bigger reduction in the optimal recycle delay (here divided by 10).

We also show that type of decoupling used during signal acquisition is greatly affecting the fraction of recovered signal as shown in Figure 3.13 for the case of histidine. In previous examples, continuous wave (cw) decoupling was used during signal acquisition. Since the XiX decoupling method preserves a well-defined spin locking axis and is, in principle, amenable to proton magnetization recovery, we therefore consider the use of flip-back recovery with the XiX decoupling scheme (more details on the XiX decoupling scheme in ref 19). We see in Figure 3.13 that a modest sensitivity improvement of about 10% is possible by using XiX decoupling instead of cw. Most of the sensitivity advantage of the XiX method comes from the narrower linewidth. The figure also shows the result from flip back with XiX, where there is an improvement with respect to ordinary XiX acquisition, but it is relatively low since the f_0 factor for this experiment is estimated to be around 0.2. This highlights that preservation of magnetization under more complex decoupling than cw is difficult.
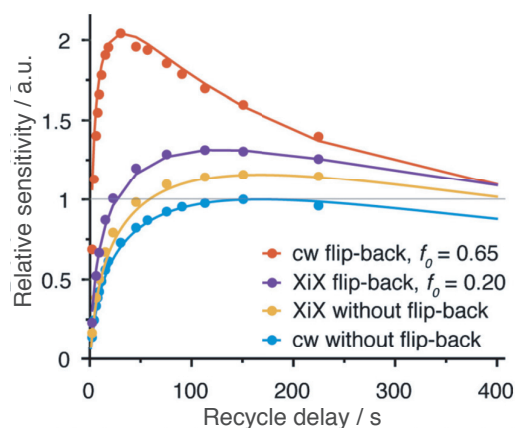
Figure 3.13: Relative simulated (lines) and experimental (disks) ^{1}H sensitivity (measured on the ^{13}C resonance lines) of a radical solution of TCE + 16 mM TEKPol impregnating microcrystalline particles histidine at 9.4 T, 100 K and 12.5 kHz MAS rate with (red & purple) and without (blue & yellow) flip-back recovery for different decoupling schemes. The parameters taken for the simulation are shown in the following table. Adapted from ref 19.

parameter	L_t	L_s	D_s	D_t	C_s	C_t	T_1	$T_{B,s}$	ε_0	ε_{depo}	θ	v_r	$f_{0,s}$
value	0.7	0.7	$1.7\ 10^{-4}$	$5.1\ 10^{-4}$	18	78	1038	0.5	280	0.5	0.5	12.5	0.5
unit	µm	µm	$µm^2s^{-1}$	$µm^2s^{-1}$	$mol.L^{-1}$	$mol.L^{-1}$	s	s				kHz	

3.3.2 Microwave gate cross polarization

This section is adapted with permission from Bornet, A.; Pinon, A. C.; Jhajharia, A.; Baudin, M.; Ji, X.; Emsley, L.; Bodenhausen, G.; Ardenkjaer-Larsen, J. H.; Jannin, S. Microwave-gated dynamic nuclear polarization *Physical Chemistry Chemical Physics* **2016**, *18*, 30530-30535.

In dDNP combined with cross polarization has allowed the transfer of polarization from highly polarized low γ nuclei, to low γ nuclei such as ^{13}C or ^{15}N. The typical CP pulse sequence is shown in Figure 3.14a. We point out here that the CP is an adiabatic CP that leaves both magnetization vectors on the z axis.
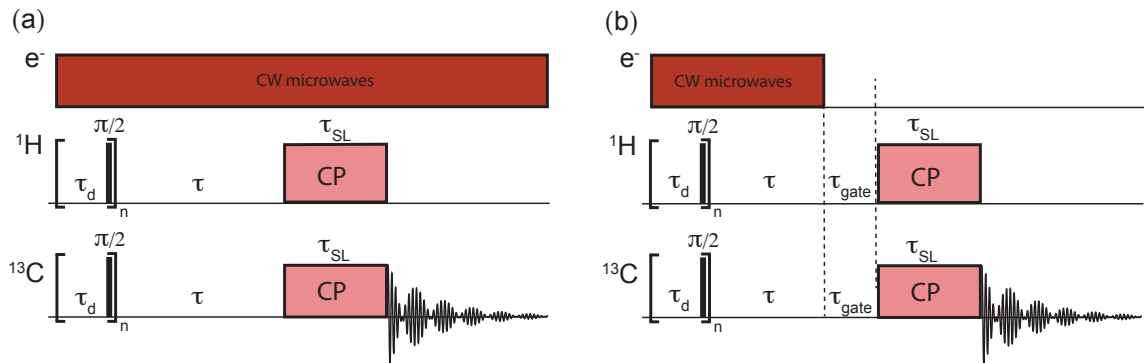

Figure 3.14: (a) CP saturation recovery in dDNP without gating. (b) CP saturation recovery in dDNP with gating.

Using the sequence presented in (a), about 50% of the proton magnetization is lost during CP. Here show that we can gate the microwaves prior to CP in order to increase the fraction of remaining proton magnetization after CP. The gating CP sequence is shown in Figure 3.14b. Finally, we even combine experimental measurements and numerical simulations in order to deduce the electronic T_{1e} of TEMPOL at 50 mM and 1.2 K.

It is interesting to look at the dynamics of the system during spin lock. Under the conditions suitable for DNP, a significant contribution to relaxation in the rotating frame is due to the presence of free electrons.[21] The relaxation time of equation (2.3) presented in chapter 2 becomes in the rotating frame:

$$\frac{1}{T_{1\rho}} = \frac{C_1}{r^6}\left(\frac{\tau}{1 + \omega_n^2\tau^2}\right) \tag{3.4}$$

where $T_{1\rho}$ is the longitudinal relaxation time in the rotating frame, τ is the electronic correlation time, C_1 a constant (C_1 is directly related to the K_1 constant described in chapter 1), and ω_n the nuclear Larmor frequency. We notice the analogy with equation (1.34) describing the spatial evolution of T_1 in the laboratory frame. However, this equation is only valid in the high temperature approximation. Indeed, at low temperatures and high fields, the electron thermal equilibrium polarization P_e^{TE} is so high that the electron flip-flop rate is attenuated from the fact that all electron spins are almost aligned in one direction. This leads to an attenuation of the relaxation rate constant as:[22]

$$\frac{1}{T_{1\rho}} = \frac{C_1}{r^6}\left(\frac{\kappa\tau}{1 + \omega_n^2(\kappa\tau)^2}\right) \tag{3.5}$$

where

$$\kappa = 1 - P_e^{\mu w} P_e^{TE} \tag{3.6}$$

where $P_e^{\mu w}$ is the partially saturated electronic polarization in the presence of microwave irradiation. We see here that the relaxation rate in the rotating frame is greatly influenced by the electronic polarization under microwave irradiation $P_e^{\mu w}$. Under MAS conditions (B = 9.4 T and T = 100 K) the electron spin polarization at thermal equilibrium is relatively low: P_e^{TE} = 6.3%, which translates into 0.996 < κ < 1, so that $T_{1\rho}$ remains essentially the same with or without electron spin saturation by microwave irradiation. However, under dDNP conditions, typically at T = 1.2 K and B = 6.7 T, the electron spin polarization at thermal equilibrium is close to unity: P_e^{TE} = 99.89%, which translates into 2.1 10^{-3} < κ < 1. Therefore, one can expect a decrease in $T_{1\rho}$ by orders of magnitude when microwave irradiation is applied to saturate the electrons.

$T_{1\rho}(^1H)$ relaxation curves were measured with a suitable pulse sequence at B = 9.4 T and T = 100 K and B = 6.7 T and T = 1.2 K with and without microwaves at 263 and 188.3 GHz respectively, in a frozen glassy sample containing 3 M [1-13C]acetate in H$_2$O/D$_2$O/glycerol-d_8 (1/4/5) doped with 40 mM TEMPOL as shown in figure 3.15. As expected, the effect of microwave irradiation on $T_{1\rho}(^1H)$ is insignificant at B = 9.4 T and T = 100 K, but is dramatic at B = 6.7 T and T = 1.2 K.
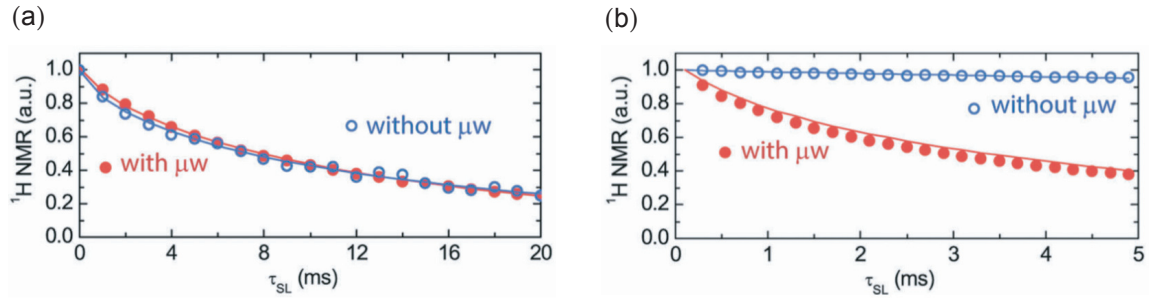
(a)

(b)

Figure 3.15: Proton $T_{1\rho}$ decay as a function of the spin lock time τ_{SL} measured at (a) B = 9.4 T and T = 100 K and (b) B = 6.7 T and T = 1.2 K in a frozen glassy sample containing 3 M [1-13C]acetate in H$_2$O:D$_2$O:glycerol-d_8 (1/4/5) doped with 40 mM TEMPOL, with (red) and without (blue) microwave irradiation (the lines are drawn to guide the eye). Adapted from ref 23.

By simulating the evolution of the polarization around an electron as a function of the electronic polarization under microwave irradiation, we can simulate the decay of the polarization as a function of time. In this case, the evolution of the polarization follows:

$$\frac{\partial P}{\partial t}(r,t) = D \cdot \Delta P(r,t) - \frac{P(r,t)}{T_{1\rho}(r)} - \beta \cdot P(r,t) \tag{3.7}$$

where β is a leakage factor that describes all source of relaxations other than paramagnetic effects due to the unpaired electron of TEMPO. Using the numerical model of polarization dynamic around an electron spin with an initial polarization being 100% and similar boundary conditions as in chapter 2, we can fit several $T_{1\rho}$ relaxation curves. We reproduce the evolution of the relaxation times as a function of the microwave power in Figure 3.16a, and as a function of temperature in Figure 3.16b. As expected in Figure 3.16a, the proton relaxation time is longer when the microwave power is smaller, since it corresponds to higher electronic polarization, thus less electronic fluctuation. Analogously in Figure

3.16b, higher temperatures lead to smaller electronic polarization, more electronic fluctuation, and shorter proton relaxation times.
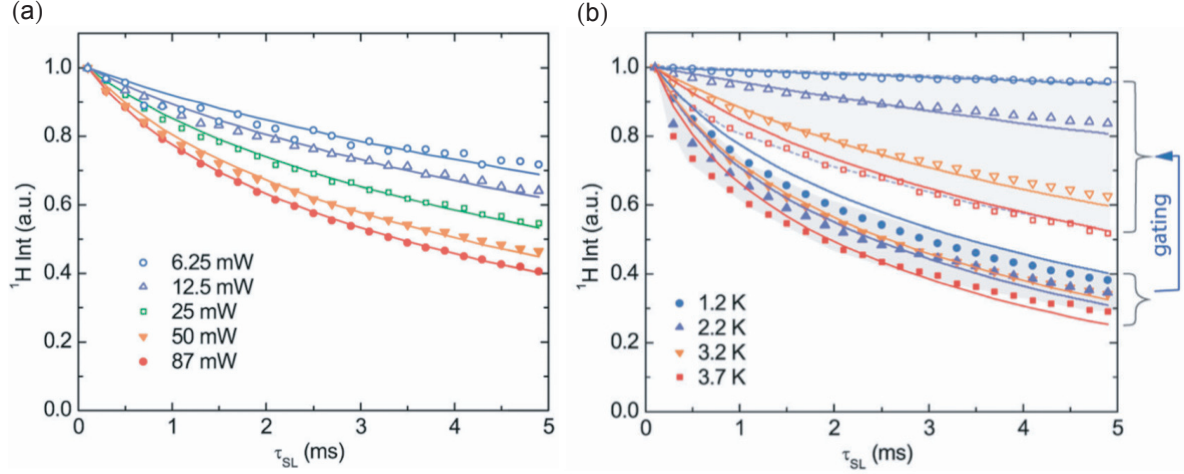
(a)   (b)

Figure 3.16: Proton $T_{1\rho}$ decay as a function of the spin lock time τ_{SL} for τ_{gate} = 500 ms measured at B = 6.7 T and T = 1.2 K in a frozen glassy sample containing 3 M [1-13C]acetate in $H_2O/D_2O/glycerol-d_8$ (1/4/5) doped with 40 mM TEMPOL, for (a) different microwave powers during τ_{gate} and (b) different temperatures. Adapted from ref[23]. Solid lines represent numerical simulations with the following parameters.

parameter	r_b	D	β	r_{WS}	C_1	τ
value	1	$1\ 10^{-6}$	8.6	2	$2.3\ 10^{-8}$	$2.8\ 10^{-4}$
unit	nm	$\mu m^2 s^{-1}$	s^{-1}	nm	$\mu m^6 s^{-1}$	s

Microwave power / mW (at 1.2 K)	6.25	12.5	25	50	87		Temperature / K (at 0 mW)	1.2	2.2	3.2	3.7
$P_e^{\mu w}$ / %	87	81	71	57	48		P_e^{TE} / %	99.8	96.9	88.7	83.9

We see from Figure 3.16 that the relaxation curves can be successfully reproduced with numerical simulations. The only factor that changes as a function of microwave power in Figure 3.16a is the electronic polarization $P_e^{\mu w}$ under microwave irradiation. In Figure 3.16b, it is the thermal equilibrium polarization P_e^{TE} that varies with temperature. We confirmed that the relaxation of proton spins during a CP spin lock is indeed due to the fluctuations of the nearby electronic spins, and that this fluctuation depends on the electronic polarization.

An interesting experiment was performed where the fraction of proton signal was measured as a function of the gating time τ_{gate}. As the gating time increases, the electronic polarization under microwave irradiation $P_e^{\mu w}$ progressively recovers towards P_e^{TE}, leading to a more and more efficient CP, and bigger fraction of proton signal measured, as shown in Figure 3.17a.
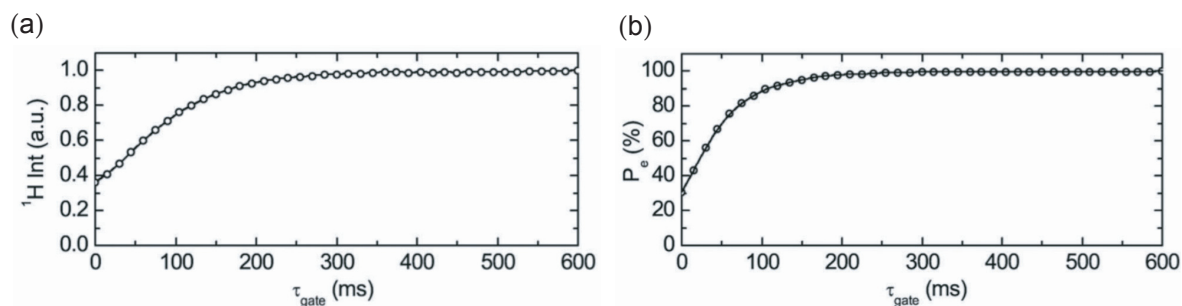
Figure 3.17: (a) Proton signal integral 3 M [1-13C]acetate in H_2O/D_2O/glycerol-d_8 (1/4/5) doped with 40 mM TEMPOL for τ_{SL} = 5 ms as a function of the gating time τ_{gate}. (b) Simulated electronic polarization as a function of the gating time. Adapted from ref 23. Solid lines are shown to guide the eye. Parameters for numerical simulations are the same as in Figure 3.16.

Experimental data shown in Figure 3.17a were fitted with numerical simulations, in order to output the electronic polarization as a function of the gating time as shown in Figure 3.17b. Fitting the build-up curve in Figure 3.17b leads to an electronic T_{1e} = 48 ms.

We see here that numerical simulations show that both $P_e^{\mu w}$ and P_e^{TE} are influent factors of the relaxation efficiency during a spin lock. Physically, it means that much less flip-flop transition that causes nuclear relaxation are possible at high electronic polarizations. This is why we notice here that gating the microwaves for 500 ms prior to CP allows the electronic polarization to recover close to unity, inhibiting nuclear relaxation during CP.

We have seen here that the CP efficiency can be increased in MAS DNP and dDNP, and that mechanisms that explain these behaviours can be successfully described with our numerical model of polarization flux.

Now that the CP is optimized, we can dissolve a target molecule in the radical solution and study its behaviour. The last section of this paragraph is focusing on the polarization dynamics of a target molecule dissolved in a homogeneous radical solution.

3.3.3 Targets dissolved in homogeneous solutions

This section shows that the build-up time and enhancement of a target dissolved in a radical solution is following the same behaviour as the radical solution itself.

A homogeneous solution of histidine dissolved in glycerol-d_8/D$_2$O/H$_2$O (6/3/1) with AMUPol as the polarization source was prepared. The prediction is that a homogeneous system displays a constant enhancement as a function of polarization time, and that the dissolved target displays the same build-up time as the solvent. As shown in Figure 3.18a, the histidine ^{13}C NMR peaks are much broader than the peaks observed when the crystalline histidine is impregnated with a radical solution remotely polarized (see chapter 4). The µwaves on build-up time is the same as the solvent build-up time as shown in Figure 3.18b, confirming that the histidine, glycerol, water, and radical molecules are homogeneously mixed. As shown in Figure 3.18c, the enhancement of both histidine and glycerol was found to be constant over 15 s, which confirms the prediction. The measurement error is relatively large for the histidine peaks because the signal-to-noise ratio was poor in the µwaves off spectra even with 2048 scans (8.5 h), due to low concentration of histidine.
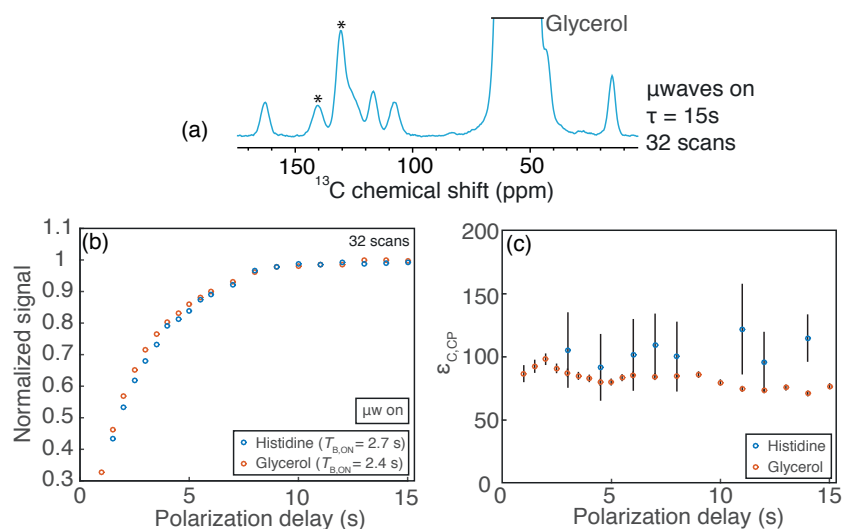

Figure 3.18: ^{13}C CPMAS DNP enhanced solid-state NMR spectrum of histidine with microwave irradiation obtained at 105 K, 8 kHz MAS, and B = 9.4 T. The asterisks indicate spinning sidebands. For spectrum (a), histidine was dissolved in 100 µL of glycerol-d_8/D$_2$O/H$_2$O (6/3/1) containing 12 mM AMUPol. (b) Normalized signal build-up with microwave irradiation of the histidine and glycerol peak areas as a function of the polarization delay and (c) the corresponding enhancement of the histidine and glycerol signals.

We confirm here that when the system is homogeneous, no heterogeneity of polarization is observed, since spin diffusion equalizes polarization almost instantaneously, leading to build-up and enhancements being identical for the source and target spins.

Now that the behaviour of homogeneous solution is well understood, it seems interesting to look at polarization dynamics in heterogeneous systems, such as impregnated microcrystals, lipid nanoparticles, core-shell particles, inorganic materials... In these heterogeneous systems, we will refer to the radical solution as "the source", and the material to be polarized as "the target".

References

(1) Zagdoun, A.; Casano, G.; Ouari, O.; Schwarzwalder, M.; Rossini, A. J.; Aussenac, F.; Yulikov, M.; Jeschke, G.; Coperet, C.; Lesage, A.; Tordo, P.; Emsley, L. Large Molecular Weight Nitroxide Biradicals Providing Efficient Dynamic Nuclear Polarization at Temperatures up to 200 K *Journal of the American Chemical Society* **2013**, *135*, 12790-12797.

(2) Sauvee, C.; Rosay, M.; Casano, G.; Aussenac, F.; Weber, R. T.; Ouari, O.; Tordo, P. Highly Efficient, Water-Soluble Polarizing Agents for Dynamic Nuclear Polarization at High Frequency *Angewandte Chemie-International Edition* **2013**, *52*, 10858-10861.

(3) Takahashi, H.; Fernandez-De-Alba, C.; Lee, D.; Maurel, V.; Gambarelli, S.; Bardet, M.; Hediger, S.; Barra, A. L.; De Paepe, G. Optimization of an absolute sensitivity in a glassy matrix during DNP-enhanced multidimensional solid-state NMR experiments *Journal of Magnetic Resonance* **2014**, *239*, 91-99.

(4) Song, C. S.; Hu, K. N.; Joo, C. G.; Swager, T. M.; Griffin, R. G. TOTAPOL: A biradical polarizing agent for dynamic nuclear polarization experiments in aqueous media *Journal of the American Chemical Society* **2006**, *128*, 11385-11390.

(5) Rossini, A. J.; Zagdoun, A.; Lelli, M.; Gajan, D.; Rascon, F.; Rosay, M.; Maas, W. E.; Coperet, C.; Lesage, A.; Emsley, L. One hundred fold overall sensitivity enhancements for Silicon-29 NMR spectroscopy of surfaces by dynamic nuclear polarization with CPMG acquisition *Chemical Science* **2012**, *3*, 108-115.

(6) Zagdoun, A.; Rossini, A. J.; Gajan, D.; Bourdolle, A.; Ouari, O.; Rosay, M.; Maas, W. E.; Tordo, P.; Lelli, M.; Emsley, L.; Lesage, A.; Coperet, C. Non-aqueous solvents for DNP surface enhanced NMR spectroscopy *Chemical Communications* **2012**, *48*, 654-656.

(7) Wenckebach, W. T. Spectral diffusion and dynamic nuclear polarization: Beyond the high temperature approximation *Journal of Magnetic Resonance* **2017**, *284*, 104-114.

(8) Perras, F. A.; Reinig, R. R.; Slowing, II; Sadow, A. D.; Pruski, M. Effects of biradical deuteration on the performance of DNP: towards better performing polarizing agents *Physical Chemistry Chemical Physics* **2016**, *18*, 65-69.

(9) Overhauser, A. W. POLARIZATION OF NUCLEI IN METALS *Phys. Rev.* **1953**, *92*, 411-415.

(10) Chaudhari, S. R.; Wisser, D.; Pinon, A. C.; Berruyer, P.; Gajan, D.; Tordo, P.; Ouari, O.; Reiter, C.; Engelke, F.; Coperet, C.; Lelli, M.; Lesage, A.; Emsley, L. Dynamic Nuclear Polarization Efficiency Increased by Very Fast Magic Angle Spinning *Journal of the American Chemical Society* **2017**, *139*, 10609-10612.

(11) Roos, M.; Micke, P.; Saalwachter, K.; Hempel, G. Moderate MAS enhances local H-1 spin exchange and spin diffusion *Journal of Magnetic Resonance* **2015**, *260*, 28-37.

(12) Mentink-Vigier, F.; Paul, S.; Lee, D.; Feintuch, A.; Hediger, S.; Vega, S.; De Paepe, G. Nuclear depolarization and absolute sensitivity in magic-angle spinning cross effect dynamic nuclear polarization *Physical Chemistry Chemical Physics* **2015**, *17*, 21824-21836.

(13) Kubicki, D. J.; Casano, G.; Schwarzwalder, M.; Abel, S.; Sauvee, C.; Ganesan, K.; Yulikov, M.; Rossini, A. J.; Jeschke, G.; Coperet, C.; Lesage, A.; Tordo, P.; Ouari, O.; Emsley, L. Rational design of dinitroxide biradicals for efficient cross-effect dynamic nuclear polarization *Chemical Science* **2016**, *7*, 550-558.

(14) Kubicki, D. J.; Rossini, A. J.; Purea, A.; Zagdoun, A.; Ouari, O.; Tordo, P.; Engelke, F.; Lesage, A.; Emsley, L. Amplifying Dynamic Nuclear Polarization of Frozen Solutions by Incorporating Dielectric Particles *Journal of the American Chemical Society* **2014**, *136*, 15711-15718.

(15) Chaudhari, S. R.; Berruyer, P.; Gajan, D.; Reiter, C.; Engelke, F.; Silverio, D. L.; Coperet, C.; Lelli, M.; Lesage, A.; Emsley, L. Dynamic nuclear polarization at 40 kHz magic angle spinning *Physical Chemistry Chemical Physics* **2016**, *18*, 10616-10622.

(16) Mentink-Vigier, F.; Akbey, U.; Oschkinat, H.; Vega, S.; Feintuch, A. Theoretical aspects of Magic Angle Spinning - Dynamic Nuclear Polarization *Journal of Magnetic Resonance* **2015**, *258*, 102-120.

(17) Hartmann, S. R.; Hahn, E. L. NUCLEAR DOUBLE RESONANCE IN ROTATING FRAME *Phys. Rev.* **1962**, *128*, 2042-&.

(18) Pines, A.; Waugh, J. S.; Gibby, M. G. PROTON-ENHANCED NUCLEAR INDUCTION SPECTROSCOPY - METHOD FOR HIGH-RESOLUTION NMR OF DILUTE SPINS IN SOLIDS *Journal of Chemical Physics* **1972**, *56*, 1776-&.

(19) Björgvinsdóttir, S.; Walder, B. J.; Pinon, A. C.; Yarava, J. R.; Emsley, L. DNP enhanced NMR with flip back recovery *Journal of Magnetic Resonance* **2018**, *288*, 69-75.

(20) Rossini, A. J.; Zagdoun, A.; Hegner, F.; Schwarzwalder, M.; Gajan, D.; Coperet, C.; Lesage, A.; Emsley, L. Dynamic Nuclear Polarization NMR Spectroscopy of Microcrystalline Solids *Journal of the American Chemical Society* **2012**, *134*, 16899-16908.

(21) Lowe, I. J.; Tse, D. NUCLEAR SPIN-LATTICE RELAXATION VIA PARAMAGNETIC CENTERS *Phys. Rev.* **1968**, *166*, 279-&.

(22) Wenckebach, W. T. *Essentials of Dynamic Nuclear Polarization*; Spindrift Publications, 2016.

(23) Bornet, A.; Pinon, A.; Jhajharia, A.; Baudin, M.; Ji, X.; Emsley, L.; Bodenhausen, G.; Ardenkjaer-Larsen, J. H.; Jannin, S. Microwave-gated dynamic nuclear polarization *Physical Chemistry Chemical Physics* **2016**, *18*, 30530-30535.

Chapter 4: Polarization dynamics
in heterogeneous systems

In the following sections, we first measure the spin diffusion coefficient in polystyrene. We then study the polarization dynamics of impregnated microcrystals and measure the size of these microcrystals using spin diffusion experiments combined with numerical simulations. More complex systems are also studied such as polymorphs, lipid nanoparticles, or core-shell particles. We finally use the numerical model to explore spin diffusion among heteronuclei in inorganic materials.

4.1 Measurement of the spin diffusion coefficient

Zhang & Cory[1] in 1998 were the first to directly measured the proton spin diffusion coefficient at room temperature in a homogeneous crystal of CaF_2 to be between 5.3 and 7.1 10^{-4} $\mu m^2 s^{-1}$. Later on, Spiess and Schmidt-Rohr measured the spin diffusion coefficient in organic polymers.[2] They found it to be between 2 and 5 10^{-4} $\mu m^2 s^{-1}$ for polystyrene at room temperature. Additionally, numbers of experiments and theoretical predictions have determined the proton spin diffusion coefficient,[3-7] always finding values in the range of 1 and 10 10^{-4} $\mu m^2 s^{-1}$. The spin diffusion coefficient has also been measured to be dependent on the MAS rate.[8] Here we propose a new, versatile approach allowing one to measure the proton spin diffusion coefficient for a wide range of materials and temperatures. The particularity of the approach here is that the measurement is performed over hundreds of nanometers, which allows use to determine a macroscopic value of the spin diffusion coefficient.

The idea is to use a heterogeneous system where part of the sample is a radical solution, and the second part is an organic particle to be polarized. Here, the key concept is that organics particle to be polarized are **well defined spherical particles of polystyrene**, as shown in Figure 4.1. Their diameter is 300 nm.
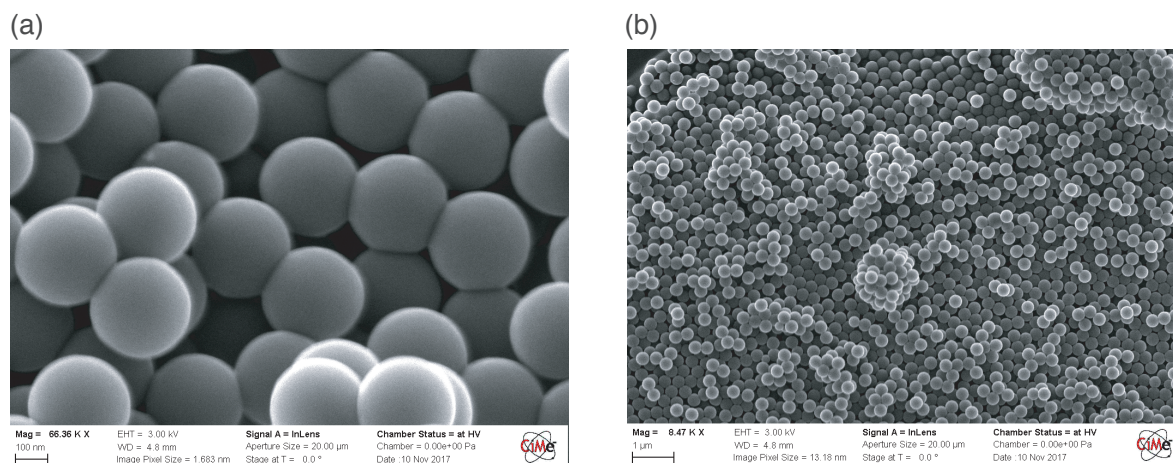
(a)　　　　　　　　　　　　　　　　(b)

Figure 4.1: SEM images of polystyrene beads of 300 nm diameter.

These particles can be impregnated with a radical solution. The impregnation technique used here is the Incipient Wetness Impregnation (IWI) introduced by Rossini *et al.* in 2012.[9] The idea is to use a non-solvent for impregnation, i.e. a solution that doesn't dissolve the solid. As a result, we obtain particles coated with the radical solution as shown in Figure 4.2. The PRE effect from radical molecules is thus happening at the exterior of the sphere, and proton spin diffusion relays this PRE to the inside of the particle. This process is called **relayed PRE,**[10] and **relayed DNP** when DNP is used. We precise here that no DNP was used, i.e. the method is applicable in any spectrometer capable of running MAS experiments.
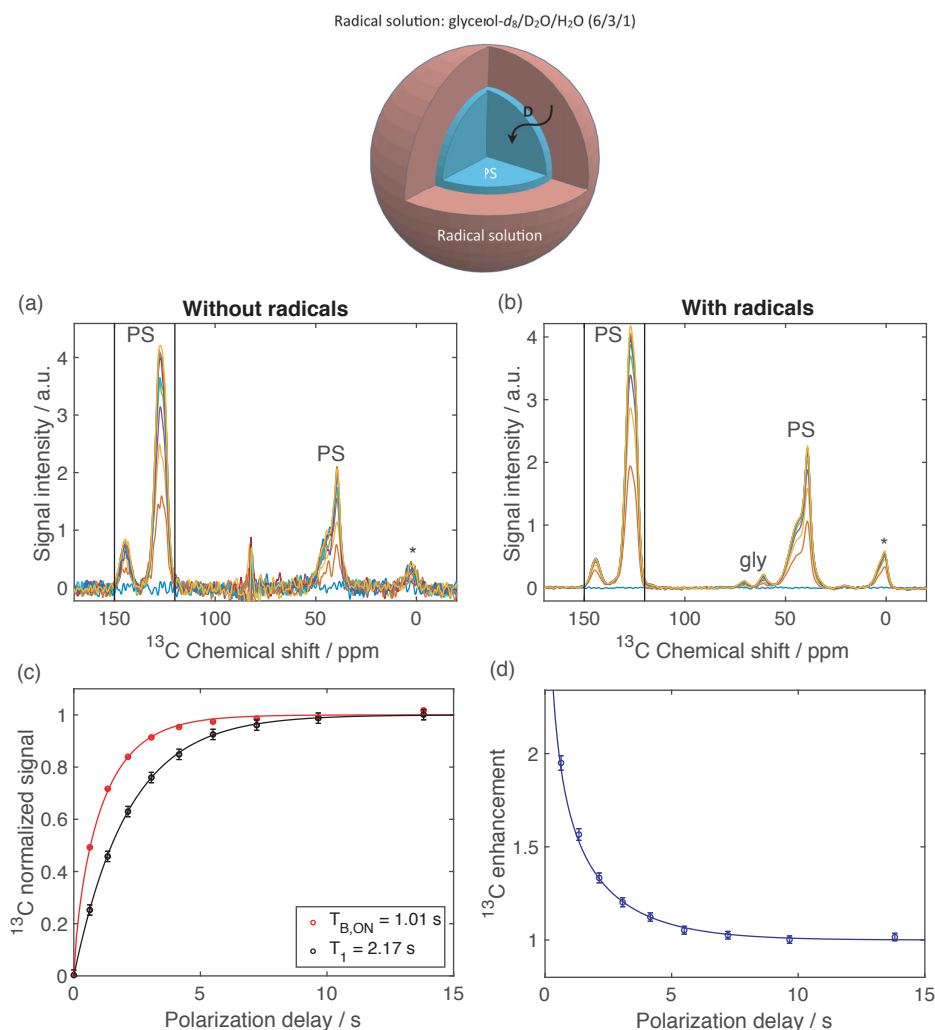
Radical solution: glycerol-d_8/D_2O/H_2O (6/3/1)

Figure 4.2: **Top**: Schematic representation of a polystyrene (PS) particle coated with a radical solution of glycerol-d_8/D_2O/H_2O (6/3/1). ^{13}C saturation recovery CPMAS spectra recorded at 9.4 T, 12.5 kHz MAS and 100 K of polystyrene particles with (a) and without (b) impregnation with the radical solution. The solid vertical lines represent the area where the signal integration was made. Each line represents a time step of the saturation recovery experiment. No microwave irradiation is used here. (c) Polystyrene normalized signal as a function of the polarization delay with (red) and without (black) impregnation. (d) Enhancement as being the ratio of the signals in (c) as a function of the polarization delay.

parameter	L_s	L_t	$T_{B,s}$	$T_{1,t}$	C_s	C_t	D_s	D_t	ε_0	ε_{depo}	v_r
value	100	300	1	2.17	18	70	$3.7\ 10^{-5}$	$5\ 10^{-4}$	1	0.5	12.5
unit	nm	nm	ms	s	mol.L^{-1}	mol.L^{-1}	µm^{2}s^{-1}	µm^{2}s^{-1}	/	/	kHz

On such a system, it is possible to monitor the evolution of the magnetization after saturation of signals, with a saturation recovery sequence as the one shown in chapter 3. With such sequence, we can observe the evolution of the polystyrene signal with time for both samples (Figure 4.2a-b). As expected, due to the PRE effect at the surface of the particle, the signal recovery is faster with the presence of the radical solution (Figure 4.2c). This system is particularly interesting, since here one of the unknown parameters is the diffusion coefficient. The particle size is known, the intrinsic relaxation time at 100 K is measured (T_1 = 2.17 s), and the build-up time at the surface of the particle can be fitted. By fitting the diffusion coefficient and the surface build-up time, we find that the best fit is found for **D = 5 10^{-4} $\mu m^2.s^{-1}$ at 100 K and 12.5 kHz MAS rate**. The best fit was found for a surface build-up time of 1 ms, which suggests the presence of radical-surface interactions as described in section 4.2.2. The measurement was repeated at 4.5 kHz spinning rate and a higher spin diffusion coefficient of D = 8 10^{-4} $\mu m^2.s^{-1}$ was obtained, confirming the fat that the diffusion coefficient decreases with the MAS spinning rate.

Similar experiments can be performed in dDNP conditions on a static sample at 1.2 K with polystyrene beads having a radius of 1.5 µm. In dDNP experiments, there is no chemical shift resolution, and signals from the radical solution and polystyrene cannot be separated. Consequently, we measure the proton build-up as a function of time. Since protons are present both in the radical solution and in the polystyrene phase, we observe a multi-exponential build-up behaviour as shown in Figure 4.3a. The fast component is due to the presence of protons in the radical solution that are affected by PRE, while the long stretched component corresponds to the range of longer build-up times from protons inside the polystyrene particle. Here for the fitting, it is important to know the volume ratio between the polystyrene volume and the radical solution volume, since the intensity of the NMR signal that we fit comes from all protons from both the polystyrene particle and the radical solution. Consequently, the thickness of the coating shell and thus the overall proton signal behaviour depends on this ratio. It can be calculated as:

$$\frac{V_{sol} \cdot \rho}{m} = \frac{(r_s + r_t)^3 - r_t{}^3}{r_t{}^3}$$

(4.1)

where r_s is the thickness of the coating layer, r_t is the radius of the spherical particle, V_{sol} the volume of radical solution used, m the mass of powder used, and ρ the density of the solid particle. In the case of non-spherical particles, BET measurements should be performed and the thickness of the coating shell can be determined as r_s = V_{sol}/(m.A) where A is the surface area of the material. Here, the signal quenching must be carefully chosen since quenching is only occurring in the radical solution and affects the overall proton signal intensity. Here since the electronic Wigner-Seitz radius is r_{WS} = 2 nm and r_q = 1.3 nm, we take θ = 0.72. When the thickness is determined, the fitting procedure can occur and the diffusion coefficient was found to be D = 7.3 10^{-4} $\mu m^2.s^{-1}$ at 1.2 K in a static sample. We confirm that the spin diffusion coefficient is higher for a static sample than for a sample spinning at 12.5 kHz.
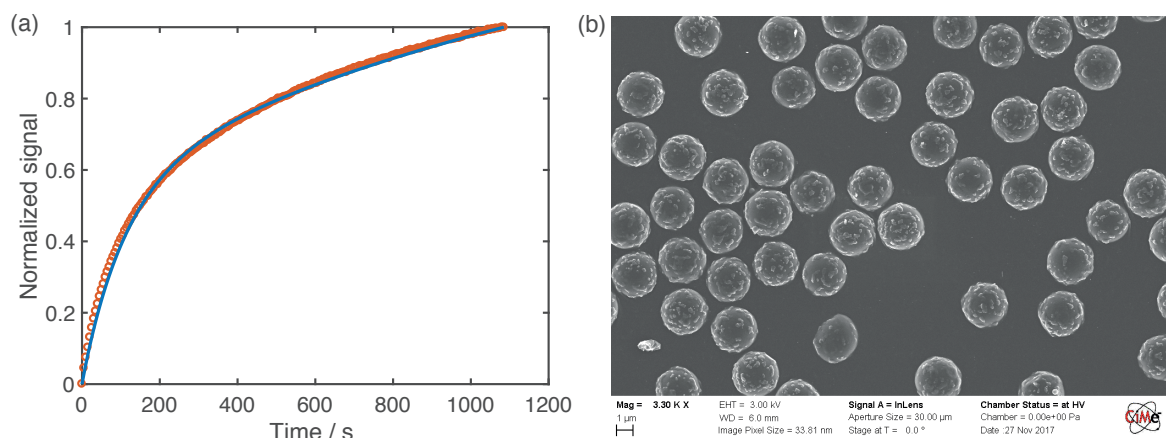
Figure 4.3: (a) Proton normalized signal area as a function of the polarization delay for particles of polystyrene impregnated with glycerol-d_8/D$_2$O/H$_2$O (6/3/1) containing 50 mM TEMPOL at 1.2 K and 6.7 T on a static sample. (b) SEM image of the polystyrene beads.

parameter	L_s	L_t	$T_{B,s}$	$T_{1,t}$	C_s	C_t	D_s	D_t	P_0	ε_{depo}	θ	ν_r
value	500	3	160	6000	11	70	$3.7\ 10^{-5}$	$5\ 10^{-4}$	90	1	0.72	0
unit	nm	µm	s	s	mol.L^{-1}	mol.L^{-1}	µm^{2}s^{-1}	µm^{2}s^{-1}	%	/	/	kHz

It must be noted that these measurements were performed on amorphous solids. It must be kept in mind that the spin diffusion coefficient can vary in the case of a monocrystal or powder (i.e. polycrystalline solid). **This spin diffusion coefficient is a reference value**. This value can now be scaled with $\gamma^2 C^{1/3}$ as mentioned in chapter 1 for different proton concentrations and different nuclei.

Now that the spin diffusion coefficient is known, we can turn the problem the other way around: can we determine domain sizes via relayed DNP when the spin diffusion coefficient is known? We will address this question in the next section.

4.2 Polarization of organic microcrystals

This section is adapted with permission from the publication: Pinon, A. C.; Schlagnitweit, J.; Berruyer, P.; Rossini, A. J.; Lelli, M.; Socie, E.; Tang, M. X.; Pham, T.; Lesage, A.; Schantz, S.; Emsley, L. *Measuring Nano-to Microstructures from Relayed Dynamic Nuclear Polarization NMR J. Phys. Chem. C* **2017**, *121*, 15993-16005.

To confirm predictions of numerical simulations made in chapter 2 that signal build-up times depend on the size of the target in heterogeneous samples, ^{13}C detected ^{1}H build-up times of histidine signals were measured when the histidine solid was either dissolved in a radical containing solution (Figure 4.4, purple circles), ground and impregnated with a solution (Figure 4.4, blue circles), unground and impregnated (Figure 4.4, orange circles), and for the dry powder alone (Figure 4.4, grey circles).

As shown in Figure 4.4, the build-up time clearly increases with the size of the particle, ranging for the μwaves on case from 2.7 s for the homogeneous solution to 435 s when the size of the particles is large, up to 1038 s for the dry powder which corresponds to the intrinsic T_1 of crystalline histidine. As predicted from numerical simulations (Figure 2.6a-b) for heterogeneous systems, shorter build-up times are measured for μwaves on than for μwaves off for the impregnated powders. We also notice that the build-up time is always equal or shorter in the μwaves on than in the μwaves off case, due to a bigger polarization gradient in the μwaves on case.
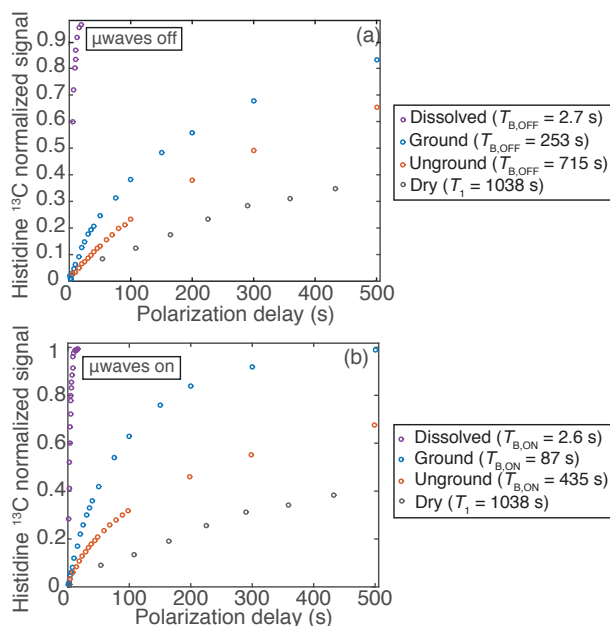

Figure 4.4: Signal ^{1}H build-up curves detected through the signal of the ^{13}C resonance in CPMAS NMR spectra recorded at 105 K, 8 kHz MAS, and B = 9.4 T (a) without and (b) with microwave irradiation of either dry, ground, unground, or dissolved powders of crystalline histidine. The dissolved sample was in glycerol-d_8/D$_2$O/H$_2$O (6/3/1) with 12 mM AMUPol. The impregnation was done with 1,1,2,2-tetrachloroethane (TCE) containing 16 mM TEKPol. All signals were normalized using the steady-state value from the exponential fits. Adapted from ref 11.

Now it is time to measure the size of particles of histidine impregnated with a radical solution via relayed DNP. Figure 4.5 shows the DNP enhanced spectrum from a sample of unground microcrystalline histidine

impregnated with TCE containing 16 mM of TEKPol. Each slice corresponds to each spectrum at a given polarization delay of the saturation recovery experiment. We notice that the histidine ^{13}C NMR peaks in this heterogeneous sample are much narrower than those in the homogeneous solution of chapter 3, because the organic domains now remain crystalline. The build-up of the histidine peaks with and without microwave irradiation is shown in Figure 4.5c and the enhancement as a function of the polarization delay is shown in Figure 4.5d. We then fit both the signal build-up and the enhancement with numerical simulations. **We find the best fit between experiments and simulations for spherical domains of radius of 5.5 μm** (see figure caption for the other parameters). The same system was also studied by DNP with manually ground particles (i.e. where smaller particles are expected), and a 2.3 μm average particle radius was determined, in agreement with SEM images.[11]
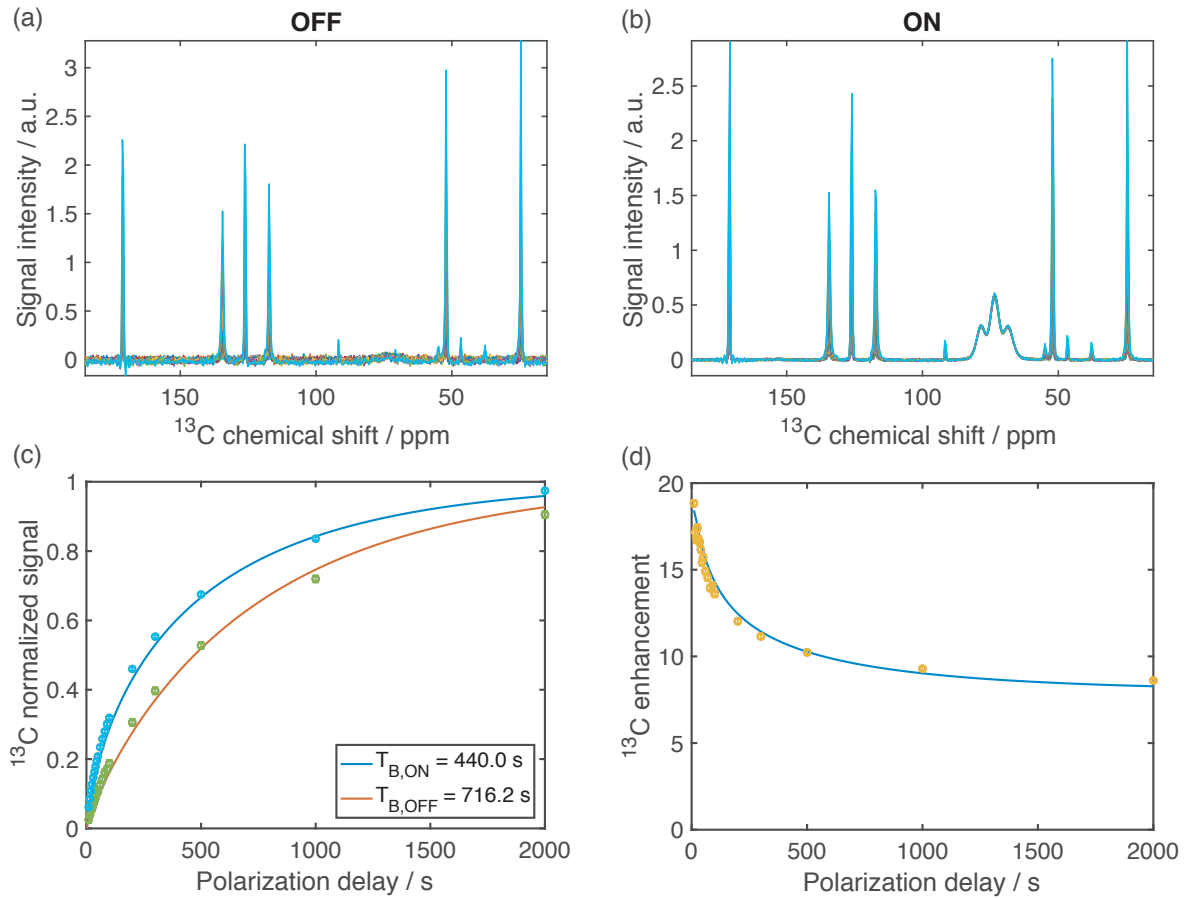

Figure 4.5: [13]C CPMAS DNP enhanced solid-state NMR spectra obtained at 100 K, B = 9.4 T and 8 kHz MAS of microcrystalline unground histidine impregnated with a solution of TCE containing 16 mM TEKPol (a) without and (b) with microwave irradiation. (c) Signal build-up of histidine peaks with and without microwave irradiation as a function of the polarization delay. (d) ^{13}C CP DNP enhancement of histidine peaks as a function of the polarization delay. Adapted from ref [11]. In (c) and (d), numerical simulations are overlapped using the following parameters.

parameter	L_s	L_t	$T_{B,s}$	$T_{1,t}$	C_s	C_t	D_s	D_t	ε_0	ε_{depo}	v_r
value	1	5.5	3	1038	18	78	$3.7\ 10^{-5}$	$6.5\ 10^{-4}$	30	0.5	8
unit	μm	μm	s	s	mol.L^{-1}	mol.L^{-1}	μm^{2}s^{-1}	μm^{2}s^{-1}	/	/	kHz

We notice here that the polarizing power of the radical solution which is proportional to $C_s/T_B = 6$ is higher than the relaxing power of histidine $C_t/T_1 = 0.07$. This is why a significant enhancement can be measured inside the particle. This is thanks to a weak histidine relaxation time ($T_1 = 1038$ s). But for particle having much shorter T_1s such as polystyrene ($T_1 = 2.17$ s), **it might be necessary to adjust the proton concentration in the radical solution in order to maximize the enhancement inside the particle**.

4.2.1 Optimization of the radical solution

If the goal of the experiment is to determine sizes as we just did, one usually wants to have the characteristic diffusion length on the order of the size of the target, so that the size of the target can be precisely measured. Also, if one wants to measure the µm range, relayed DNP might me the best technique to use (Figure 4.5). However, if one wants to measure the nm range, relayed PRE might be more suited (Figure 4.2). As usual, it depends on the intrinsic relaxation time T_1 of the solid to probe.

But when the goal is to maximize the polarization inside the target, the radical solution enhancement is not the quantity to be maximized. Indeed, as we mentioned in chapter 2, the magnetic energy that the radical solution can provide per unit of time is an important factor to be taken into account. In such cases, the proton concentration in the radical solution has a significant impact on how well the radical solution can polarize the particle. The total number of protons in the radical solution can be changed by either varying the thickness of the coating shell Δ, or by varying the proton concentration [^{1}H]. Both cases are qualitatively simulated in Figure 4.6a.
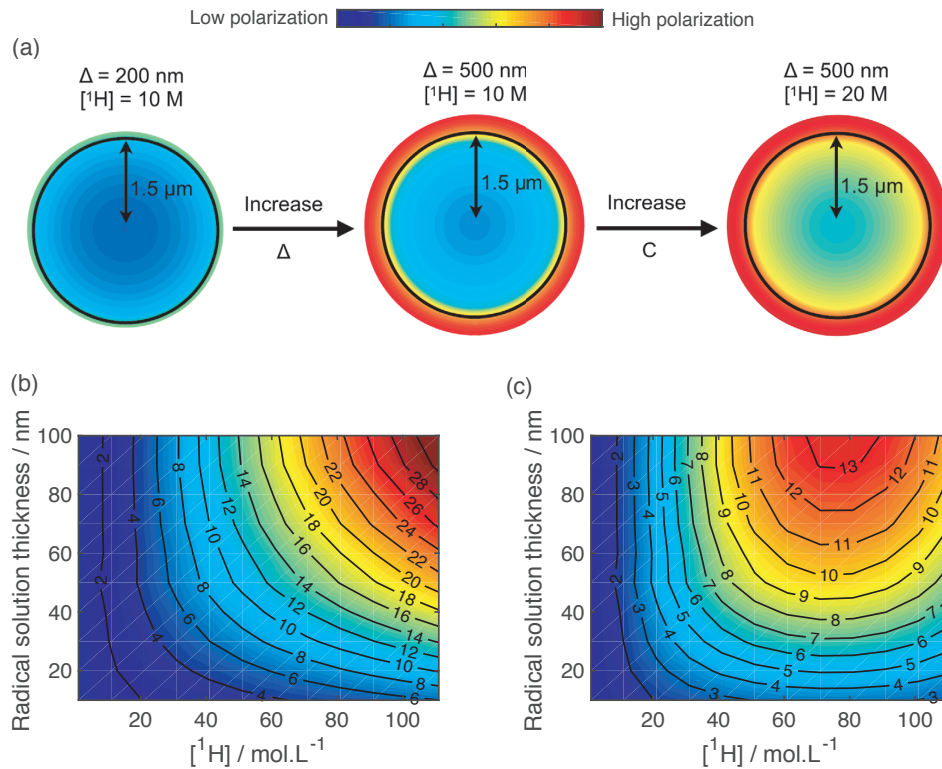

Figure 4.6: (a) Simulated polarization inside and outside a spherical microcrystal of a fixed size, for different radical solution thicknesses and different proton concentrations in the radical solution. Enhancement in a particle as a function of the radical solution thickness and proton concentration without (b) or with (c) taking into account the fact that both the radical solution build-up time and enhancement depend on the proton concentration. Parameters used for panels (b) and (c) are shown in the following table. For panel (c), the enhancement and build-up times were taken to follow the behaviour in Figure 3.6b-c.

parameter	L_s	L_t	$T_{B,s}$	$T_{1,t}$	C_s	C_t	D_s	D_t	ε_0	ε_{depo}	v_r
value	varies	100	17 or varies	2.15	varies	70	varies	$5\ 10^{-4}$	255 or varies	0.5	12.5
unit	/	nm	s	s	mol.L^{-1}	mol.L^{-1}	µm^{2}s^{-1}	µm^{2}s^{-1}	/	/	kHz

We see in Figure 4.6a that increasing the thickness of the proton concentration increase the polarization (and thus the enhancement) inside the particle. In Figure 4.6b is shown the steady state enhancement inside a particle as a function of the radical solution thickness and the proton concentration of the radical solution **if the radical solution enhancement and build-up times were independent of the proton concentration**. As expected, we observe that increasing either of the proton concentration or the radical solution thickness increases the enhancement inside the particle.

But one thing that must be added to this simulation to be more realistic is the fact that **both the build-up time and the steady state enhancement of the radical solution do depend on the proton concentration at 100 K, as shown in chapter 3**. The enhancement decreases with the proton concentration, and the build-up time decreases with the proton concentration at 100 K, as measured in chapter 3. When taking these effects into account, we can plot again the steady state enhancement inside the particle in Figure 4.6c. We now observe that higher proton concentrations than 80 M are unfavourable for the particle enhancement, since it corresponds to cases where the radical solution enhancement itself is becoming too small. These effects must be taken into account if one wants to maximize the polarization inside microcrystals: **the highest enhancement in the radical solution is not predicted to lead to the highest enhancement in the particle**.

In order to confirm this prediction, we measured the solvent enhancement (glycerol ^{13}C resonance) and the polystyrene enhancement of a sample containing polystyrene particles of 100 nm diamater impregnated with glycerol-d_8/glycerol-H_8/D$_2$O/H$_2$O and 2 mM AMUPol. The enhancements can be successfully reproduced with numerical simulations as shown in Figure 4.7b. The same measurement was also performed at different proton and radical concentrations as shown in Table 4.1. The same ratio solid/liquid was used, in order to create the same radical solution layer thickness around the polystyrene particle.
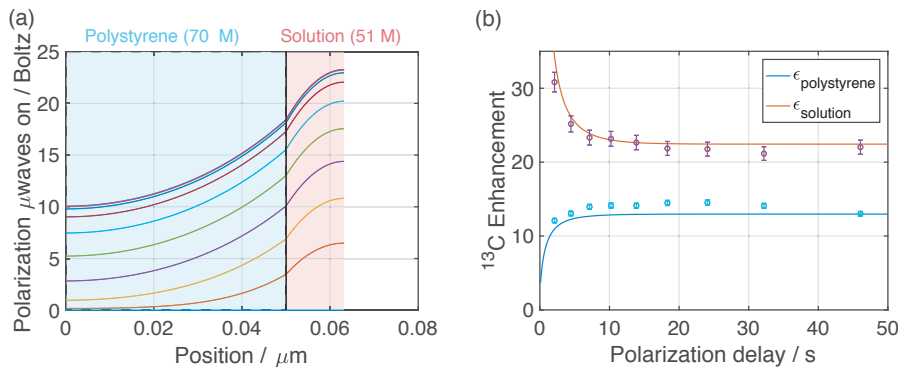

Figure 4.7: (a) Simulated polarization inside and outside a spherical microcrystal having a 50 nm radius, for a proton concentration in the radical solution of 51 M. (b) Experimental and simulated ^{13}C enhancements as a function of polarization delay of a sample containing polystyrene particles of 100 nm large impregnated with glycerol-d_8/glycerol-H_8/D$_2$O/H$_2$O and 2 mM AMUPol at 100 K, 9.4 T and 12.5 kHz MAS rate. The parameters for numerical simulations are shown in the following table.

parameter	L_s	L_t	$T_{B,s}$	$T_{1,t}$	C_s	C_t	D_s	D_t	ϵ_0	ϵ_{depo}	ν_r
value	13	100	14.4	2.15	51	70	3.2 10^{-4}	5 10^{-4}	590	0.5	12.5
unit	nm	nm	s	s	mol.L^{-1}	mol.L^{-1}	µm^{2}s^{-1}	µm^{2}s^{-1}	/	/	kHz

In Figure 4.7b we see for the first time that the radical solution's enhancement can vary with time. It happens in cases where the thickness of the coating radical solution layer is smaller than the radical solution's characteristic diffusion length, as it is the case here (Figure 4.7a).

Table 4.1: Experimental measurements for polystyrene beads of 100 nm diameter impregnated with glycerol-d_8/glycerol-H_8/D$_2$O/H$_2$O and AMUPol for different radical and proton concentration.

[AMUPol] / mM	[^{1}H] / M	T_B / s	ε_{RS} @ 10 s	$\varepsilon_{RS}.W_P$ / mW.L^{-1}	ε_{PS} @ 10 s
2	3.5	28	240	29	9
2	51	14	183	655	14
12	14	2.5	241	1349	19
12	109	3.2	166	5654	38

We see on Table 4.1 that at low (2mM) and high (12mM) AMUPol concentrations, the enhancement of a radical solution **alone** (ε_{RS}) is **higher** at **low** proton concentration but when this solution is impregnating particles, the enhancement inside the particle (ε_{PS}) is **higher** at **high** solution proton concentration. This confirms our observation from numerical simulations: **in order to increase the enhancement in organic particles, increasing the radical solution enhancement is not necessarily the way to go. Notably, the commonly used "DNP juice" containing 11 M of protons and 12mM of AMUPol is <u>not optimal</u> for polarizing highly protonated particles like polystyrene. One must aim for higher proton concentrations, even if sometimes it means lower radical solution enhancement.**

However, here we define $\varepsilon_{RS}.W_P$ as the product of the enhancement and the radical solution polarizing power by considering the same importance to the radical solution enhancement, to its proton concentration, and to its build-up time (W_P is a simple ratio of these parameters). In reality the importance of each of these parameters might change. Besides, the solution polarizing power does not take into account the spin diffusion coefficient, neither the intrinsic relaxation time in the particle. As we can see in Figure 4.8 where experimental proton enhancement (orange) and enhancement times polarizing power (blue) of a sample of glycerol-d_8/glycerol-H_8/D$_2$O/H$_2$O at 109 M proton concentration as a function of the AMUPol concentration was measured, we see that $\varepsilon_{RS}.W_P$ is maximized for 100 mM of AMUPol whereas the enhancement is only 31. If maximizing $\varepsilon_{RS}.W_P$ would mean maximize ε_{PS}, it would mean that the polystyrene enhancement would be higher at an AMUPol concentration of 100 mM than 12 mM, whereas the polystyrene enhancement is already 38 at 12 mM... This doesn't make sense.
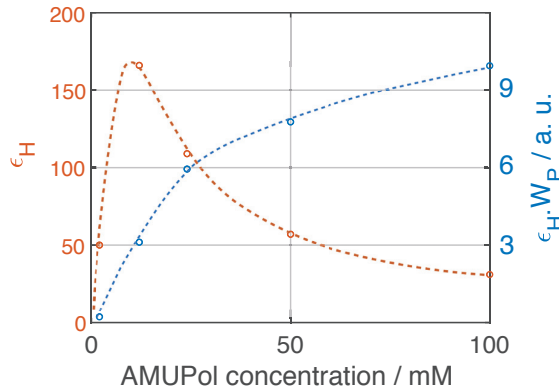

Figure 4.8: Experimental proton enhancement (orange) and enhancement times polarizing power (blue) of a sample of glycerol-d_8/glycerol-H_8/D$_2$O/H$_2$O at 109 M proton concentration, as a function of the AMUPol concentration.

We come to the conclusion that a new number that describe the source/target system must be found for heterogeneous systems. This number must give the scientist a good idea of if the system is optimized for

maximizing the enhancement inside a microcrystal or not. We thus define the following number expressed in watts:

$$\Pi = \frac{D_{eff} \cdot T_{1,eff} \cdot \varepsilon_H{}^2}{A \cdot T_B} \left(\frac{N_{H,s}}{N_{H,t}}\right)\left(\frac{C_p}{N_A}\right) \tag{4.2}$$

where T_B is the build-up time of the radical solution, A the surface area of the material, C_p the spin capacity of the spins, N_A Avogadro's number, $N_{H,s/t}$ number of protons in the source/target, ε_H the radical solution proton enhancement, and

$$D_{eff}{}^{-1} = D_{source}{}^{-1} + D_{target}{}^{-1} \tag{4.3}$$

$$T_{1,eff}{}^{-1} = T_{1,source}{}^{-1} + T_{1,target}{}^{-1} \tag{4.4}$$

This number shows a high correlation with the predicted enhancements from numerical simulations, as a shown by comparing Figure 4.9 and Figure 4.6c. As predicted by Π, proton concentrations higher than 70 M are unfavourable for the polarization of microcrystals. **It means that if one wants to maximize the polarization in microcrystals, one can calculate Π and try to maximize it.**
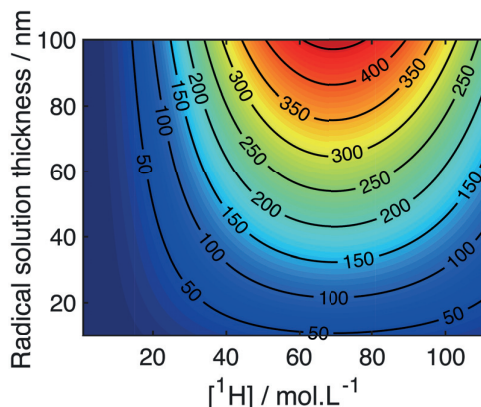

Figure 4.9: Π number that describes the steady state polarization of a particle as a function of the proton concentration in the radical solution. Parameters used for the simulations are identical as in Figure 4.6c.

Ideally, equation (2.26) that describes the steady state enhancement inside a spherical particle could be used in order to optimize the system instead of Π. But equation (2.26) is rather complex and we want to use simple number here so that the work presented in this thesis is useful for any scientist. The Π number is relatively simple to calculate and very convenient for predictions. A final alternative is simply to open the webpage http://msd.epfl.ch/home where we created a user-friendly interface allowing anybody to predict if their system is suited for hyperpolarization of organic materials.

The system source/target might get more complex than what we think. Indeed, the radical molecule could interact with the surface of the particle. We study these interesting surface effects in the next section.

4.2.2 Surface effects

One effect recently observed by Perras *et al.*[12] was that the importance of radical-surface interactions are often neglected. Indeed, they show that the optimal radical concentration when the radical solution is impregnating a material can greatly vary depending on if the material has preferential interactions with the radical molecules or not. Similar measurements were thus performed at EPFL on microcrystalline solids.

When histidine particles are impregnated with TCE containing TEKPol, in order to understand if whether or not TEKPol molecules are interacting with the surface of histidine particles, the following measurements was performed: the proton enhancement of histidine was measured as a function of the TEKPol concentration in a solution of TCE-d_2. It means that the proton enhancement measured on histidine *is only generated from the TEKPol molecules in close proximity to the surface* that polarize histidine protons from direct cross-effect. As shown in Figure 4.10b, the TEKPol concentration for which the histidine enhancement is the highest is occurring at lower TEKPol concentrations (10 mM) than the optimal radical concentration for a bulk radical solution alone (16 mM).[13] In chapter 2, we assumed that the particle steady enhancement was not supposed to be a function of the build-up time in the radical solution. This is only true when the particle enhancement is the result of the polarizing power of the bulk protons in the radical solution. Here we measure different enhancement since we only measure the enhancement from direct cross effect.

This observation leads us to think that **the concentration of radical molecules is higher at the surface of the particle than in the bulk of the radical solution**. We just postulated here that histidine is a *TEKPophillic* solid: there is more TEKPol molecules at the surface of the histidine particle than in the bulk of the radical solution. In order to confirm this hypothesis, we measured the histidine enhancement as a function of time for each of these radical concentration. We see in Figure 4.10a that **the early behaviour of the enhancement strongly depends on the radical concentration, as predicted by numerical simulations in chapter 2.**
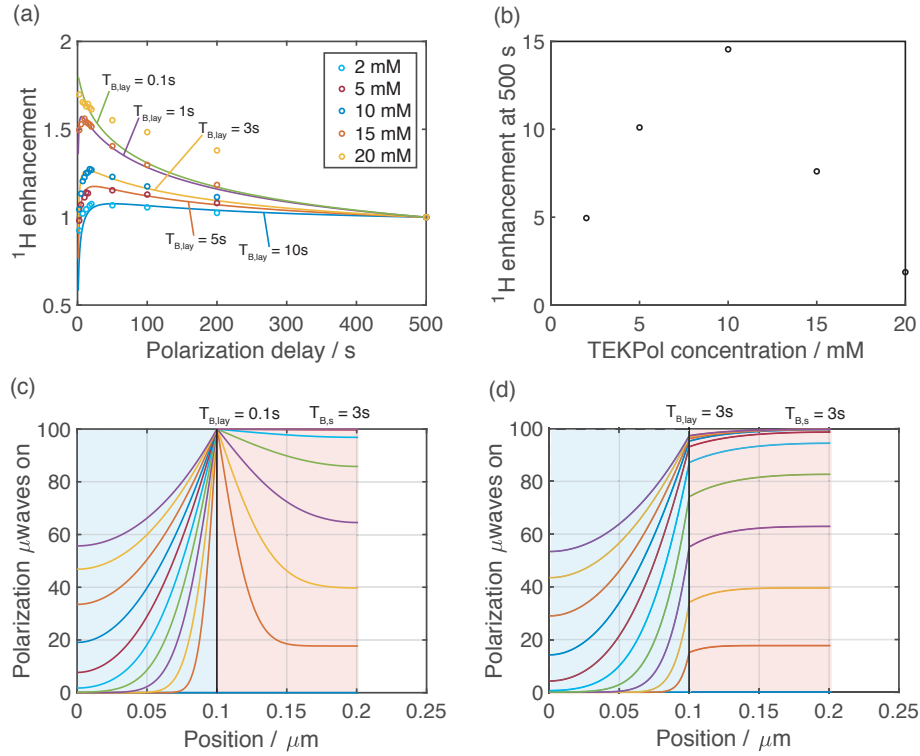
Figure 4.10: (a) Experimental normalized proton enhancement of histidine microcrystal measured at 9.4 T, 12.5 kHz MAS rate, and 100 K as a function of the polarization delay. Overlapped (solid lines) are numerical simulations for different build-up times at the surface of the particle $T_{B,lay}$ (i.e. corresponding to different radical concentration at the surface of the particle). (b) Proton enhancement at 500 s recycle delay as a function of the radical concentration. Simulated polarization as a function of position in the source (red) + target (blue) system for exponential time steps with (c) and without (d) the presence of a short T_B at the layer representing the presence of high radical concentration at the source/target border. The parameters used for the simulations are shown in the following table.

parameter	L_s	L_t	$T_{B,s}$	$T_{1,t}$	C_s	C_t	D_s	D_t	ε_0	ε_{depo}	v_r
value	0.1	2-4	0.1 - 10	1038	18	78	$3.7\ 10^{-5}$	$8.1\ 10^{-5}$	20	0.5	12.5
unit	μm	μm	s	s	mol.L^{-1}	mol.L^{-1}	μm^{2}s^{-1}	μm^{2}s^{-1}	/	/	kHz

Numerical simulations are then modified in order to take into account this surface effect. We add to the model a layer between the source and the target where the T_1 is reduced due to the high radical concentration. This layer was set to be 1 nm large, building-up to the same enhancement as in the bulk of the radical solution, with a shorter build-up time $T_{B,lay}$. The case with such a layer is presented in Figure 4.10c and without such a layer in the panel (d). We see in Figure 4.10a that numerical simulations that take into account this short surface build-up time successfully reproduce the enhancement's early behaviour, confirming that the build-up time at the surface of the particle determines the enhancement behaviour at early times.

This observation explains why numerical simulations predict an increasing enhancement at early times when not considering the layer (Figure 2.4d), whereas experiments show a decreasing enhancement:[11] the radical layer must be added to the simulations in these cases, as done in Figure 4.10c. To confirm (again) this hypothesis, we can have a look at the enhancement behaviour in a system when the source and target are no longer physically two different solids (i.e. no surface effect possible), but rather the

same solid where the source/target interface only defined by the presence or absence of radical molecules, as shown in Figure 4.11.
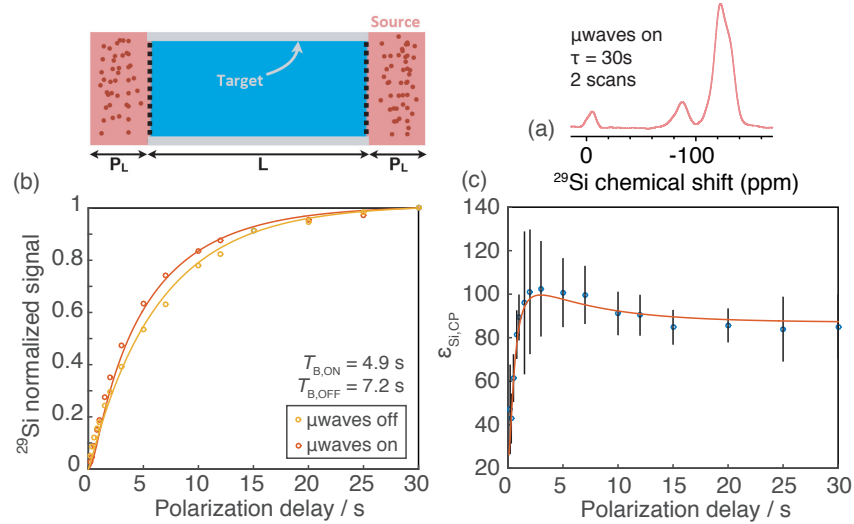

Figure 4.11: ^{29}Si CPMAS DNP enhanced solid-state NMR spectra obtained at 105 K, B = 9.4 T, and 8 kHz MAS of the mesoporous material MatImPh-dTMS impregnated with TCE containing 16 mM biradical TEKPol2. (b) ^{29}Si CPMAS normalized signal build-up of the silicon resonance with and without microwave irradiations. The signals were normalized to that of the longest polarization delay. (c) ^{29}Si CP DNP enhancement of the ^{29}Si signal as a function of the polarization delay. Adapted from ref [11]. In panels (b) and (c), numerical simulations are overlaid for one- dimensional diffusion with the following parameters.

parameter	L_s	L_t	$T_{B,s}$	$T_{1,t}$	C_s	C_t	D_s	D_t	ε_0	ε_{depo}	v_r
value	0.2	0.6	1	10	18	18	$3.7\ 10^{-5}$	$3.7\ 10^{-5}$	390	0.5	12.5
unit	μm	μm	s	s	mol.L^{-1}	mol.L^{-1}	μm^{2}s^{-1}	μm^{2}s^{-1}	/	/	kHz

When impregnating silica-based mesoporous materials with a radical solution (TCE) containing a bulky radical (here TEKPol2[14]), the enhancement of the silicon atoms of the material are shown to depend on time (Figure 4.11c). This shows that the TCE solution can penetrate the inside of the pores, whereas the bulky radical is restricted outside the pores. Here the interface source/target is no longer precisely defined as two different solids, but rather by the presence or absence or radical molecules. We cannot define here any radical interaction at the source/target border, and we see in Figure 4.11c that the enhancement behaviour at early times is different from previously: the early behaviour shows an increase followed by a decrease, in contrast with the decreasing behaviour measure in Figure 4.5d. The experimental enhancement is reproduced with numerical simulation using a build-up time of 1 s in the radical solution (corresponding to experimental measurement) without using any layer between the source and the target, which shows here that no surface effect is observed.

Now that the model has proved its strength for simple biphasic systems, more complex systems can be studied by relayed DNP, such as layer systems.

4.3 Layer systems

In this section, we combine saturation recovery experiments with numerical simulations in order to determine the structure of layer systems. We prove the robustness of the method by determining the thickness of different layers in polymorphic drugs, lipid nanoparticles, crystalline nanoparticles, and core-shell nanoparticles.

4.3.1 Polymorphs of Theophylline

This section is adapted with permission from Pinon, A. C.; Rossini, A. J.; Widdifield, C. M.; Gajan, D.; Emsley, L. Polymorphs of Theophylline Characterized by DNP Enhanced Solid-State NMR *Molecular Pharmaceutics* **2015**, *12*, 4146-4153.

Here we want to use relayed DNP to the polymorphic drug theophylline. Theophylline is known to crystallize as several different polymorphs. The kinetically stable of theophylline under typical lab conditions is often referred as Form II and is usually the form obtained from commercial suppliers. The monohydrated form (Form M) of theophylline is obtained by a simple recrystallization of Form II in water.[15]

We want to use relayed DNP on Form M (Figure 4.12Aa) of theophylline particles by impregnating them with a radical solution. In order to use the impregnation technique on theophylline, it is first necessary to grind the powder. But grinding Form M at room temperature causes dehydration of the sample and partial reconversion to Form II, as shown in Figure 4.12Ab.

To potentially avoid this, the powder was ground in the presence of several drops of distilled water, to prevent dehydration. This technique worked well, as shown in the resulting ^{13}C CPMAS NMR spectrum in Figure 4.12Ac. When the ground powder of Form M was impregnated with TCE/methanol (95/5), partial conversion of Form M to Form II was observed (Figure 4.12Ad). However, impregnation with a glycerol-d_8/D$_2$O/H$_2$O (6/3/1) solution did not cause any measurable transformation to Form II, as shown in Figure 4.12Ae.

In Figure 4.12B is shown the ^{13}C CPMAS spectra of form M ground (without water) and impregnated with TCE/methanol (95/5). As expected, partial polymorphic transition from Form M to Form II is occurring. But the interesting phenomenon here is that since Form M and Form II have different chemical shift, it is possible to measure separately different enhancements.

We observe, as shown in Figure 4.12B, that the experimental Form II enhancement (ε_{II} = 31) is larger than the Form M enhancement (ε_M = 5). It means that the Form M is further away from the radical solution than Form II. Also, we observe that the measured build-up time of Form II is 11 seconds whereas its intrinsic T_1 is 23 s. Also, the build-up time of Form M is the same as its intrinsic T_1 (7 seconds). It means that Form II is affected by PRE, whereas Form M is not affected by PRE. This is why we postulate that **the polymorphic transition is only occurring at the surface of the particle**, leading to a layer structure as shown in Figure 4.12B. We see here that there is a gradient of enhancements: 150 in the radical solution, 31 in Form II, and 5 in Form M. These experimental measurements are well reproduced by numerical simulations (Figure 4.12C-D) in agreement with a layer structure.

Of course, now we want to overlap numerical simulations. As shown in Figure 4.12D we can successfully reproduce the enhancement measured at 30 s recycle delay with a 0.5 μm radius Form M core and a 10 nm Form II layer.
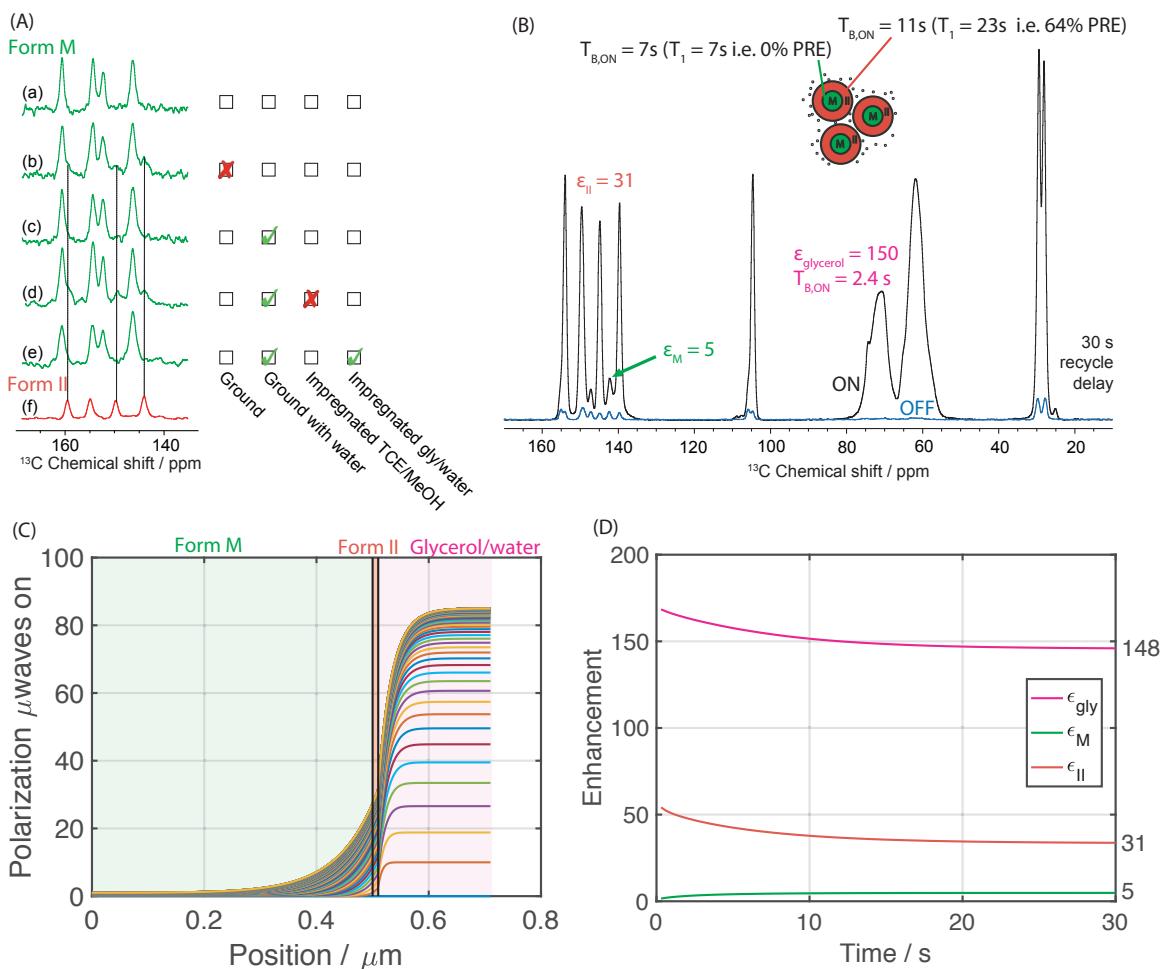

Figure 4.12: (A) Comparison of ^{13}C CPMAS solid-state NMR spectra as a function of the grinding procedure and the solvent used for impregnation of Form M. All spectra were recorded with a 16.4 T spectrometer at ca. 300 K. (a) Pure Form M before any procedure. (b) Mixture of Forms M and II obtained after grinding at room temperature. (c) Form M after grinding with a drop of water. (d) Mixture of Forms M and II after grinding with a drop of water and impregnation with TCE/methanol (95/5) solution. (e) Form M after grinding with a drop of water and impregnated with a glycerol-d_8/D_2O/H_2O (6/3/1) solution. (f) Pure Form II. (B) ^{13}C CPMAS solid-state NMR spectra of Form M ground and impregnated with TCE/methanol (95/5) with (red) and without (blue) microwave irradiation at 30 s recycle delay. (C) Simulated polarization as a function of position for different times. (D) Simulated enhancements for Form M and Form II as a function of time. Parameters for numerical simulations are shown in the following table.

parameter	L_M	L_{II}	$T_{B,s}$	$T_{1,M}$	$T_{1,II}$	C_s	$C_{II,M}$	D_s	D_t	ε_0	ε_{depo}	v_r
value	0.5	0.01	2.4	7	23	18	66	$2.5\ 10^{-4}$	$6.7\ 10^{-5}$	150	0.5	8
unit	μm	μm	s	s	s	mol.L^{-1}	mol.L^{-1}	μm^{2}s^{-1}	μm^{2}s^{-1}	/	/	kHz

We notice on Figure 4.12D that the enhancement of Form M increases as a function of time. We will see later that in our DNP systems where the target T_1 is longer than the solution T_B, an increasing enhancement can be the signature of a compound being isolated from the radical solution by a shell (here a shell of Form II).

4.3.2 Lipid nanoparticles

This section is adapted with permission from Viger-Gravel, J.; Schantz, A.; Pinon, A. C.; Rossini, A. J.; Schantz, S.; Emsley, L. Structure of Lipid Nanoparticles Containing siRNA or mRNA by Dynamic Nuclear Polarization-Enhanced NMR Spectroscopy *Journal of Physical Chemistry B* **2018**, *122*, 2073-2081.

A challenge in medicine today is the ability to deliver drugs to specific targets, for example, to inhibit cancer cells without damaging the surrounding healthy tissues. Cell membranes are mostly composed of lipid bilayers, and their hydrophobic nature protects the cells from hydrophilic molecules in the extracellular matrix. To achieve cellular internalization of hydrophilic bioactive molecules, many carrier-mediated delivery systems have been proposed.[16] However, most of these systems may show clinical side effects and have not been approved for in vivo applications or low efficacy because of poor cellular uptake or clearance by the mononuclear phagocyte system. Lipid nanoparticles (LNPs) show a high promise to overcome these disadvantages for drug delivery of small interfering RNA (siRNA) or messenger RNA (mRNA) because they can form less-toxic highly stable complexes between the cargo and the LNP and achieve target-specific cellular internalization and release of hydrophilic bioactive molecules. However, their internal structure still remains unknown.
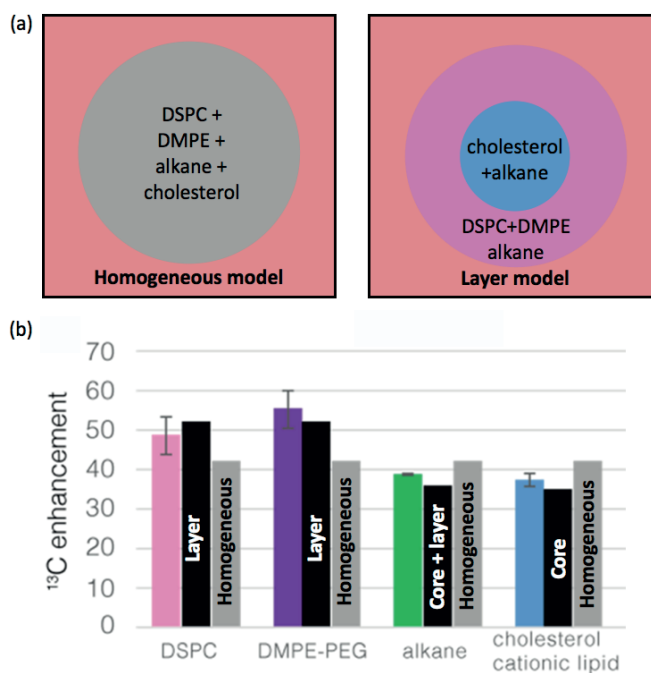

Figure 4.13: (a) Schematic representation of the two models in competition for the description of the structure of lipid nanoparticles. (b) Average enhancements for the different components of the lipid nanoparticles. The parameters for simulations are shown in the following table.

parameter	L_{LNP}	L_{layer}	L_{source}	$T_{B,s}$	T_1	D_s	ε_0	ε_{depo}	ν_r
value	0.06	5.5	0.1	1.24	1.41	$1\ 10^{-3}$	96	0.5	12.5
unit	µm	nm	µm	s	s	$\mu m^2 s^{-1}$	/	/	kHz

By placing the LNPs in a radical solution suitable for DNP, we can study this system via relayed DNP. Here the molecular probes are the different components of the LNP. With ^{13}C CPMAS experiments, we can measure different enhancement on each ^{13}C resonance of the LNP components, which we can compare

with numerical simulations in order to determine the internal structure of the particle. Two models (Figure 4.13a) that represent the possible extreme cases of the LNP structure, homogeneous or layered domain, are compared by numerical proton spin diffusion simulations. Figure 4.13b compares the best fits between the experimentally observed averaged ^{13}C enhancement and the predictions of the numerical simulations for homogeneous and layer models. We also assume that the spin-diffusion constants (D) inside the LNP and in the LNP layer (in the case of the layer model) are lower ($D_{in} \sim 10^{-4}$ $\mu m^2 s^{-1}$) than outside in the radical solution ($D_{out} = 10^{-3}$ $\mu m^2 s^{-1}$). The lower spin diffusion constant inside the LNP is included to account for molecular dynamics, which might be explained by additional mobile moieties such as methyl groups and alkane chains.

The homogeneous model mimics a homogeneous LNP that displays an equal value for the enhancement for all components. The layer model represents a layered structure, where the simulated polarization for the layer, core and core+layer regions corresponds to the LNP components: DSPC + DMPE-PEG, cholesterol, and alkanes, respectively.

We immediately see that for the homogeneous case, which corresponds to the homogeneous core structure where all LNP components are uniformly distributed in the domain, simulations predict the same value of the enhancement for all of the different components. This is clearly not in agreement with the data. In contrast, **simulations for the layer model are in good agreement with the data and predict that we should measure different values of the enhancements for the different components, with the following enhancement trend: surface (layer) > global (core + layer) > core**. DSPC and DMPE-PEG have higher enhancements than the other components in all four LNP samples. This suggests there is an enrichment of DSPC and DMPE-PEG lipids at the surface of the particles and that the cholesterol is located in the core region of the LNP domain. A Weibull size distribution was used for numerical simulations, as detailed is ref 16.

Here, relayed DNP experiments combined with numerical simulations can help us distinguish if particles contain homogeneously distributed compounds, or if the particle is organised with layers. It is important to notice that these conclusions can be drawn independently from surface effects.

4.3.3 Crystalline nanoparticles

CNPs are defined as colloidal dispersions of crystalline nanoparticles, in which the drug nanoparticles are usually poorly soluble in water. The problem of insolubility can be compensated by small particle size, usually below 300 nm, in order to enable intravenous drug delivery. The high surface area enables a faster dissolution rate as compared to larger crystals. Another advantage of CNPs is that the drug content is much higher than in the case of liposomes or micellar systems. Finally, CNPs do not usually involve any problematic additives, and are often less toxic or less likely to lead to undesirable effects than other formulations.

CNPs are constituted with 3 main components. First, the dispersion is a D_2O based solution. The active pharmaceutical ingredient (API) is present as nanometer size crystalline particles. These CNPs are then coated with a surfactant, for example a DSPE-PEG polymer, which stabilizes the particles and enables reduced sizes in the preparation process of the nanoparticles. Usually, less than 1% (w/w) of polymer is needed to provide good stabilization of the particles. Moreover, the DSPE-PEG layers prevent aggregation of the particles in the blood, and make them less prone to uptake by the liver, which can lead to a longer circulation times. Consequently, the choice of the stabilizer plays a crucial role in the stability and dynamics of the CNPs. The properties and thickness of the stabilizing layer are thus key in the conception of such formulations. However, methods to study the structure of these layers are scarce.

We will see that we can use relayed DNP to measure the thickness of the PEG layer.

By placing the CNPs in a radical solution suitable for DNP, we can study this system via relayed DNP. The CNP dispersion can be mixed with AMUPol, ^{12}C-glycerol-d_8, and sodium formate. ^{13}C-depleted glycerol is used since the glycerol resonance is overlapping the PEG resonance. A few mg of ^{13}C-labeled sodium formate is then added to probe the behaviour of the radical solution. The resulting sample is expected to be heterogeneous: the radical solution contains sodium formate molecules, PEG molecules are partially in the solvent (20% of the total PEG concentration) and partially at the surface of the API (80% of the total PEG concentration), and the API would be exempt of radical molecule, as shown in Figure 4.14.

Thanks to ^{13}C chemical shift distinction, it is possible to independently record the time evolution of the signals of formate, PEG and API resonances during the saturation recovery experiment.
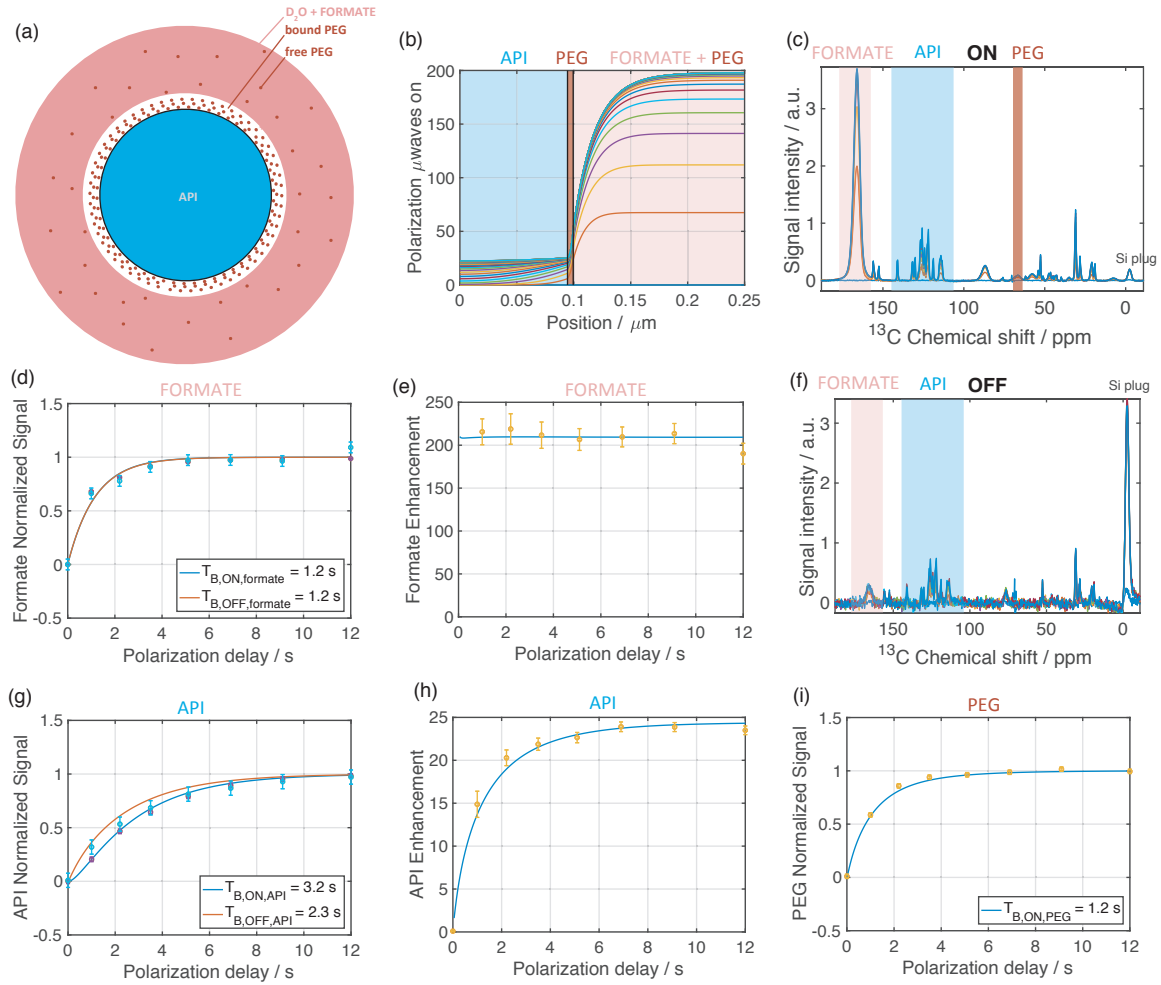
Figure 4.14: (a) Schematic representation of what is believed the structure of a CNP dispersion. (b) Simulated polarization as a function of position for different time steps in the CNP system. 13C CPMAS spectra recorded at 9.4 T, 100 K and 12.5 kHz of the LNP dispersion in ^{12}C-glycerol-d_8/D$_2$O/H$_2$O (6/3/1) containing 0.5 mg of ^{13}C-labelled sodium formate with (c) and without (f) microwave irradiation. Color rectangles show areas that were taken for signal integration. (d) Normalized signal from the ^{13}C formate resonance as a function of the polarization delay. (b) Enhancement of the ^{13}C formate resonance as a function of the polarization delay. (g) Normalized signal from the ^{13}C API resonances as a function of the polarization delay. (h) Enhancement of the ^{13}C API resonance as a function of the polarization delay. (i) Normalized signal from the ^{13}C DSPE-PEG resonance as a function of the polarization delay. Parameters for numerical simulations are given in the following table.

parameter	L_{API}	L_{PEG}	$T_{B,s}$	$T_{1,API}$	$T_{1,PEG}$	C_{API}	C_{PEG}	C_s	D_s	D_{PEG}	D_{API}	ε_0	ε_{depo}	v_r
value	189	5	2.4	26	48	74	101	12	$2.7\ 10^{-4}$	$5.6\ 10^{-4}$	$5\ 10^{-3}$	210	0.5	12.5
unit	nm	nm	s	s	ms	mol.L^{-1}	mol.L^{-1}	mol.L^{-1}	µm^{2}s^{-1}	µm^{2}s^{-1}	µm^{2}s^{-1}	/	/	kHz

Figure 4.14, shows the comparison between experiment and prediction for a spherical nanocrystal having a diameter of 189 nm, with a DSPE-PEG layer of 5 nm. In Figure 4.14d and 4.14e, simulations reproduce the behavior of both the formate signals and enhancement. In Figure 4.14g the API signal build-ups are well reproduced. In Figure 4.14h, the enhancement of the API increases as a function of time in both the simulated and experimental data. **This is due to a faster signal build-up without microwave irradiation than with microwave irradiation**. Indeed, polarization builds-up roughly with T_1 in the µwaves off case, whereas hyperpolarization can only build up with spin diffusion in the µwaves on case. Hyperpolarization arrives in the API by spin diffusion after the time needed to go through the PEG

104

layer. This explains the slower build-up of the μwaves on API signal in Figure 4.14g, and the delayed increase of the experimental and simulated enhancements. Experimental measurements are in agreement with the expected PEG resonance build-up time μwaves on in Figure 4.14i.

Here we find the best agreement between numerical simulations and experimental data for L_{PEG} = 5 nm $T_{1,PEG}$ = 48 ms. This suggest that the AMUPol radical has a high affinity with the PEG molecules at the surface of the CNP particle. It seems reasonable since both PEG and AMUPol have PEG chains. The DSPE-PEG can thus be considered as *AMUPophillic*.

We see here that the behavior of the enhancement at early time can give interesting information about the thickness of the coating layer, here being 5 nm thick.

4.3.4 Core-shell particles

Core-shell particles are composed of a polystyrene spherical core having a 84 nm radius, coated with mesoporous silica which pores contain CTAB. These well-defined core-shell particles can be impregnated with a radical solution of glycerol-d_8/D_2O/H_2O (6/3/1) containing 12 mM AMUPol. **The system can be then studied by relayed DNP as shown in Figure 4.15 in order to confirm its structure**. Here, we assume that the radical molecule does not enter the pore. The DNP effect is expected to occur at the exterior of the particle, and hyperpolarization is expected to spin diffuse through the protons of the CTAB molecules, down to the polystyrene core.
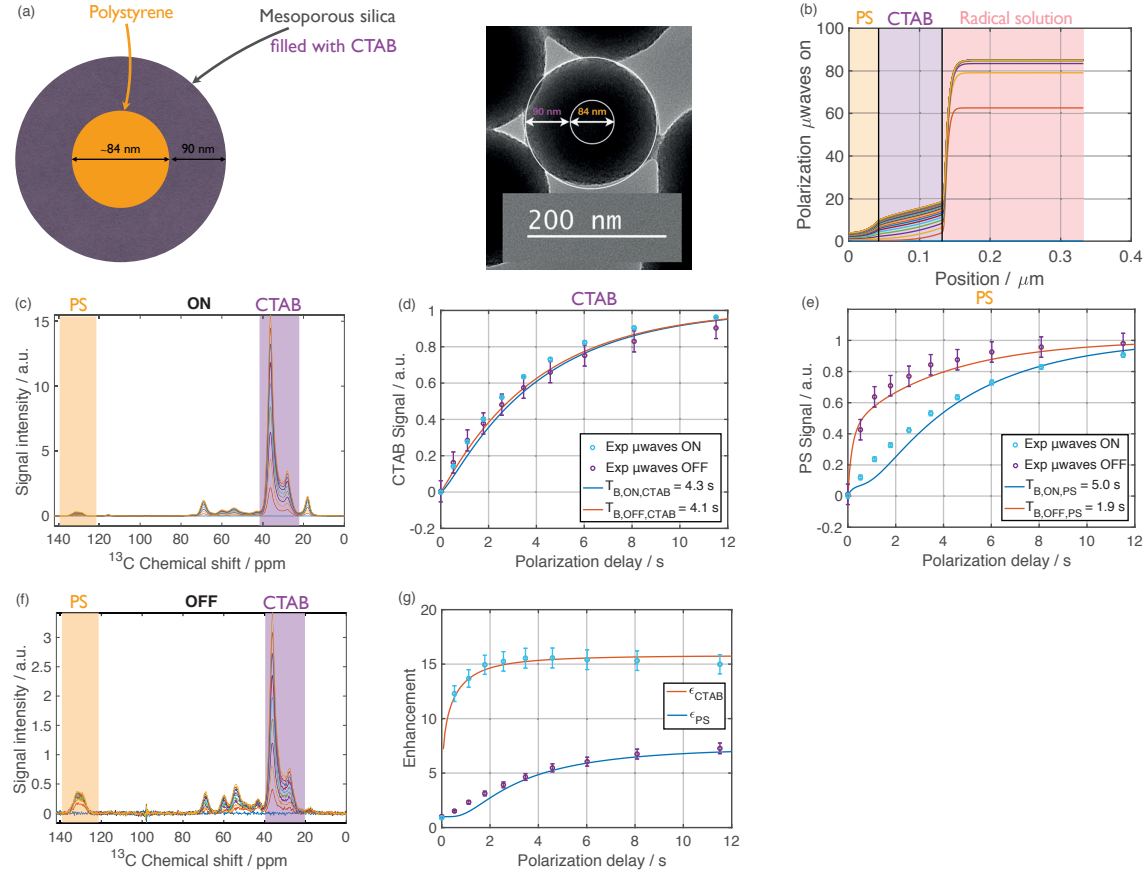
Figure 4.15: (a) Scheme representing the multi-layer system along with a TEM image of the system. (b) Simulated polarization as a function of position is the core-shell system, for different time steps. ^{13}C CPMAS spectra recorded at 9.4 T, 100 K and 12.5 kHz MAS of polystyrene particles coated with mesoporous silica containing CTAB, impregnated with ^{12}C-glycerol-d_8/D_2O/H_2O (6/3/1) containing 12 mM of the biradical AMUPol with (c) and without (f) microwave irradiation. Color rectangles corresponds to areas used for integration. (d) CTAB signal build-up as a function of time with and without microwaves. (e) PS signal build-up as a function of time with and without microwaves. (g) PS and CTAB enhancements as a function of time. Circles are experimental measurements, and solid lines are simulations. Parameters for numerical simulations are given in the following table.

param	L_{PS}	L_{CTAB}	L_s	$T_{1,PS}$	$T_{1,CTAB}$	$T_{B,s}$	C_{PS}	C_{CTAB}	C_s	D_{PS}	D_{CTAB}	D_s	ε_0	ε_{dep}	v_r
value	42	90	200	2.1	6	0.5	70	102	11	$5\ 10^{-4}$	$1.2\ 10^{-3}$	$6.5\ 10^{-5}$	85	0.5	12.5
unit	nm	nm	nm	s	s	s	mol.L^{-1}	mol.L^{-1}	mol.L^{-1}	µm^{2}s^{-1}	µm^{2}s^{-1}	µm^{2}s^{-1}	/	/	kHz

We see in Figure 4.15 that all behaviours are well reproduced, confirming that our numerical simulations are robust for such layered systems. Indeed, the CTAB enhancement is measured to be higher than the PS enhancement. Besides, the PS enhancement is measured to increase with time, as expected for a core domain being protected from the radical solution by a shell (the shell being CTAB). The only deviation between experiments and simulations is for the PS µwaves on signal, and enhancement at early times. We notice that the simulation predicts a late increase of the PS signal and enhancements, whereas the experiment shows a faster increase. This could be due to the fact that in some of the particles, the AMUPol molecule can partially entering the pores, and bring hyperpolarization to PS faster than expected. This could be also due to a slight distribution or layer thicknesses.

Overall, the excellent agreement between numerical simulations and layer system shows that simulations can be used to quantitatively confirm the structure of complex layered systems.

4.4 Spin diffusion in inorganic materials

The following section is adapted with permission from Bjorgvinsdottir, S.; Walder, B. J.; Pinon, A. C.; Emsley, L. Bulk Hyperpolarization of Inorganic Materials *Submitted* **2018**.

4.4.1 Pulse cooling

One of the most challenging cases for NMR is the hyperpolarization of proton-free inorganic materials. Examples include most inorganic oxides including SiO_2, as well as semi-conductors such as GaP, and materials such as silicon carbide, elemental Silicon, or pure carbons. In these cases, impregnation DNP cannot be used to hyperpolarize the bulk of the materials via ^1H-^1H spin diffusion.

Spin diffusion among heteronuclei is often thought to be negligible.[17] We have seen in chapter 1 that for example, ^{13}C spin diffusion rates in diamond at natural abundance are expected to be ~15000 times slower than ^1H-^1H spin diffusion rates in typical organic solids.[18] However, we note here that relaxation times in inorganic materials can often be on the order of hours, or a factor 10^3 longer than in a typical organic solid. With this realization, we suggest that it might be possible to hyperpolarize inorganic solids by heteronuclear spin diffusion.

We will see here how impregnation DNP can be combined with spin diffusion between heteronuclei to provide a general strategy to hyperpolarize proton-free inorganic solids, with a pulse cooling cross polarization method that transfers hyperpolarization from protons to nearby heteronuclei.

We have given in chapter 2 some expressions for the steady state DNP enhancement obtainable inside a spherical particle being polarized by spontaneous spin diffusion from a radical solution at the surface. From that we can deduce that the maximum polarization gain with respect to a one-pulse direct acquisition experiment, gives an upper bound of:

$$P_{target} = 1 + 3(P_{source} - 1)\frac{\sqrt{DT_1}}{R}\left[\coth\left(\frac{R}{\sqrt{DT_1}}\right) - \frac{\sqrt{DT_1}}{R}\right] \tag{4.5}$$

where $P_{target/source}$ is the potential gain in target/source polarization with respect to Boltzmann polarization, D is the spin diffusion coefficient of the target nucleus, T_1 the intrinsic longitudinal relaxation time of the target in the absence of radical solution, and R is the radius of the particle. The measured gain is likely to be less than this since the expression does not contain the eventual difference in temperature, experimental efficiency between the two experiments, surface effects, or smaller spin diffusion coefficient due to chemical shift anisotropy or chemical shift differences.

Using equation (4.5), with a radical solution enhancement of P_{source} = 175, and spherical particles with radii R = 0.5 for static samples, we can estimate P_{target} for different compounds as shown in Table 4.2. Perhaps surprisingly, enhancements of an order of magnitude in many of these samples by heteronuclear spin diffusion at natural isotopic abundance looks feasible in this analysis.

Table 4.2. Estimated potential polarizations from equation (4.5) for five different materials at natural isotopic abundance for a static sample, based on P_{source} = $175(\gamma_{1H}/\gamma)$ and R = 0.5 μm with estimates of D according to $D = D_{PS}(C/C_{PS})^{1/3}(\gamma/\gamma_{1H})^2$, where D_{PS} is the diffusion constant for protons in polystyrene in a static sample (1.5 x 10^{-4} $μm^2s^{-1}$),[8] C is the average concentration of active spins in the

sample of interest, C_{PS} is the concentration of protons in polystyrene (70 M), and using estimates for the longitudinal relaxation times T_1.

Nucleus	C / M	D / nm^{2}s^{-1}	T_1 / s	P_{target}
^{19}F in CaF$_2$ ‖ [100]	81.5	530	115	141
^{31}P in GaP	41.1	78	500[†]	128
^{119}Sn in SnO$_2$	4.0	31	1000[†]	121
^{13}C in diamond	3.25	13	10^{5}[‡]	173
^{125}Te in CdTe	1.72	17	3600[†]	141
^{113}Cd in CdTe	2.98	9.9	3600[‡]	126
^{29}Si in α-quartz	2.06	6.9	10^{5}[‡]	171

† measured on a powdered sample; ‡ estimated

This is confirmed in Figure 4.16B, which shows DNP enhanced ^{1}H-^{119}Sn CPMAS spectra of SnO$_2$ recorded at 9.4 T and 100 K using the pulse sequence shown in Figure 4.16A that allows for ^{119}Sn spin diffusion between cross polarization and detection. Spin diffusion between the tin nuclei clearly occurs during τ_z. In the spectra with τ_z = 0 peaks attributed to both surface (-590 ppm) and bulk (-603 ppm) sites are observed. As the ^{119}Sn spin diffusion delay is increased, we clearly see the surface signal diminish, and the bulk signal increase over times up to 200 seconds. This behavior can be quantitatively reproduced with numerical simulations of spin diffusion as shown in Figure 4.14D, and using the parameters for ^{119}Sn from Table 4.2. Actually, the numerical simulations predicted such a bulk signal behavior (Figure 4.16D, blue curve) <u>even before</u> we performed performing the experiment!

Very similar behavior is observed for the same experiment on for **^{31}P spin diffusion** in powdered GaP, for **^{113}Cd spin diffusion** in CdTe, and for **^{29}Si spin diffusion** in SiO$_2$, as shown in ref 19. Again, in all cases, the surface and bulk sites are clearly observed, with diffusion from one to the other on the timescale of 100 s.
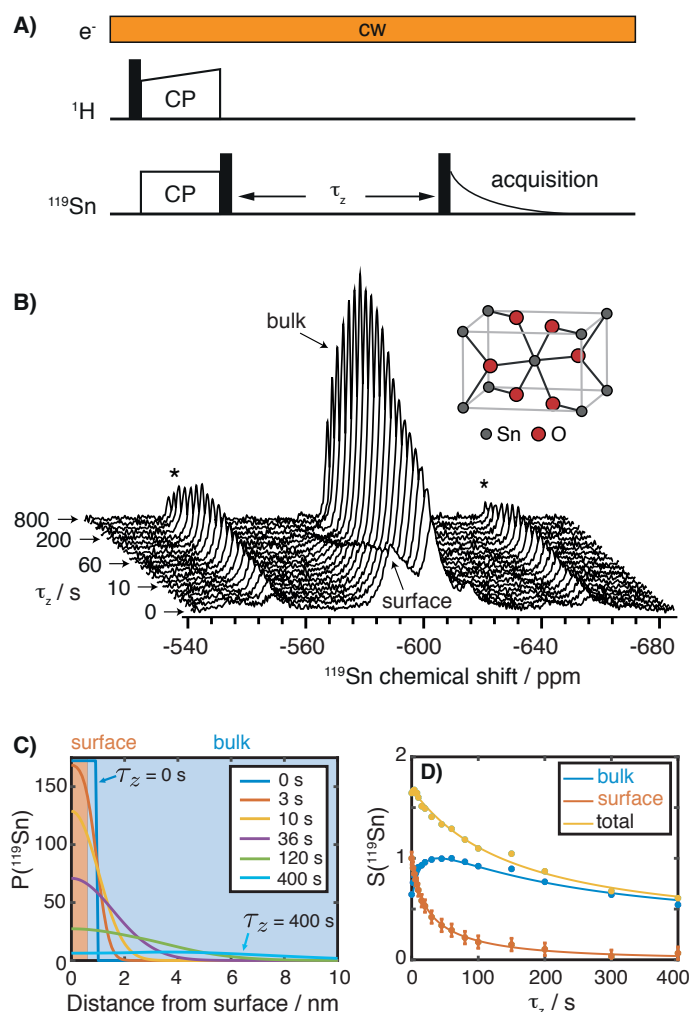
Figure 4.16: [119]Sn spin diffusion observed in the DNP enhanced CPMAS ^{119}Sn NMR spectrum of powdered tin dioxide impregnated with a 16 mM solution of TEKPol in TCE spinning at 8 kHz. A) The *z*-filtered [119]Sn CP sequence. Spin diffusion occurs during the τ_z interval, when magnetization is stored longitundinally between polarization and signal acquisition. B) DNP enhanced [119]Sn CP MAS spectra acquired as a function of τ_z. Spinning sidebands are marked with asterisks. Full experimental details are given in ref [19]. C) Simulated [119]Sn polarization as a function of the distance from the surface of the particle for different τ_z times. D) [119]Sn normalized bulk (blue), surface (red) and total (yellow) signals as a function of τ_z. Experimental points are shown as a scatter whereas numerical simulations are shown as solid lines. Parameters are shown in Table 4.2.

Hyperpolarization can in principle be efficiently implemented by the either direct DNP of the heteronuclei at the surface from the radicals in the wetting solution, or by the pulse cooling scheme shown in Figure 4.17A. In that scheme, we use multiple cycles of flip-back cross polarization to repeatedly cool the heteronuclei at the surface of the material, followed by spin diffusion periods to propagate polarization into the bulk of the material on a longer timescale. Phase cycling can be adjusted to detect signal coming either only from ^{1}H hyperpolarization, or to include both polarization from CP and from direct heteronuclear DNP. During the spin diffusion periods ^{1}H hyperpolarization is rapidly replenished in the impregnating phase. Typically, delay between CP blocks should be longer than the [1]H

build-up time in the solvent, and the overall length of the pumping sequence should be long enough to allow spin diffusion to accumulate polarization in the bulk.
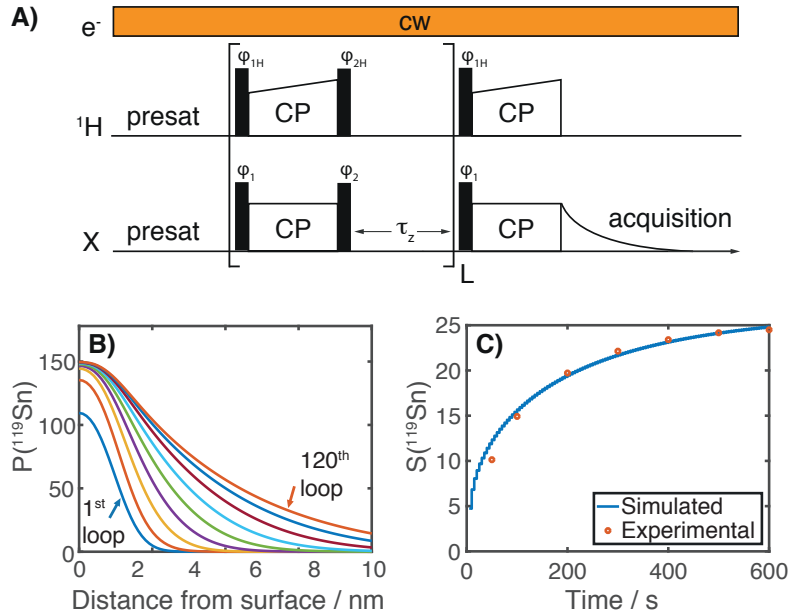

Figure 4.17: Bulk nuclear hyperpolarization by pulse cooling using multiple-contact CP. A) The pulse cooling CP sequence. Phase alternation of the pulses ϕ_1 and ϕ_2 relative to ϕ_{1H} and ϕ_{2H} can be can be used include the contribution from direct DNP and intrinsic longitudinal recovery of heteronuclei. B) Simulated [119]Sn polarization as a function of the distance from the surface of the particle after different numbers of loops, with τ_z = 5 s. C) Simulated [119]Sn signal enhancement compared to a pulse acquire experiment as a function of time. Experimental points are shown as circles whereas numerical simulations are shown as solid lines. Parameters used in simulations which provide good agreement with pulse cooling experiments on tin dioxide are given in the following table. More details can be found in ref [19].

parameter	L_t	L_s	$T_{B,s}$	$T_{1,API}$	C_s	C_t	D_s	D_t	ε_0	v_r	τ_z	L
value	0.5	150	3.35	1400	18	3.98	$8.1\ 10^{-5}$	$3.5\ 10^{-8}$	356	8	5	120
unit	µm	nm	s	s	mol.L^{-1}	mol.L^{-1}	µm^{2}s^{-1}	µm^{2}s^{-1}	/	kHz	s	/

Here again, numerical simulations reproduce well the experimentally observed behavior. The spinning rate dependence generally follows expectations. As the MAS rate is increased, the measured polarization inside the SnO$_2$ particle decreases, since the spin diffusion coefficient decreases with MAS. More details are given in ref 19.

We see here that using numerical simulation, we can successfully reproduce the accumulation of hyperpolarization inside proton-free particles, and reproduce the build-up behaviour of the [119]Sn spins inside the particle. That way, we are sure that we understand the mechnaisms that come into play.

4.4.2 Lead halide perovskites

Lead halide perovskites are highly promising semiconducting materials for optoelectronic and photovoltaic applications. All-inorganic cesium lead halide ($CsPbX_3$, X=Cl, Br, I) nanocrystals have recently emerged as a viable alternative to classical II-VI metal chalcogenides used in LED and solar cell applications. Similarly, multi-component organic-inorganic lead halide perovskites ($APbX_3$, A=methylammonium ($CH_3NH_3^+$, MA), formamidinium ($CH_3(NH_2)_2^+$, FA), X=Cl, Br, I)) applied as light absorbers in solar cells, currently provide power conversion efficiencies of over 22%.

All-inorganic lead halide perovskite quantum dots (QDs) doped with transition metal and lanthanide ions show particularly advantageous optoelectronic properties such as strongly sensitized luminescence and improved thermal and air stability. The most widely investigated materials are $CsPbCl_3$, $CsPbBr_3$, and $CsPbI_3$, as well as mixed-halide compositions doped with Mn^{2+} and very recently Ce^{3+}. The strategy of transition metal ion doping has also been proposed as a means of fine tuning of photovoltaic parameters in organic-inorganic lead halide perovskites. Incorporation of transition metal ions into the perovskite lattice is typically evidenced using XRD, UV-VIS, PL, and in some instances by EPR and HAADF-STEM. While some of these methods provide atomic-level resolution (HAADF-STEM, EPR) and others provide insight into phase composition (XRD), none of them achieves both. On the other hand, NMR is capable of both by utilizing local nuclear probes such as ^1H, ^{13}C, ^{14}N, ^{133}Cs, ^{87}Rb, ^{39}K and ^{207}Pb.

Most transition metal and lanthanide ions are paramagnetic and therefore are expected to induce large PRE effects that can be observed for distances up to 2 nm from the unpaired electron in diamagnetic perovskite materials. We know now that, given the right conditions, spin diffusion can transport the magnetization to nuclei farther away from the paramagnetic centers, leading to substantially shorter T_1 in the bulk of the material.
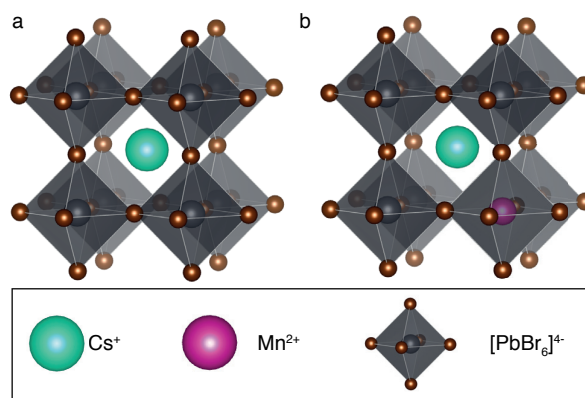

Figure 4.18. Schematic representation of paramagnetic doping in perovskites: (a) parent $CsPbBr_3$ lattice, (b) homovalent B-site replacement

Figure 4.18 schematically shows how paramagnetic metal ions can be incorporated into perovskite lattices. Since the Cs-Pb distance in the parent $CsPbBr_3$ lattice (Figure 4.18) is about 0.5nm, substituting Pb^{2+} by Mn^{2+} is expected to cause substantial PRE. To verify this hypothesis, we carried out ^{133}Cs relaxation measurements on mechanochemically synthesized $CsPbBr_3$ undoped and stoichiometrically doped with 0.5, 3 and 8 mol% of Mn^{2+}. The corresponding saturation-recovery curves (Figure 4.19) show

significantly faster recovery (shorter T_1) of ^{133}Cs nuclei in the perovskite phase of the Mn^{2+}-doped samples **and indicate incorporation of the paramagnetic dopant into the perovskite lattice**.
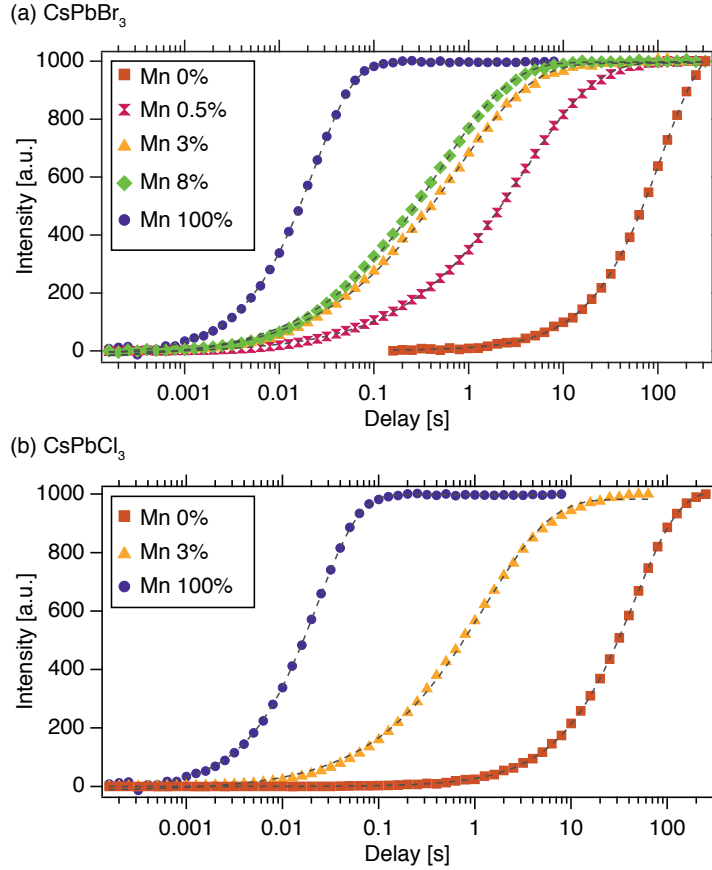
(a) CsPbBr$_3$

(b) CsPbCl$_3$

Figure 4.19. Cesium signal build-up curves measured using a saturation-recovery for (a) CsPbBr$_3$ doped with different manganese percentages, and (b) CsPbCl$_3$ doped with different manganese percentages. Experimental conditions: at 9.4 T and 20 kHz MAS. Dashed lines are fits of stretched exponential.

Since paramagnetic doping leads to a distribution of apparent relaxation times, the curves are best fitted using a stretched exponential function. The results are summarized in Table 4.3.

Table 4.3: ^{133}Cs T_1 relaxation times of Mn^{2+}-doped CsPbBr$_3$ and CsPbCl$_3$ fitted using the stretched exponential function. The reported errors correspond to one standard deviation in the precision of the fit.

material	^{133}Cs T_1 [s]	stretching parameter β
CsPbBr$_3$	108.5 ± 1.2	1.00
CsPb$_{0.995}$Mn$_{0.005}$Br$_3$	3.995 ± 0.023	0.58
CsPb$_{0.97}$Mn$_{0.03}$Br$_3$	0.729 ± 0.012	0.54
CsPb$_{0.92}$Mn$_{0.08}$Br$_3$	0.4848 ± 0.0066	0.57
CsBr+MnBr$_2$	0.02328 ± 0.00014	1.00
CsPbCl$_3$	45.94 ± 0.11	0.94
CsPb$_{0.97}$Mn$_{0.03}$Cl$_3$	1.267 ± 0.023	0.63

The fact that the stretching parameter β is significantly different than 1 for doped $CsPb_{1-x}Mn_xBr_3$ perovskite confirms the incorporation of manganese atoms in the perovskite lattice.

Now the first question is: Is the PRE effect caused by Mn direct, or relayed through Cs-Cs spin diffusion?

We can calculate again the longitudinal pseudopotential using the PRE equation from chapter 1 for S = 5/2, τ = 350 ns for Mn(II) and using the following estimation for the spin diffusion coefficient $D_{Cs} = 10^{-2}$ A^2s^{-1}. We find ρ_1 = 134 A. Consequently, ρ_1 is bigger than the length scales involved. Indeed, the average Mn-Mn distances in a $CsPbBr_3$ lattice doped with 0.5%, 3%, and 8% Mn are 2.13 nm, 1.16 nm, and 0.84 A respectively. **It means that the PRE effect induced by Mn is not relayed by Cs-Cs spin diffusion.**

The second question is: are manganese atoms homogeneously spread in the $CsPbBr_3$ lattice, or are they forming clusters?

In order to prove the absence of cluster in the $CsPb_{1-x}Mn_xBr_3$ perovskite, we model the spatial distribution of the polarization in the presence of a PRE effect induced by the presence of manganese using the diffusion equation presented in chapter 2 and the PRE effect equation introduced in chapter 1.

In the model, we consider spherical clusters of $CsMnBr_3$ surrounded by $CsPbBr_3$ domains. In the cluster, the cesium spin lattice relaxation time was measured to be $T_{1,cluster}$ = 23 ms (the measurement was performed on the $CsMnBr_3$ perovskite alone). Outside the cluster, the cesium T_1 depends on distance between the cesium atom and the closest manganese atom from a cluster. We thus model the spatial dependence of T_1 as:
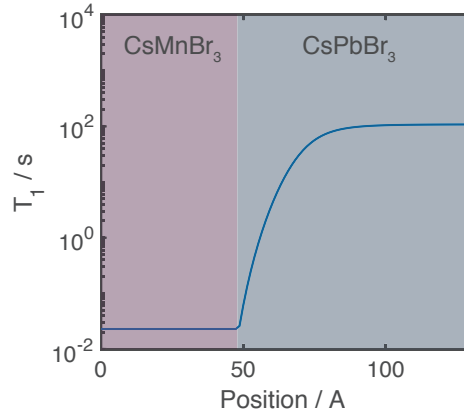

Figure 4.20: Simulated spatial dependence of spin lattice relaxation time T_1 in the two domains. $T_{1,cluster}$ = 23 ms in the $CsMnBr_3$ lattice and progressively increases with a r^{-6} dependence up to $T_{1,dia}$ = 108.5 s in the $CsPbBr_3$ lattice for a cluster having a radius of 4.8 nm.

The resulting polarization can then be plotted as a function of position, for different time steps:
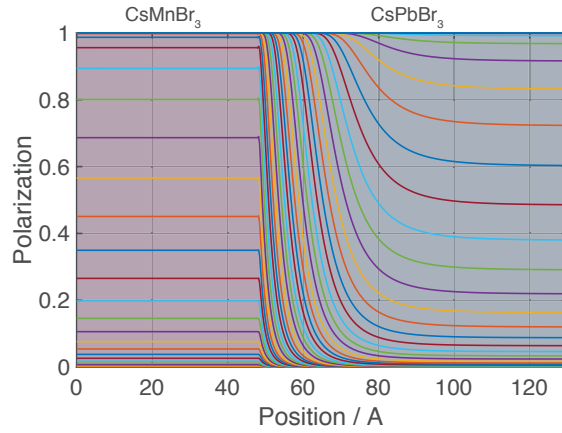
Figure 4.21: Simulated spatial dependence of the polarization for different time steps during a saturation recovery experiment in the two domains for a cluster having a radius of 4.8 nm, representing 3% of the total spherical volume.

As expected in Figure 4.21, the polarization builds up quickly in the CsMnBr$_3$ lattice due to strong PRE effects from the manganese atoms, and more slowly in the CsPbBr$_3$ lattice. Several simulations can be performed by varying the cluster radius (and adjusting the diamagnetic volume so that the doping percentage is constant) to see the effect on the simulated build-ups, as shown in Figure 4.22.
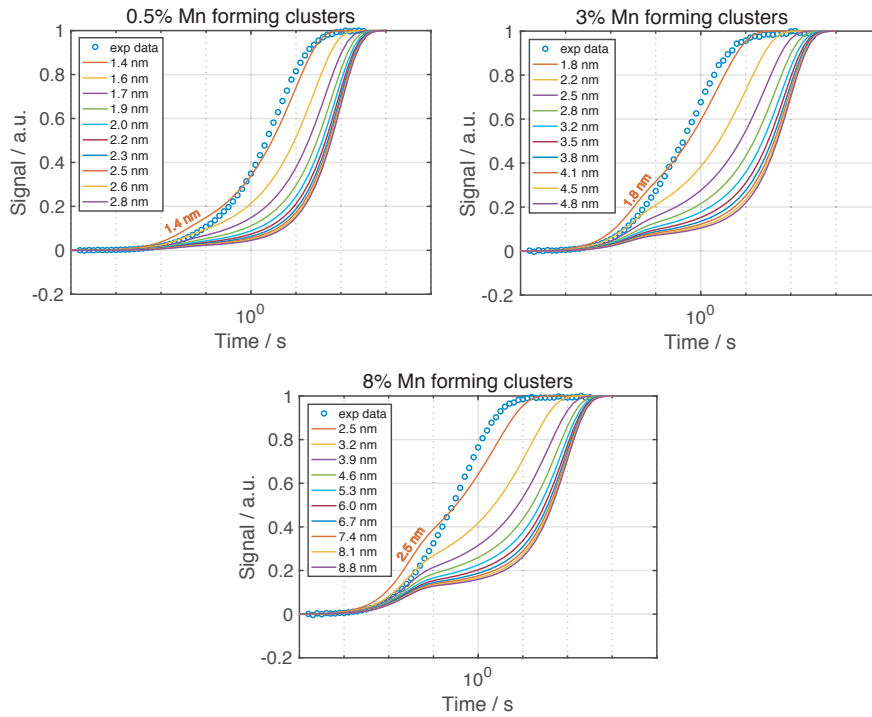
Figure 4.22: Experimental (blue circles) and simulated signal build-ups (solid lines) as a function of time for different cluster radii, for the three manganese dopings (0.5%, 3%, and 8%).

We observe in Figure 4.22 that for the largest cluster radii, the build-up behavior follows a clear bi-exponential pattern confirmed by fitting, where the first component corresponds to the cesium atoms located inside the cluster being affected by PRE with $T_{1,cluster}$ = 23 ms and represents 0.5%, 3%, and 8% of the total behavior, while the second component represent 99.5%, 97%, and 92% of the total behavior with $T_{1,dia}$ = 108 s, respectively. We confirm here that **at large cluster radii, the PRE effect in the diamagnetic CsPbBr$_3$ lattice is negligible and the build-up is no longer stretched**. However when the radii decreases, the surface area of the paramagnetic domain CsMnBr$_3$ increases, the PRE effect becomes relatively more important in the diamagnetic lattice, and the build-up shifts from a bi-exponential to a stretched exponential.

We can deduce from these simulations that the manganese does not form CsMnBr$_3$ clusters bigger than 1.6 nm (3 unit cells), 2.2 nm (5 unit cells), and 3.2 nm (6 unit cells) for the 0.5%, 3% and 8% doping percentages respectively in the diamagnetic crystalline lattice. Consequently, the incorporatin of manganese is quite homogeneous.

We notice that numerical simulations do not perfectly reproduce the experimental behavior. This could be due to the fact that numerical simulations consider the system as a continuum of polarization. This approximation is not a problem when the system is big as for radii much bigger than the inter nuclei distance. But this approximation becomes weaker when the length involved is on the order of the inter nuclei distance, as it is the case here for the smallest cluster radii.

References

(1) Zhang, W. R.; Cory, D. G. First direct measurement of the spin diffusion rate in a homogenous solid *Physical Review Letters* **1998**, *80*, 1324-1327.

(2) Spiegel, S.; Schmidt-Rohr, K.; Boeffel, C.; Spiess, H. W. H-1 SPIN-DIFFUSION COEFFICIENTS OF HIGHLY MOBILE POLYMERS *Polymer* **1993**, *34*, 4566-4569.

(3) Borckmans, P.; Walgraef, D. LONG-TIME BEHAVIOR OF FREE-INDUCTION DECAY IN PARAMAGNETIC SPIN SYSTEMS *Physical Review Letters* **1968**, *21*, 1516-+.

(4) Redfield, A. G.; Yu, W. N. MOMENT-METHOD CALCULATION OF MAGNETIZATION AND INTERSPIN-ENERGY DIFFUSION *Phys. Rev.* **1968**, *169*, 443-&.

(5) Borckmans, P.; Walgraef, D. IRREVERSIBILITY IN PARAMAGNETIC SPIN SYSTEM - FREE-INDUCTION DECAY AND LINE SHAPE IN CAF2 *Physical Review B* **1973**, *7*, 563-565.

(6) Tang, C. G.; Waugh, J. S. DYNAMICS OF CLASSICAL SPINS ON A LATTICE - SPIN DIFFUSION *Physical Review B* **1992**, *45*, 748-754.

(7) Boutis, G. S.; Greenbaum, D.; Cho, H.; Cory, D. G.; Ramanathan, C. Spin diffusion of correlated two-spin states in a dielectric crystal *Physical Review Letters* **2004**, *92*.

(8) Roos, M.; Micke, P.; Saalwachter, K.; Hempel, G. Moderate MAS enhances local H-1 spin exchange and spin diffusion *Journal of Magnetic Resonance* **2015**, *260*, 28-37.

(9) Rossini, A. J.; Zagdoun, A.; Hegner, F.; Schwarzwalder, M.; Gajan, D.; Coperet, C.; Lesage, A.; Emsley, L. Dynamic Nuclear Polarization NMR Spectroscopy of Microcrystalline Solids *Journal of the American Chemical Society* **2012**, *134*, 16899-16908.

(10) Schlagnitweit, J.; Tang, M. X.; Baias, M.; Richardson, S.; Schantz, S.; Emsley, L. Nanostructure of Materials Determined by Relayed Paramagnetic Relaxation Enhancement *Journal of the American Chemical Society* **2015**, *137*, 12482-12485.

(11) Pinon, A. C.; Schlagnitweit, J.; Berruyer, P.; Rossini, A. J.; Lelli, M.; Socie, E.; Tang, M. X.; Pham, T.; Lesage, A.; Schantz, S.; Emsley, L. Measuring Nano- to Microstructures from Relayed Dynamic Nuclear Polarization NMR *Journal of Physical Chemistry C* **2017**, *121*, 15993-16005.

(12) Perras, F. A.; Wang, L. L.; Manzano, J. S.; Chaudhari, U.; Opembre, N. N.; Johnson, D. D.; Slowing, I.; Pruski, M. Optimal sample formulations for DNP SENS: The importance of radical-surface interactions *Current Opinion in Colloid & Interface Science* **2018**, *33*, 9-18.

(13) Takahashi, H.; Fernandez-De-Alba, C.; Lee, D.; Maurel, V.; Gambarelli, S.; Bardet, M.; Hediger, S.; Barra, A. L.; De Paepe, G. Optimization of an absolute sensitivity in a glassy matrix during DNP-enhanced multidimensional solid-state NMR experiments *Journal of Magnetic Resonance* **2014**, *239*, 91-99.

(14) Kubicki, D. J.; Casano, G.; Schwarzwalder, M.; Abel, S.; Sauvee, C.; Ganesan, K.; Yulikov, M.; Rossini, A. J.; Jeschke, G.; Coperet, C.; Lesage, A.; Tordo, P.; Ouari, O.; Emsley, L. Rational design of dinitroxide biradicals for efficient cross-effect dynamic nuclear polarization *Chemical Science* **2016**, *7*, 550-558.

(15) Fucke, K.; McIntyre, G. J.; Wilkinson, C.; Henry, M.; Howard, J. A. K.; Steed, J. W. New Insights into an Old Molecule: Interaction Energies of Theophylline Crystal Forms *Crystal Growth & Design* **2012**, *12*, 1395-1401.

(16) Viger-Gravel, J.; Schantz, A.; Pinon, A. C.; Rossini, A. J.; Schantz, S.; Emsley, L. Structure of Lipid Nanoparticles Containing siRNA or mRNA by Dynamic Nuclear Polarization-Enhanced NMR Spectroscopy *Journal of Physical Chemistry B* **2018**, *122*, 2073-2081.

(17) Lafon, O.; Rosay, M.; Aussenac, F.; Lu, X.; Trebosc, J.; Cristini, O.; Kinowski, C.; Touati, N.; Vezin, H.; Amoureux, J. P. Beyond the silica surface by direct silicon-29 dynamic nuclear polarization *Angew Chem Int Ed Engl* **2011**, *50*, 8367-8370.

(18) Becerra, L. R.; Gerfen, G. J.; Temkin, R. J.; Singel, D. J.; Griffin, R. G. DYNAMIC NUCLEAR-POLARIZATION WITH A CYCLOTRON-RESONANCE MASER AT 5-T *Physical Review Letters* **1993**, *71*, 3561-3564.

(19) Björgvinsdóttir, S.; Walder, B. J.; Pinon, A. C.; Emsley, L. Bulk Hyperpolarization of Inorganic Materials *Submitted* **2018**.

Conclusions

In this thesis, we have made several progresses in terms of understanding polarization dynamics in DNP systems.

We have developed a numerical model that reproduces with high accuracy polarization dynamics in complex systems, based on the transport of polarization via spin diffusion.

We have shown the benefits of optimizing the radical and proton concentrations for homogeneous radical solutions. We have shown that high enhancements can be achieved even at low radical concentrations. We have explained with the help of numerical simulations why the Overhauser enhancement increases with increasing MAS rate. We quantitatively explain why flipping back the proton magnetization to the z-axis in MAS DNP or gating the microwaves in dDNP can improve the CP efficiency.

We have been able to measure the spin diffusion coefficient for polystyrene on a macro scale using relayed PRE combined with numerical simulations. We have then used this spin diffusion coefficient to measure the size of micro-particles by relayed DNP. We have confirmed the presence of surface effects when solid materials are being impregnated with radical solutions. With relayed DNP combined with the developed model, we have been able to determine the structure of polymorphic drugs, lipid nanoparticles, crystalline nanoparticles, and core-shell particles, by only performing CPMAS saturation recovery experiments.

Finally, we have shown that a variety of inorganic materials can be hyperpolarized by spin diffusion, and we have shown that perovskite materials can be doped with manganese and that the manganese atoms does not form clusters in the lattice.

Combining spin diffusion measurements such as saturation recovery, together with numerical simulations is a powerful tool to determine structures of complex systems. Now that this technique has been proved to work reliably, it can be used for a wide range of applications.

Appendix

Matlab Program:

```
m = 0; %m=0 for 1D, m=1 for 2D, m=3 for 3D
length_target = 0.1; %length of the target in um
length_source = 0.1; %length of the source in um
rstep = 500; %number of points in space domain
tmax = 100; %maximum time in s
tstep = 301; %number of points in time domain
T1source = 3; %source build up time in s
T1target = 100; %intrinsic relaxation time of the target in s
epsilon0 = 200; %source enhancement
slope = 5e10; %slope of the tanh function
theta = 0.9; %percentage of quenched signal in the source
dep = 0.5; %percentage of depolarization in the source
concsource = 100; %1H concentration in the source in molar
conctarget = 70; %1H concentration in the target in molar
MAS = 12.5; %MAS rate in kHz
D0 = 4.25e-3; %fictive diffusion coefficient of PS in a static sample
Din = D0*(conctarget/70)^(1/3)/(1+0.6*MAS); %The target diffusion coeff is scaled with the proton
concentration and MAS
Dout = D0*(concsource/70)^(1/3)/(1+0.6*MAS); %The source diffusion coeff is scaled with the proton
concentration and MAS
Cp = 7.98e-2; %Molar heat capacity of 1H spins at 9.4 T (not used)
k=1;

badass_function(m,length_target,rstep,tmax,tstep,T1source,T1target,epsilon0,Din,Dout,length_source,sl
ope,theta,dep,concsource,conctarget,Cp);

function
[p,pref,epsilon,epsilon2,epsilon3,SignalPol,SignalRef,SignalPol2,SignalRef2,SignalPol3,SignalRef3,NormSi
gnalPol,NormSignalRef,NormSignalPol2,NormSignalRef2,NormSignalPol3,NormSignalRef3]=badass_funct
ion(m,length_target,rstep,tmax,tstep,T1out,T1in,epsilon0,Din,Dout,length_source,slope,theta,dep,concj
uice,concuX,Cp)

 r = linspace(0,length_target+length_source,rstep);
 t = linspace(0,tmax,tstep);
 ipoint1 = floor(length_source*rstep/(length_target+length_source)); %index of the r matrix where the
target stops and the source begins

% Extract the first solution of the pdepe equation, as p and pref.
 sol = pdepe(m,@pdex1pde,@pdex1ic,@pdex1bc,r,t); %solution of the diffusion equation with
microwaves
  p = sol(:,:,1); %p is the polarization with microwaves
```

```
sol2 = pdepe(m,@pdex1pdenoDNP,@pdex1icnoDNP,@pdex1bcnoDNP,r,t);%solution of the diffusion
equation without microwaves
pref = sol2(:,:,1); %pref is the polarization without microwaves


% Process the polarization and calculate the enhancement
[p,pref,epsilon,epsilon2,epsilon3,SignalPol,SignalRef,SignalPol2,SignalRef2,SignalPol3,SignalRef3,NormSi
gnalPol,NormSignalRef,NormSignalPol2,NormSignalRef2,NormSignalPol3,NormSignalRef3]=CalcEpsilon(p
,pref,r,t);

% Function that process the polarization and calculate the enhancement
function
[p,pref,epsilon,Normepsilon,epsilon2,epsilon3,SignalPol,SignalRef,SignalPol2,SignalRef2,SignalPol3,Signal
Ref3,NormSignalPol,NormSignalRef,NormSignalPol2,NormSignalRef2,NormSignalPol3,NormSignalRef3] =
CalcEpsilon(p,pref,r,t)

    %Initialization of matrixes

    p_cut = zeros(length(t),length(r));
    pref_cut = zeros(length(t),length(r));
    Presign = zeros(length(t),length(r));
    Presignref = zeros(length(t),length(r));
    Presign2 = zeros(length(t),length(r));
    Presignref2 = zeros(length(t),length(r));
    Presign3 = zeros(length(t),length(r));
    Presignref3 = zeros(length(t),length(r));
    SignalPol = zeros(1,length(t));
    SignalRef = zeros(1,length(t));
    SignalPol2 = zeros(1,length(t));
    SignalRef2 = zeros(1,length(t));
    SignalPol3 = zeros(1,length(t));
    SignalRef3 = zeros(1,length(t));
    NormSignalPol = zeros(1,length(t));
    NormSignalRef = zeros(1,length(t));
    NormSignalPol2 = zeros(1,length(t));
    NormSignalRef2 = zeros(1,length(t));
    NormSignalPol3 = zeros(1,length(t));
    NormSignalRef3 = zeros(1,length(t));
    epsilon = zeros(1,length(t));
    epsilon2 = zeros(1,length(t));
    epsilon3 = zeros(1,length(t));
    Normepsilon = zeros(1,length(t));

    %Visible polarization
    for l=1:length(r)
        p_cut(:,l) = p(:,l)*theta0(r(l)); %Visible polarization ON
        pref_cut(:,l) = pref(:,l)*theta0(r(l));  %Visible polarization OFF
    end
```

```matlab
%Plot the polarizations

clf(figure(1));
figure(1);
plot(r,p,'LineWidth',1.5);
set(gca,'FontSize',22,'LineWidth',1.5);
xlabel('Position / \mum')
ylabel('Polarization \muwaves on')
x2=length_target;
y1=get(gca,'ylim');
hold on
grid on
plot([x2 x2],y1,'k','LineWidth',1.5);
hold off

clf(figure(2));
figure(2);
plot(r,pref,'LineWidth',1.5);
set(gca,'FontSize',22,'LineWidth',1.5);
xlabel('Position / \mum')
ylabel('Polarization \muwaves off')
x2=length_target;
y1=get(gca,'ylim');
hold on
grid on
plot([x2 x2],y1,'k','LineWidth',1.5);
hold off


% Calcul of Presignal
    for j=1:length(t)
        for k=1:length(r) %Here we integrate the entire system
            if m == 0
                Presign(j,k) = fc(r(k))*p_cut(j,k); %1D
                Presignref(j,k) = fc(r(k))*pref_cut(j,k);
            else
                if m == 1
                Presign(j,k) = fc(r(k))*p_cut(j,k)*(r(k)); %2D
                Presignref(j,k) = fc(r(k))*pref_cut(j,k)*(r(k));
                else
                    if m == 2
                Presign(j,k) = fc(r(k))*p_cut(j,k)*(r(k))^2; %3D
                Presignref(j,k) = fc(r(k))*pref_cut(j,k)*(r(k))^2;
                    end
                end
            end
        end
    end
```

```matlab
        end

    for j=1:length(t)
        for k=1:length(r)-ipoint1 %Here we only integrate the target
            if m == 0
                Presign2(j,k) = fc(r(k))*p_cut(j,k); %1D
                Presignref2(j,k) = fc(r(k))*pref_cut(j,k);
            else
                if m == 1
                Presign2(j,k) = fc(r(k))*p_cut(j,k)*(r(k)); %2D
                Presignref2(j,k) = fc(r(k))*pref_cut(j,k)*(r(k));
                else
                    if m == 2
                Presign2(j,k) = fc(r(k))*p_cut(j,k)*(r(k))^2; %3D
                Presignref2(j,k) = fc(r(k))*pref_cut(j,k)*(r(k))^2;
                    end
                end
            end
        end
    end
    for j=1:length(t)
        for k=length(r)-ipoint1:length(r) %Here we only integrate the source
            if m == 0
                Presign3(j,k) = fc(r(k))*p_cut(j,k); %1D
                Presignref3(j,k) = fc(r(k))*pref_cut(j,k);
            else
                if m == 1
                Presign3(j,k) = fc(r(k))*p_cut(j,k)*(r(k)); %2D
                Presignref3(j,k) = fc(r(k))*pref_cut(j,k)*(r(k));
                else
                    if m == 2
                Presign3(j,k) = fc(r(k))*p_cut(j,k)*(r(k))^2; %3D
                Presignref3(j,k) = fc(r(k))*pref_cut(j,k)*(r(k))^2;
                    end
                end
            end
        end
    end

% Calcul of the Signals by integrating the presignals
    for w=1:length(t)
    SignalPol(w) = trapz(Presign(w,:));
    SignalRef(w) = trapz(Presignref(w,:));
    SignalPol2(w) = trapz(Presign2(w,:));
    SignalRef2(w) = trapz(Presignref2(w,:));
    SignalPol3(w) = trapz(Presign3(w,:));
    SignalRef3(w) = trapz(Presignref3(w,:));
    end
```

124

```matlab
% The normalized values of Signal Pol and Ref
    for c=1:length(t)
    NormSignalPol(c) = SignalPol(c)./SignalPol(end);
    NormSignalRef(c) = SignalRef(c)./SignalRef(end);
    NormSignalPol2(c) = SignalPol2(c)./SignalPol2(end);
    NormSignalRef2(c) = SignalRef2(c)./SignalRef2(end);
    NormSignalPol3(c) = SignalPol3(c)./SignalPol3(end);
    NormSignalRef3(c) = SignalRef3(c)./SignalRef3(end);
    end

% The ratio of Pol and Ref gives the enhancement

    for v=1:length(t)
    epsilon(v) = SignalPol(v)./SignalRef(v);
    epsilon2(v) = SignalPol2(v)./SignalRef2(v);
    epsilon3(v) = SignalPol3(v)./SignalRef3(v);
    end

assignin('base', 'epsilon',epsilon);
assignin('base', 'epsilon2',epsilon2);
assignin('base', 'epsilon3',epsilon3);
assignin('base', 't',t);
assignin('base', 'NormSignalPol',NormSignalPol);
assignin('base', 'NormSignalRef',NormSignalRef);
assignin('base', 'NormSignalPol2',NormSignalPol2);
assignin('base', 'NormSignalRef2',NormSignalRef2);
assignin('base', 'NormSignalPol3',NormSignalPol3);
assignin('base', 'NormSignalRef3',NormSignalRef3);
assignin('base', 'SignalPol',SignalPol);
assignin('base', 'SignalRef',SignalRef);
assignin('base', 'SignalPol2',SignalPol2);
assignin('base', 'SignalRef2',SignalRef2);
assignin('base', 'SignalPol3',SignalPol3);
assignin('base', 'SignalRef3',SignalRef3);
assignin('base', 'r',r);
assignin('base', 'p',p);
assignin('base', 'pref',pref);
assignin('base', 'p_cut',p_cut);
assignin('base', 'pref_cut',pref_cut);


    %Plot

    clf(figure(3));
    figure(3);
    plot(t,epsilon2,t,epsilon3,'LineWidth',1.5);
    set(gca,'FontSize',22,'LineWidth',1.5);
```

```matlab
    xlabel('Time / s')
    ylabel('Enhancement')
    grid on
    legend('\epsilon_t','\epsilon_s','Location','northeast');

    clf(figure(4));
    figure(4);
    plot(t,NormSignalPol2,t,NormSignalRef2,'LineWidth',1.5);
    hold on
    plot(t,NormSignalPol3,t,NormSignalRef3,'LineWidth',1.5);
    set(gca,'FontSize',22,'LineWidth',1.5);
    xlabel('Time / s')
    ylabel('Signal / a.u.')
    grid on
    legend('S_{t,ON}','S_{t,OFF}','S_{s,ON}','S_{s,OFF}','Location','southeast');

end

%Plot all functions

        T1 = zeros(1,length(r));
  epsilonzero = zeros(1,length(r));
      theta3 = zeros(1,length(r));
          D = zeros(1,length(r));
depolarization = zeros(1,length(r));
 concentration = zeros(1,length(r));

for b = 1:length(r)
  T1(b) = fT1(r(b));
  epsilonzero(b) = fe0(r(b));
  theta3(b) = theta0(r(b));
  D(b) = fD(r(b));
  depolarization(b) = depo(r(b));
  concentration(b) = fc(r(b));
end

clf(figure(5));
figure(5);plot(r,D,'LineWidth',1.5);set(gca,'FontSize',22);
xlabel('Position / \mum')
ylabel('D / \mum^2s^{-1}')
  x2=length_target;
  y1=get(gca,'ylim');
  hold on
  plot([x2 x2],y1,'k','LineWidth',1.5)
  hold off

clf(figure(6));
figure(6);plot(r,T1,'LineWidth',1.5);set(gca,'FontSize',22);
```

```matlab
xlabel('Position / \mum')
ylabel('T_{1} / s')
  x2=length_target;
  y1=get(gca,'ylim');
  hold on
  plot([x2 x2],y1,'k','LineWidth',1.5)
  hold off

clf(figure(7));
figure(7);plot(r,epsilonzero,'LineWidth',1.5);set(gca,'FontSize',22);
xlabel('Position / \mum')
ylabel('P_{0,on} / a.u.')
  x2=length_target;
  y1=get(gca,'ylim');
  hold on
  plot([x2 x2],y1,'k','LineWidth',1.5)
  hold off

clf(figure(8));
figure(8);plot(r,theta3,'LineWidth',1.5);set(gca,'FontSize',22);
xlabel('Position / \mum')
ylabel('\theta / a. u.')
  x2=length_target;
  y1=get(gca,'ylim');
  hold on
  plot([x2 x2],y1,'k','LineWidth',1.5)
  hold off

clf(figure(9));
figure(9);plot(r,depolarization,'LineWidth',1.5);set(gca,'FontSize',22);
xlabel('Position / \mum')
ylabel('P_{0,off} / a.u.')
  x2=length_target;
  y1=get(gca,'ylim');
  hold on
  plot([x2 x2],y1,'k','LineWidth',1.5)
  hold off

clf(figure(10));
figure(10);plot(r,concentration,'LineWidth',1.5);set(gca,'FontSize',20);
xlabel('Position / \mum')
ylabel('^1H Concentration / M')
  x2=length_target;
  y1=get(gca,'ylim');
  hold on
  plot([x2 x2],y1,'k','LineWidth',1.5)
  hold off
```

```matlab
% --------------------------------------------------------------------
% Function definitions
% --------------------------------------------------------------------

% Source term WITH DNP.
function [c,f,s] = pdex1pde(x,~,u,DuDx)
    c = Cp*fc(x);
    f = fD(x)*Cp*fc(x)*DuDx;
    s = -(u-fe0(x))*(1/fT1(x))*Cp*fc(x);
end

% Source term WITHOUT DNP.
function [c,f,s] = pdex1pdenoDNP(x,~,u,DuDx)
    c = Cp*fc(x);
    f = fD(x)*Cp*fc(x)*DuDx;
    s = -(u-depo(x))*(1/fT1(x))*Cp*fc(x);
end

% Initial polarization is 0 all over the crystal WITH DNP
function u0 = pdex1ic(~)
    u0 = 0;
end

% Initial polarization is 0 all over the crystal WITHOUT DNP
function u0 = pdex1icnoDNP(~)
    u0 = 0;
end

% Boundary conditions WITH DNP
function [pl,ql,pr,qr] = pdex1bc(~,~,~,~,~)
    pl = 0;
    ql = 1;
    pr = 0;
    qr = 1;
end

% Boundary condition WITHOUT DNP
    function [pl,ql,pr,qr] = pdex1bcnoDNP(~,~,~,~,~)
    pl = 0;
    ql = 1;
    pr = 0;
    qr = 1;
    end

% T1 function that will determine the relaxation term
function [T1] = fT1(y)

    T1 = (T1in+T1out)/2+(T1in-T1out)/2*(tanh(slope*(length_target-y)));
```

```matlab
end

% Build-up epsilon spatial function MW ON
function [epsilonzero] = fe0(y)

    epsilonzero = (epsilon0*dep+1)/2+(epsilon0*dep-1)/2*(tanh(-slope*(length_target-y)));
end

% Contribution factor spatial function
function [theta3] = theta0(y)

    theta3 = (1+theta)/2+(1-theta)/2*tanh(slope*(length_target-y));

end

% Spin diffusion spatial function
function [D] = fD(y)

    D = (Din+Dout)/2+(Din-Dout)/2*(tanh(slope*(length_target-y)));

end

% Build-up spatial function MW OFF (depolarization)
function [depol] = depo(y)

    depol = (1+dep)/2+(1-dep)/2*tanh(slope*(length_target-y));

end

% Concentration spatial function
function [c] = fc(y)

    c = (concuX+concjuice)/2+(concuX-concjuice)/2*tanh(slope*(length_target-y));

end

end
```

Remerciements

Avant toute chose, je voudrais remercier tous les membres de mon jury de thèse, **Marek Pruski** et **Bradley Chmelka** (experts externes), **Jean-Philippe Ansermet** (expert interne), ainsi qu'à **Andreas Osterwalder** (président du jury) pour avoir accepté de lire et juger cette thèse. Merci également à Marek et Brad pour s'être déplacés des USA jusqu'à Lausanne. Et enfin merci à toutes les personnes présentes lors de l'examen oral pour les intéressantes discussions qui s'y sont établies.

Un immense merci à mon directeur de thèse **Lyndon Emsley** pour tout ce qu'il a fait pour moi. Il m'a d'abord accepté en thèse alors que les seules informations qu'il possédait à l'époque sur moi se trouvaient dans une vidéo intitulée *"Allez viens à l'ENS Lyon"*. S'il ne me jugeait pas sur cette vidéo, je pouvais être confiant pour l'avenir. Il faudrait un chapitre entier pour décrire toutes les fois où je me suis dit que j'avais de chance de faire une thèse avec lui. Durant ces 4 ans, il m'a soutenu, il était toujours disponible pour répondre à mes questions scientifiques (avec une déconcertante facilité), et a toujours cherché à pousser ma connaissance en RMN le plus loin possible. Il sait me dire quand ça ne va pas, mais il sait aussi me dire quand il est content de mon travail. Il a réussi à me faire **lire en entier** des articles écrits en 1960, imaginez-vous.

Merci à toutes les personnes avec qui j'ai pu travailler durant ces 4 années à l'EPFL. Tout d'abord merci à **Pascal Mieville**, **Anto Barisic**, **Vlado Janovic**, et **Émilie Baudat** pour avoir entretenu avec soin tous les spectromètres que j'ai pu utiliser durant cette these. Merci à **Donald Zbinden** pour avoir résolu mes nombreux soucis de connexion, ainsi qu'à **Annelise Carrupt**, **Gladys Pache**, et **Benjamin Kronenberg** du magasin BCH pour leur convivialité et leur verrerie inutilisée mais parfaite pour faire des pots de fleur.

Thanks to **Aaron Rossini** for initiating me to the art of packing and spinning a rotor in the proper way. He must have been hard for him to be patient enough to teach me all this, but I'm glad he did, even if it was for *"shits and gigs"*.

Merci à toutes les personnes qui étaient présentes au début de ma these, notamment la mafia romande. Merci à **Jonas Milani** pour m'avoir presque motivé à faire du sport en extérieur, **Basile Vuichoud** pour m'avoir accompagné dans mes virées solitaires à la salle de sport, **Sami Jannin** pour les précieuses discussions scientifiques que j'ai pu avoir avec lui, et enfin **Aurélien Bornet** pour tous les super moments que j'ai pu passer avec lui au labo comme à l'extérieur. Et plus globalement, merci à tous les 4 pour avoir égayé ma première année de thèse à l'EPFL (pour avoir bu des bières avec moi quoi).

Comme disait d'ailleurs Aurélien : « La science, ça se passe au coin café ».

Je ne bois pas de café.

Mais l'idée est belle. Je voudrais donc remercier toutes les personnes qui m'ont invité à prendre un café et à qui j'ai dit « non ». Parmi ces personnes, il y a évidemment toustes mes collègues du laboratoire LRM. Merci à **Dominik Kubicki** pour avoir été la première personne à m'éveiller au veganisme et à l'isolation sociale. C'est tellement bien l'isolation sociale. Thanks to **Brennan Walder**, for always taking the time to respond to my frequent and annoying NMR questions as clearly as he could. Thanks to **Albert Hofstetter** for helping me with my matlab program, I would have loose so much time without him. Thanks to **Federico Paruzzo** for the webpage and for being my drinking mate during the second year of

131

Curriculum Vitæ

First Name	Arthur
Middle Name	César
Last Name	Pinon
Date of birth	23.10.1991
Address	Route Cantonale 35, 1025 Saint-Sulpice (CH)
E-mail	arthur.pinon@epfl.ch
	arthurcesarpinon@gmail.com
Cellphone	+41 78 681 08 66

Education

2014 - 2018 **PhD thesis assistant**
École Polytechnique Fédérale de Lausanne, Lausanne, Switzerland / GlaxoSmithKline, Stevenage, United Kingdom.
Spin Diffusion in Dynamic Nuclear Polarization Nuclear Magnetic Resonance.
Directed by Lyndon Emsley (EPFL) & Tran Pham (GSK)

2012 - 2014 **Master of Science in Chemistry**
École Normale Supérieur de Lyon, Lyon, France.
Master in fundamental chemistry.
Earned with Honors.
Label "Réseau Français de Chimie Théorique".

2011 - 2012 **Bachelor of Science in Chemistry**
École Normale Supérieur de Lyon, Lyon, France.
Third year of bachelor in fundamental chemistry

2009 - 2011 **Classe préparatoire scientifique PCSI/PC**
Lycée Déodat de Séverac, Toulouse, France.
Intensive preparation in science for national competitive entry to the French "Grandes Écoles".
Majors: Maths, Physics and Chemistry

July 2009 **Scientific Baccalauréat**
Lycée Ozenne, Toulouse, France
Equivalent of High School Diploma.
Earned with Honors.
Majors: Maths, Physics and Chemistry.

Internships

January-July **Research Internship**
2014 *Centre de RMN à Très Hauts Champs, Villeurbanne, France*
Supervised by Lyndon Emsley.
DNP Enhanced NMR Crystallogrphy.

May-July **Research Internship**
2013 *University of Calgary, Calgary, AB, Canada*
Supervised by Simon Trudel.
Synthesis and Characterization of Cobalt-based Heusler Compound Nanoparticles.

June-July **Research Internship**
2012 *École Normale Supérieur de Lyon, Lyon, France.*
Supervised by Olivier Maury.
Synthesis and Study of Water-solvable Cyanine for Biological Imaging.

Teaching Experience

2014 - 2018 **EPFL Teaching assistant**
École Polytechnique Fédérale de Lausanne, Lausanne, Switzerland
Intensive module of doctoral course "Advanced NMR"
Undergraduate chemistry laboratory courses
Bachelor and Master NMR & MRI courses
Private lessons of chemistry and physics
Guidance of a bachelor thesis
Spectroscopy courses

Languages

French Native
English Fluent
Spanish Medium Intermediate

Computer skills

Operating Windows, Macintosh,
systems Linux

Engineering Illustrator, Chemdraw Mercury,
software COMSOL Multiphysics

Editors Latex, Office

Programming C, Bash, Matlab

Sports	Trampoline, Gymnastics, Snowboard
Associative	Member of the French *Bureau des Élèves* of the ENS de Lyon (2011-2012)
Arts	Music producer
International	Lived in Brazil for one year (2007-2008), validated the second High School year by correspondence

Awards and Grants

2017 - Student travel stipend for the 58th Experimental NMR Conference (ENC)

Publications

1. Huynh, L. T.; Bonvicini, S. N.; **Pinon, A. C.**; Trudel, S.
   "Nanocrystalline alloys: synthesis and characterization of non-stoichiometric Co_2FeAl nanocrystals"
   Canadian Journal of Chemistry **2015**, 94, 367-372.
   DOI: 10.1139/cjc-2015-0352

2. **Pinon, A. C.**; Rossini, A. J.; Widdifield, C. M.; Gajan, D.; Emsley, L.
   "Polymorphs of Theophylline Characterized by DNP Enhanced Solid-State NMR"
   Mol. Pharm. **2015**, 12, 4146-4153.
   DOI: 10.1021/acs.molpharmaceut.5b00610

3. Bornet, A.; **Pinon, A. C.**; Jhajharia, A.; Baudin, M.; Ji, X.; Emsley, L.; Bodenhausen, G.; Ardenkjaer-Larsen, J. H.; Jannin, S.
   "Microwave-gated Dynamic Nuclear Polarization"
   Phys. Chem. Chem. Phys. **2016**, 18, 30530-30535.
   DOI: 10.1039/C6CP05587G

4. **Pinon, A. C.**; Schlagnitweit, J.; Berruyer, P.; Rossini, A. J.; Lelli, M.; Socie, E.; Tang, M.; Lesage, A.; Schantz, S.; Tran, P. and Emsley, L.
   "Measuring Nano- to Micro Structures from Relayed Dynamic Nuclear Polarization NMR."
   J. Phys. Chem. C **2017**, 121, 15993-16005.
   DOI: 10.1021/acs.jpcc.7b04438

5. Chaudhari, S. R.; Wisser, D.; **Pinon, A. C.**; Berruyer, P.; Gajan, D.; Tordo, P.; Ouari, O.; Reiter, C.; Engelke, F.; Coperet, C.; Lelli, M.; Lesage, A.; Emsley, L.
   "Dynamic Nuclear Polarization Efficiency Increased by Very Fast Magic Angle Spinning"
   J. Am. Chem. Soc. **2017**, 139, 10609-10612.
   DOI: 10.1021/acs.jpclett.7b01512

6. Dumez, J.-N.; Vuichoud, B.; Mammoli, D.; Bornet, A.; **Pinon, A. C.**; Stevanato, G.; Meier, B.; Bodenhausen, G.; Jannin, S.; Levitt, M. H.
   "Dynamic Nuclear Polarization of Long- Lived Nuclear Spin States in Methyl Groups"
   J. Phys. Chem. Let. **2017**, 8, 3549-3555.
   DOI: 10.1021/acs.jpclett.7b01512

7   Zhao, L.; **Pinon, A. C.**; Emsley, L; and Rossini, A.J.
"DNP-Enhanced Solid-State NMR Spectroscopy of Active Pharmaceutical Ingredients"
Magn. Reson. Chem. **2017**, 1-27.
DOI: 10.1002/mrc.4688

8   Björgvinsdóttir, S.; Walder, B. J.; **Pinon, A. C.**; Yarava, J. R.; and Emsley, L.
"DNP enhanced NMR with flip-back recovery"
J. Mag. Res. **2018,** 288:69-75
DOI: 10.1016/j.jmr.2018.01.017

9   Viger-Gravel, J.; Schantz, A.; **Pinon, A. C.**; Rossini, A. J.; Schantz, S.; and Emsley, L.
"Structure of Lipid Nanoparticles Containing siRNA or mRNA by Dynamic Nuclear Polarization Enhanced NMR Spectroscopy"
J. Phys. Chem. B **2018,** 122(7):2073-2081
DOI: 10.1021/acs.jpcb.7b10795

10 Björgvinsdóttir, S.; Walder, B. J.; **Pinon, A. C.**; and Emsley, L.
"Bulk Nuclear Hyperpolarization of inorganic solids"
J. Am. Chem. Soc. **2018,** 140, 25, 7946-7951